VOL.107 NO.GT1. JAN. 1981

JOURNAL OF THE GEOTECHNICAL ENGINEERING DIVISION

PROCEEDINGS OF
THE AMERICAN SOCIETY
OF CIVIL ENGINEERS

VOL. 107 NO. GT1. JAN. 1981

JOURNAL OF THE GEOTECHNICAL ENGINEERING DIVISION

PROCEEDINGS OF THE AMERICAN SOCIETY OF CIVIL ENGINEERS

ISSN 0093-5405

AMERICAN SOCIETY OF CIVIL ENGINEERS

CONTENTS

Pile Load Tests: Cyclic Loads and Varying Load Rates
by Leland M. Kraft, Jr., William R. Cox, and Edward A. Verner 1

Longitudinal Vibrations of Embankment Dams
by George Gazetas 21

Cyclic Axial Response of Single Pile
by Harry G. Poulos 41

Embedded Anchor Response to Uplift Loading
by Andreas Andreadis, Roger C. Harvey, and Eldon Burley 59

Construction of Large Canal on Collapsing Soils
by Paul C. Knodel 79

Computer Simulation of Creep of Clay
by Roland Pusch and Paul Feltham 95

→

This Journal is published monthly by the American Society of Civil Engineers. Publications office is at 345 East 47th Street, New York, N.Y. 10017. Address all ASCE correspondence to the Editorial and General Offices at 345 East 47th Street, New York, N.Y. 10017. Allow six weeks for change of address to become effective. Subscription price to members is $16.00. Nonmember subscriptions available; prices obtainable on request. Second-class postage paid at New York, N.Y. and at additional mailing offices. GT.

The Society is not responsible for any statement made or opinion expressed in its publications.

TECHNICAL NOTES

Proc. Paper 15956

Stresses in Soil around Vertical Compressible Piles
by K. S. Sankaran, N. R. Krishnaswamy, and B. K. Sharas Chandra 107

DISCUSSION

Proc. Paper 15952

Extreme-Value Problems of Limiting Equilibrium,* by Michael Garber and Rafael Baker (Oct., 1979).
by Reginald A. Barron 115
by Ryszard J. Izbicki 116
by A. Luceño and E. Castillo 118
closure 121

INFORMATION RETRIEVAL

The key words, abstract, and reference "cards" for each article in this Journal represent part of the ASCE participation in the EJC information retrieval plan. The retrieval data are placed herein so that each can be cut out, placed on a 3 × 5 card and given an accession number for the user's file. The accession number is then entered on key word cards so that the user can subsequently match key words to choose the articles he wishes. Details of this program were given in an August, 1962 article in CIVIL ENGINEERING, reprints of which are available on request to ASCE headquarters.

*Discussion period closed for this paper. Any other discussion received during this discussion period will be published in subsequent Journals.

16000 PILE LOAD TESTS: CYCLIC LOADS AND LOAD RATES

KEY WORDS: Capacity; Clays; Compression; **Cyclic loads; Loading rate; Pile load tests (cyclic loading); Soils; Steel piles;** Stratigraphy; Tension; **Unconsolidated soils**

ABSTRACT: Two series of axial load tests were performed on four 14-in. (356-mm) diam, open-end, steel pipe piles at an interval of about 320 days. Pile lengths of 40 ft or 50 ft (12.2 or 15.2 m) were installed below conductors driven to depths ranging from 115 ft to 320 ft (35 m to 98 m) into a strong underconsolidated clay. Each pile was subjected to as many as 26 tests. Data presented includes: (1) Compression and tension tests; (2) tests performed at different times after driving and after previous tests; and (3) incremental loading and constant rate of loading. Pile capacity increased 40% to 75% when the loading rate increased by three orders of magnitude. The one-way cyclic loading applied in this study did not effect the ultimate capacity, but large displacement began to accumulate when the maximum cyclic load reached 80% of the static capacity.

REFERENCE: Kraft, Leland M., Cox, William R., and Verner, Edward A., "Pile Load Tests: Cyclic Loads and Varying Load Rates," *Journal of the Geotechnical Engineering Division,* ASCE, Vol. 107, No. GT1, **Proc. Paper 16000**, January, 1981, pp. 1-19

15980 LONGITUDINAL VIBRATIONS OF EMBANKMENT DAMS

KEY WORDS: **Earth dams; Earthquakes; Embankments;** Soil dynamics

ABSTRACT: This paper presents an analytical method to study free and forced longitudinal vibrations of embankment dams. Both shear and dilatational deformations are taken into account, and the dam is modeled as a linear homogeneous prism with a wedge-shape cross section, bounded by two vertical (abutment) and one horizontal (riverbed) planes. Numerical results demonstrate the effect of the length and height of the dam on its natural frequencies and its modal displacement and strain shapes. It is shown that shear deformations are more important in relatively long dams, whereas the opposite is true with dams built in narrow canyons. The method is evaluted through two case histories involving an earthfill and a rockfill dam. Close agreement exists between predicted and observed natural frequencies, but the distribution of peak accelerations within the dam is badly predicted.

REFERENCE: Gazetas, George, "Longitudinal Vibrations of Embankment Dams," *Journal of the Geotechnical Engineering Division,* ASCE, Vol. 107, No. GT1, **Proc. Paper 15980**, January, 1981, pp. 21-40

15979 CYCLIC AXIAL RESPONSE OF SINGLE FILE

KEY WORDS: **Bearing capacity;** Consolidation; **Cyclic loads;** Foundations; **Offshore structures; Pile settlement;** Piles (foundations); **Shear strain;** Skin friction; Soil mechanics

ABSTRACT: A number of solutions have been obtained for a typical offshore pile, to determine the influence of a number of the input parameters on the computered cyclic response. More significant parameters include the critical shear strain at which significant degradation of skin friction occurs, the rate of loading on the pile, and the distributions of static skin friction and soil modulus along the pile. The analysis predicts a gradual decrease in cyclic stiffness of the pile with increasing numbers of cycles and increasing cyclic load level, but a very sudden decrease in ultimate load capacity once the (half-peak-to-peak) cyclic load level exceeds 50% to 60% of the ultimate static load capacity. These theoretical findings are broadly confirmed by the results of small-scale laboratory model tests.

REFERENCE: Poulos, Harry G., "Cyclic Axial Response of Single File," *Journal of the Geotechnical Engineering Division,* ASCE, Vol. 107, No. GT1, **Proc. Paper 15979**, January, 1981, pp. 41-58

15985 ANCHOR RESPONSE TO UPLIFT LOADING

KEY WORDS: Anchors; **Foundations; Ocean engineering; Soil mechanics**

ABSTRACT: A number of factors which influence soil-anchor interaction are evaluated, and in addition, the extent of soil disturbance and the influence of pore water pressures during testing are assessed. Response under repeated and sustained-repeated loading is shown to be represented by a family of hyperbolic curves, and a failure criterion is determined by the critical strain condition below which a satisfactory response can still be subsequent to repeated loading. A strain dependent mechanism is used for defining behaviour under varying loading conditions which permits an assessment of anchor life when subjected to a package of projectd environmental conditions. Where possible the results are compared to those of other workers in the anchor field, and recommendations made which may lead to a better understanding of embedded systems.

REFERENCE: Andreadis, Andreas, Harvey, Roger C., and Burley, Eldon, "Embedded Anchor Response to uplift Loading," *Journal of the Geotechnical Engineering Division,* ASCE, Vol. 107, No. GT1, **Proc. Paper 15985**, January, 1981, pp. 59-78

15992 CONSTRUCTION OF CANAL ON COLLAPSING SOILS

KEY WORDS: **Canals; Collapsible soils;** Depth; Field density; Liquid limit; **Pneumatic tired rollers; Pondweeds;** Soil consolidation tests; **Subsidence**

ABSTRACT: Soil subsidence may occur because of withdrawal of fluids (usually deep subsidence), the drainage of peat lands, or by the application of water to moisure-deficient, low-density soils (usually near-surface subsidence). Only near-surface subsidence is analyzed in connection with the investigations for, and construction of, the San Luis Canal where parts of the alinement passed through areas of low-density, moisture-deficient soils. Ponding of the critical subsidence areas delineated by studies was an effective methods of collapsing and densifying the soils prior to construction of the canal. The canal invert and the embankment were densified with a heavy pneumatic roller during the construction phase. The San Luis Canal was constructed during 1963 to 1968 and has functioned with only minor problems to date (1979).

REFERENCE: Knodel, Paul C., "Construction of Large Canal on Collapsing Soils," *Journal of the Geotechnical Engineering Division,* ASCE, Vol, 107, No. GT1, **Proc. Paper 15992**, January, 1981, pp. 79-94

15998 COMPUTER SIMULATION OF CREEP OF CLAY

KEY WORDS: **Clays; Computerized simulation; Creep;** Creep rate; **Energy; Energy bands;** Illite; **Microstructure;** Soil mechanics; Soil physics; Stochastic models

ABSTRACT: The variable character of the particle contacts in natural illitic clay implies a spectrum of bond strengths. When a sufficiently high external shear stress is applied some weaker interlinking particle groups are transformed to "domains" which act as slip units. In creep induced by a constant deviatoric stress, the number and heights of thermally activable barriers to slip will vary in space and time. This is encompassed by a stochastic model, a simple version of which was used in a computer simulation. The dependence of the strain on time was found to be logarithmic, in good agreement with experiments.

REFERENCE: Pusch, Roland, and Feltham, Paul, "Computer Simulation of Creep of Clay," *Journal of the Geotechnical Engineering Division,* ASCE, Vol. 107, No. GT1, **Proc. Paper 15998**, January, 1981, pp. 95-104

JOURNAL OF THE GEOTECHNICAL ENGINEERING DIVISION

PILE LOAD TESTS: CYCLIC LOADS AND VARYING LOAD RATES

By Leland M. Kraft, Jr.,[1] William R. Cox,[2] and Edward A. Verner,[3]
Members, ASCE

INTRODUCTION

A cooperative research study was undertaken by Chevron Oil Field Research Company with 13 other participants to provide data on the axial-load capacity of deep foundation piling in strong clays that are underconsolidated. Two series of axial load tests were performed in 1975 on four 14-in. (356-mm)-diam, open-end, steel pipe piles with an interval of some 320 days between each series. The test site was located one mile south of Empire, La. (Fig. 1).

The scope of the initial testing program was limited to pile capacities under static load conditions. Additional information about pile performance could be obtained at a nominal increase in cost by including tests at different loading rates, so the project scope was increased during the project. The data from the two test series offer an opportunity to gain an improved understanding of the performance of piles subjected to axial loads. Data are available for: (1) Compression and tension tests; (2) tests performed at different times after driving and after previous tests; (3) incremental loading and constant rate of loading tests; (4) tests loaded to failure in periods ranging from a few seconds to hours; and (5) cyclic load tests with periods typical of ocean wave loading. Pile performance was studied in terms of: (1) Load-deformation (pile-soil stiffness) response at the top of the test pile; (2) cumulative pile deformation; (3) distribution of load transfer along the pile with load application; (4) redistribution of load

[1]Mgr., Special Projects Group, McClelland Engrs., Inc., 6100 Hillcroft, Houston, Tex. 77081.

[2]Vice Pres. and Mgr., Offshore Engineering, McClelland Engrs., Inc., 6100 Hillcroft, Houston, Tex. 77081.

[3]Vice Pres. and Mgr., Offshore Technology, TERA, Inc., Houston, Tex.

Note.—Discussion open until June 1, 1981. To extend the closing date one month, a written request must be filed with the Manager of Technical and Professional Publications, ASCE. Manuscript was submitted for review for possible publication on March 25, 1980. This paper is part of the Journal of the Geotechnical Engineering Division, Proceedings of the American Society of Civil Engineers, © ASCE, Vol. 107, No. GT1, January, 1981. ISSN 0093-6405/81/0001-0001/$01.00.

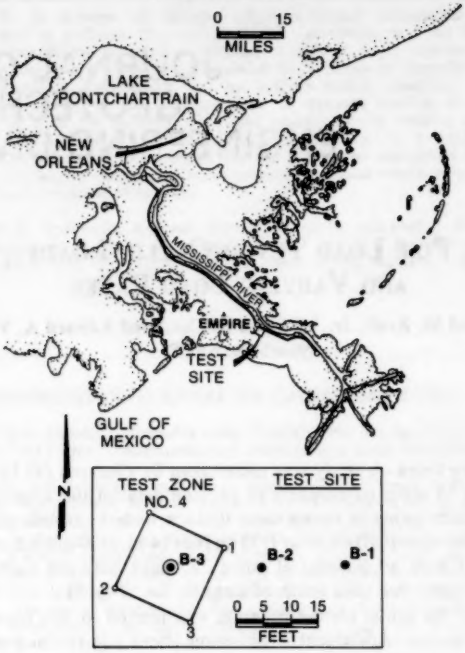

FIG. 1.—Test Site and Boring Plan (1 ft = 0.305 m; 1 mile = 1.6 km)

transfer along the pile with cyclic loading and unloading; and (5) ultimate pile resistance.

This paper describes the soil conditions, the piles, the test program, the reduced pile load test data, and an evaluation of these data.

Soils Investigation

Soil Borings.—The soils investigation included: (1) Three undisturbed sample borings at the site to determine soil stratigraphy and to obtain samples for laboratory tests; (2) spontaneous-potential, gamma-ray, and resistivity logs in a boring to provide additional definition of soil stratigraphy; (3) field and laboratory tests on recovered samples to determine pertinent physical properties of the soils; and (4) engineering analyses of the field and laboratory data for general planning of the test program and to develop pile capacity predictions.

The soils investigation also included in situ remote vane (6,7) tests. A comprehensive suite of classification tests and strength measurements from unconfined compression tests, unconsolidated-undrained tests, and miniature vane tests were performed. In addition, stress-strain curves and measured shear strengths were determined from six triaxial compression tests, eight static simple

shear tests, five cyclic simple shear tests, three direct shear tests, and 16 friction tests between clay and steel (eight of these tests were on remolded specimens).

Stratigraphy.—The borings drilled at the test site revealed a stratigraphic sequence containing two major clay strata in which the pile tests were performed. These strata are a firm, highly plastic, uniform clay extending from 76-ft to 178-ft (23-m to 54-m) penetration; and a stiff to very stiff, gray, highly plastic clay, containing seams of sand, silty sand, and sandy silt, from 188-ft to 372-ft (57-m to 113-m) penetration. The stratigraphy as revealed by Boring No. 3 and the interpreted shear strength profile are summarized in Fig. 2. Four 40-ft to 50-ft thick zones of clay between 115-ft and about 360-ft penetration were selected from boring data in which to perform the pile tests. These test zones

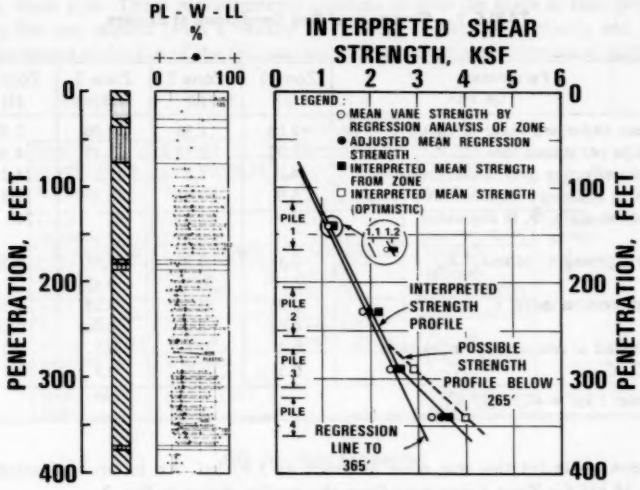

FIG. 2.—Soil Conditions at Empire Test Site (1 ft = 0.305 m; 1 ksf = 47.9 kN/m^2)

are denoted by "Pile 1," "Pile 2," "Pile 3," and "Pile 4" in Fig. 2. Table 1 summarizes the range in interpreted soil properties for each test zone.

Resistivity and gamma-ray logs, sample descriptions, and Atterberg limit data indicate little layering and property variation in Zone 1. The mean interpreted strength in Zone 1 is 1.20 ksf.

The material in Zone 2 is more variable, based on resistivity, gamma ray, and sample logs, than the soil in Zone 1. Many thin seams of sand and silt were revealed in the clay. The mean shear strength from the interpreted profile is 2.03 ksf Zone 2.

The material in Zone 3 shows similar variability to Zone 2 based on sample descriptions, resistivity, and gamma-ray logs. Sample recovery was poor, due primarily to its layered condition, and strength data are concentrated at the bottom portion of this zone. Test results from 205-ft, 302-ft, 305-ft, 310-ft, and 320-ft penetrations were larger than results at other penetrations. These

larger results indicate a mean strength of about 2.6 ksf. Judgment interpretation, relying on miniature vane data largely in a zone at 250-ft penetration and another zone from 340-ft to 345-ft penetration, suggests a mean strength of about 2.9 ksf. For this study, we used an interpreted mean strength of 2.6 ksf for Zone 3.

The resistivity and gamma-ray logs indicate sandy material from 346-ft to 352-ft penetration in Zone 4. Sample descriptions show that the clay in this zone is layered with sand and silt seams. The strength data exhibited considerable scatter in Zone 4 due to variable sample disturbance caused by layering and variations in physical properties of the material. A weighted mean strength based on the larger vane values in this zone was 3.61 ksf. A different judgment interpretation, based largely on data at 250 ft and from 340 ft to 345 ft, suggests

TABLE 1.—Summary of Soil Conditions at Empire

Parameters (1)	Zone 1 (2)	Zone 2 (3)	Zone 3 (4)	Zone 4 (5)
Mean undrained shear strength, s_{um}, in kips per square foot	1.08 1.32	1.83 2.23	2.08 3.12	2.86 4.30
Mean effective overburden pressure, $\bar{\sigma}_{vm}$, in kips per square foot	4.8 5.9	8.3 10.4	12.2 13.5	14.2 15.8
Friction angle, Φ, in degrees	25	22 27	22 27	26
Earth pressure "at rest," K_0	0.58	0.55 0.63	0.55 0.63	0.56
Compression index, C_c	0.46 0.62	0.23 0.62	0.28 0.76	0.32 0.58
Rebound to compression index ratio, C_r/C_c	0.2 0.3	0.2 0.3	0.2 0.3	0.2 0.3

Note: 1 ksf = 47.9 kN/m^2.

a mean value for this test zone as much as 3.95 ksf. An interpreted strength of 3.58 ksf for Zone 4 was used from the profile shown in Fig. 2.

Test Piles and Test Sequence

To isolate the tests to the selected strata of soil, 18-in. (457-mm) diam conductors were driven to the top of the test zones and then the soil plugs in the conductors were drilled out. The four 14-in. (356-mm)-diam, open-end piles were then driven into the test zones below the conductors.

The first series of compression and tension axial load tests were made on the four piles in the period January 20–28, 1975; these initial tests on each pile were performed 4 days to 10 days after driving. The first series of tests consisted generally of slow static (incremental loading) tests in compression and tension modes. A few "quick static" tests (constant loading rate) were performed selectively on two piles.

The first tests in the second series were made some 320 days after the last tests of the first series. The second series of tests were performed with continuous loading for each test. At the end of the static tests in the second series, cyclic

tests with about a 15-s period were run in compression mode on each of the four piles. At the end of cyclic testing, static tests at varying rates of loading were made. A series of very fast compression loadings were then made under separate funding provided by Shell Oil Company; these tests will be referred to as the "fast tests." The chronological sequence of the different tests are shown in Fig. 3. Test information, including the setup time, are tabulated in Table 2, which also summarizes the loading rates for each test type.

A schematic diagram of the test setup is presented in Fig. 4. The acquired data consisted of the axial strains at four points along the length of the test section, the pressure in the jacking system, the vertical movement of a weight attached by wire line to a weight at the top of the test section (diaphragm), and the vertical movements of two plates on either side of the top of the 14-in. diam pipe. These measurements combine to give the loads at four points along the test section (with a backup for the top of the test section), and the displacement at the top of the test section with a backup measurement at ground

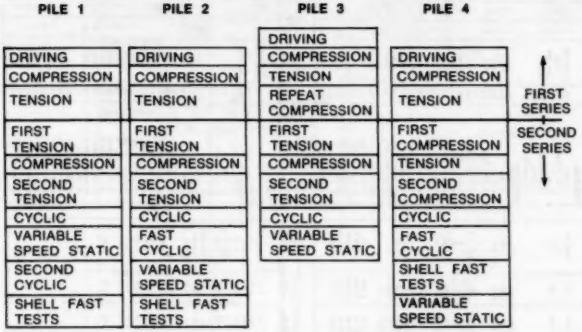

FIG. 3.—Test Sequence

level. The lead wires for the downhole bridges on Pile 2 were broken during cable recovery attempts, rendering all bridges for that pile inoperative.

The results were sampled with a data logger on a sequential basis during testing with an elapsed time between samples of about 1.5 s. The data were automatically recorded, and the time shift was accounted for in the data reduction process.

All displacement measurements were made with transducers of a linear variable differential transformer type that were individually calibrated. During the first series of static tests, the displacement at the top of the test section was measured with the backup system, because the primary wire-line system failed to function. These backup measurements were arrived at by measuring the displacement at the top of the 14-in. pile and adjusting this value by the calculated amount of shortening, or extension, for the long length of pipe between the pile top and the diaphragm at the top of the test section. For the longer piles this adjustment was of the same order as the top displacement, resulting in considerable amplification of any errors in the component measurements. Probable errors

TABLE 2.—Summary of Pile Test Information

PILE 1

Test	Yes/No	Comp/Tens	Disp. Top	Disp. b-1	Load Top	Load b-1	Load b-2	Load b-3	Load b-4	Date 1975 (M/D)	Duration m:sec	Setup m:sec[2]
First Series												
1 Static	Yes	Comp (max)	D	D[1][3]	D	D	D	D	D	1/23	1.59	7 days, 1 hr
2 Quick Static	No											
3 Static	Yes	Tens (max)	D	D[1][3]	D	D	D	D	D	1/23	1.36	3.15
4 Quick Static	No											
5 Static	No											
6 Quick Static	No											
Second Series												
7 Static	Yes	Tens	D	D	D	D	D	D	D	12/12	1.09	323 days
8 Static	Yes	Comp	D	D	D	D	D	D	D	12/12	0.43	2.39
9 Static	Yes	Tens	D	D	D	D	D	D	D	12/12	0.58	2.37
10 Quick Static	No											
11 Cyclic (10-30)	No											
12 Cyclic (20-60)	Yes	Comp		G	G	G			G	12/17	0.48	4 days, 23 hr
13 Cyclic (30-70)	Yes	Comp		G	G	G			G	12/17	0.21	0.08
14 Cyclic (40-80)	Yes	Comp		G	G	G			G	12/17	0.49	0.03
15 Cyclic (50-90)	Yes	Comp		G	G	G			G	12/17	0.50	0.06
16 Cyclic (40-100)	Yes	Comp		G	G	G			G	12/17	0.25	0.03[3]
17 Cyclic (70-110)	No											
18 Variable Cyclic	No											
19 Variable Static	Yes	Comp	D	D,G	D,G	D,G	D	D	D,G	12/17	0.57	0.11
20 Variable Static	Yes	Comp	D	D,G	D,G	D,G	D	D	D,G	12/17	0.11	0.01
21 Variable Static	Yes	Comp	D	D,G	D,G	D,G	D	D	D,G	12/17	0.04	0.01
22 Variable Static	Yes	Comp	D	D,G	D,G	D,G	D	D	D,G	12/17	0.03	-
23 Variable Static	Yes	Comp	T	D,G	D,G	D,G	D	D	D,G	12/17	0.02	-
24 Variable Static	No											
25 Shaft Fast Test	Yes	Comp	G	G	G	G				12/18	0.0033	15.44
26 Shaft Fast Test	Yes	Comp	G	G	G	G				12/18	0.0024	0.4820
27 Shaft Fast Test	Yes	Comp	G	G	G	G				12/18	0.0028	0.0312
28 Shaft Fast Test	Yes	Comp	G	G	G	G				12/18	0.0026	0.2118
29 Shaft Fast Test	Yes	Comp	G	G	G	G				12/18	0.0034	0.0352
30 Shaft Fast Test	No											

PILE 2

Test	Yes/No	Comp/Tens	Disp. Top	Disp. b-1	Load Top	Load b-1	Load b-2	Load b-3	Load b-4	Date 1975 (M/D)	Duration m:sec	Setup m:sec[2]
					Low Force (4)							
First Series												
1 Static	Yes	Comp (max)	D	D[1][3]	D					1/23	3.13	9 days, 3 hr
2 Quick Static	Yes	Comp	D	D[1][3]	D					1/25	0.12	0.08
3 Static	Yes	Tens (max)	D	D[1][3]	D					1/25	1.39	2.02
4 Quick Static	Yes	Tens	D	D	D					1/25	0.11	0.13
5 Static	No											
6 Quick Static	No											
Second Series												
7 Static	Yes	Tens	D	D	D					12/10	1.33	319 days
8 Static	Yes	Comp	D	D	D					12/10	0.46	3.40
9 Static	Yes	Tens	D	D	D					12/10	0.35	2.21
10 Quick Static	Yes	Tens	D	D	D					12/10	0.06	0.14
11 Cyclic (10-30)	No											
12 Cyclic (20-60)	Yes	Comp		G	G	G				12/21	0.5011	10 days, 11 hr
13 Cyclic (30-70)	Yes	Comp		G	G	G				12/21	0.7004	0.1042
14 Cyclic (40-80)	Yes	Comp		G	G	G				12/21	0.4923	0.0120
15 Cyclic (50-90)	Yes	Comp		G	G	G				12/21	0.4912	0.0134
16 Cyclic (40-100)	Yes	Comp		G	G	G				12/21	0.2652	0.0133
17 Cyclic (70-110)	No											
18 Variable Cyclic	Yes	Comp		D,G	D,G	D,G				12/21	0.52	0.12
19 Variable Static	Yes	Comp		D,G	D,G	D,G				12/21	0.5601	0.32
20 Variable Static	Yes	Comp		D,G	D,G	D,G				12/21	0.0401	0.0209
21 Variable Static	Yes	Comp		D,G	D,G	D,G				12/21	0.0207	0.0222
22 Variable Static	Yes	Comp		D,G	D,G	D,G				12/21	0.0107	0.0243
23 Variable Static	Yes	Comp		D,G	D,G	D,G				12/21	0.0126	0.0127
24 Variable Static	Yes	Comp		D,G	D,G	D,G				12/21	0.0229	0.0133
25 Shaft Fast Test	Yes	Comp		G	G	G				12/21	0.0220	0.2861
26 Shaft Fast Test	Yes	Comp		G	G	G				12/21	0.0220	0.0819
27 Shaft Fast Test	Yes	Comp		G	G	G				12/21	0.0052	0.0102
28 Shaft Fast Test	Yes	Comp		G	G	G				12/21	0.0052	0.0847
29 Shaft Fast Test	Yes	Comp		G	G	G				12/21	0.0053	0.0429
30 Shaft Fast Test	Yes	Comp		G	G	G				12/21	0.0054	0.0259

PILE 3

Test	Yes/No	Comp/Tens	Disp. Top	Disp. b-1	Load Top	Load b-1	Load b-2	Load b-3	Load b-4	Date 1975 (M/D)	Duration m:sec	Setup m:sec[2]
First Series												
1 Static	Yes	Comp (max)	D	D[1][3]	D	D	D	D	D	1/26	2.15	10 days, 9 hr
2 Quick Static	Yes	Comp	D	D[1][3]	D	D	D	D	D	1/26	0.12	0.21
3 Static	Yes	Tens (max)	D	D[1][3]	D	D	D	D	D	1/27	1.57	11.35
4 Quick Static	Yes	Tens	D	D	D	D	D	D	D	1/27	0.11	0.16
5 Static	Yes	Comp (max)	D	D[1][3]	D	D	D	D	D	1/28	1.24	27.30
6 Quick Static	Yes	Comp	D	D[1][3]	D	D	D	D	D	1/28	0.30	0.03
Second Series												
7 Static	Yes	Tens	D	D	D	D	D	D	D	12/7	0.53	312 days
8 Static	Yes	Comp	D	D	D	D	D	D	D	12/8	1.07	23.38
9 Static	Yes	Tens	D	D	D	D	D	D	D	12/8	1.32	3.35
10 Quick Static	Yes	Tens	D	D	D	D	D	D	D	12/8		
11 Cyclic (10-30)	Yes	Comp		G	G	G		G		12/16	0.48	7 days, 9 hr
12 Cyclic (20-60)	Yes	Comp		G	G	G		G		12/16	0.51	0.09
13 Cyclic (30-70)	Yes	Comp		G	G	G		G		12/16	0.57	0.03
14 Cyclic (40-80)	Yes	Comp		G	G	G		G		12/16	0.50	0.27
15 Cyclic (50-90)	Yes	Comp		G	G	G		G		12/16	0.50	0.07
16 Cyclic (40-100)	Yes	Comp		G	G	G		G		12/16	0.51	0.09
17 Cyclic (70-110)	Yes	Comp		G	G	G		G		12/16	0.03	0.09
18 Variable Cyclic	No											
19 Variable Static	Yes	Comp	D	D,G	D,G	D,G	D,G	D,G	D,G	12/16	0.23	0.06
20 Variable Static	No											
21 Variable Static	No											
22 Variable Static	No											
23 Variable Static	No											
24 Variable Static	No											
25 Shaft Fast Test	No											
26 Shaft Fast Test	No											
27 Shaft Fast Test	No											
28 Shaft Fast Test	No											
29 Shaft Fast Test	No											
30 Shaft Fast Test	No											

PILE 4

Test	Yes/No	Comp/Tens	Disp. Top	Disp. b-1	Load Top	Load b-1	Load b-2	Load b-3	Load b-4	Date 1975 (M/D)	Duration m:sec	Setup m:sec[2]
First Series												
1 Static	Yes	Comp (max)	D	D[1][3]	D	D[1][3]	D	D	D	1/28	3.24	4 days, 3 hr
2 Quick Static	No											
3 Static	Yes	Tens (max)	D	D[1][3]	D	D[1][3]	D	D	D	1/31	2.40	26.41
4 Quick Static	No											
5 Static	No											
6 Quick Static	No											
Second Series												
7 Static	Yes	Comp	D	D	D	D[1][3]	D	D	D	12/14	0.59	327 days
8 Static	Yes	Tens	D	D	D	D[1][3]	D	D	D	12/14	1.34	3.20
9 Static	Yes	Comp	D	D	D	D[1][3]	D	D	D	12/14	1.32	2.35
10 Quick Static	No											
11 Cyclic (10-30)	No											
12 Cyclic (20-60)	Yes	Comp			G	G		G	G	12/19	0.50	4 days, 20 hr
13 Cyclic (30-70)	Yes	Comp			G	G		G	G	12/19	0.50	1.05
14 Cyclic (40-80)	Yes	Comp			G	G		G	G	12/19	0.50	0.03
15 Cyclic (50-90)	Yes	Comp			G	G		G	G	12/19	0.50	0.07
16 Cyclic (40-100)	Yes	Comp			G	G		G	G	12/19	0.52	0.12
17 Cyclic (70-110)	Yes	Comp			G	G		G	G	12/19	0.09	0.06
18 Variable Cyclic	Yes	Comp			G	G		G	G	12/19	0.39	1.01
19 Variable Static	Yes	Comp	D	D,G	D,G	D,G[1][3]	D,G	D,G	D	12/20	0.17	1.40[3]
20 Variable Static	Yes	Comp	D	D,G	D,G	D,G[1][3]	D,G	D,G	D	12/20	0.15	0.07[3]
21 Variable Static	Yes	Comp	D	D,G	D,G	D[1][3]	D,G	D,G	D	12/20	0.16	0.06
22 Variable Static	No											
23 Variable Static	No											
24 Variable Static	No											
25 Shaft Fast Test	Yes	Comp	G	G	G	G				12/20	0.0020	16.2733
26 Shaft Fast Test	Yes	Comp	G	G	G	G				12/20	0.0010	0.1007
27 Shaft Fast Test	Yes	Comp	G	G	G	G				12/20	0.0026	0.0026
28 Shaft Fast Test	Yes	Comp	G	G	G	G				12/20	0.0029	0.1047
29 Shaft Fast Test	Yes	Comp	G	G	G	G				12/20	0.0040	0.0523
30 Shaft Fast Test	No											

Legend

D - Digital data at staggered 15 second intervals
G - Graphical continuous records

Notes

(1) Poor tracking of diaphragm re-zeroed
(2) Except as noted
(3) After variable static, 4 more 15 second readings in 60-100% range were run.
(4) Bridge hardwires broken during cable recovery
(5) Out of normal sequence - followed Shaft Fast Tests
(6) Unstable bridge readings

Typical Loading Rates

Static	10^{-3} kips/min
Quick Static	10^{-2} kips/min
Cyclic	3×10^{-1} kips/min
Variable Static	10^{-3} to 10^{-1} kips/min
Shaft Fast	5×10^{-1} kips/min

due to such amplifications are conservatively estimated to be ±15% for Pile 1, ±40% for Pile 2, ±75% for Pile 3, and ±50% for Pile 4. Because of these relatively large errors, very little could be concluded about the axial load-deflection behavior for the first series of tests. Modifications were made for the second series of tests to result in an error of less than ±2%.

Loads at the top of the test section were measured with a strain gage bridge at that level and with a backup reading of the jack pressure. Overall accuracy of the measurement of the load at the top of the test section was estimated, considering all contributing effects. The probable error in the measured capacity is the larger of ±5 kips or ±2%.

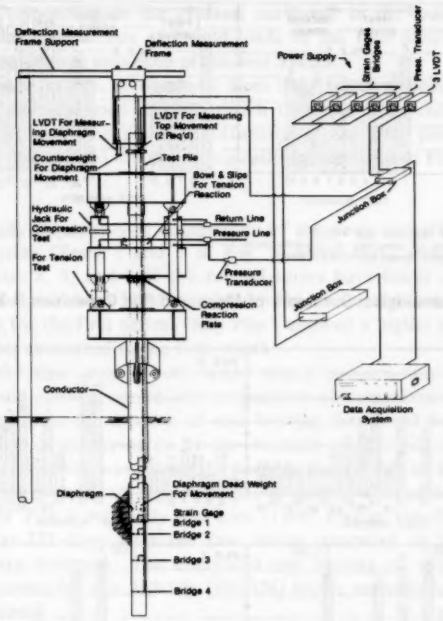

FIG. 4.—Schematic of Test Setup

Further details of pile makeup, instrumentation, test equipment, test procedures, and data accuracy were presented earlier (5) and are not repeated here.

Measured and Predicted Pile Behavior

The data from the two tests series were used to evaluate the effects of rate of loading, elapsed time after driving or previous test, and cyclic loading-on pile capacity and load-displacement response of the pile. Because each pile was by choice loaded to failure a number of times, the evaluation of the effect

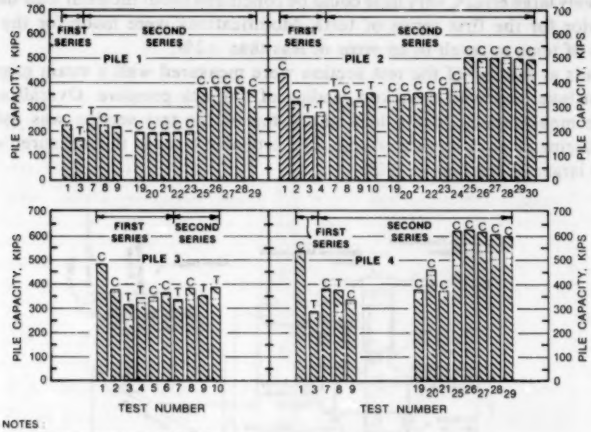

FIG. 5.—Chronological Summary of Measured Pile Capacities (1 kip = 4.45 kN)

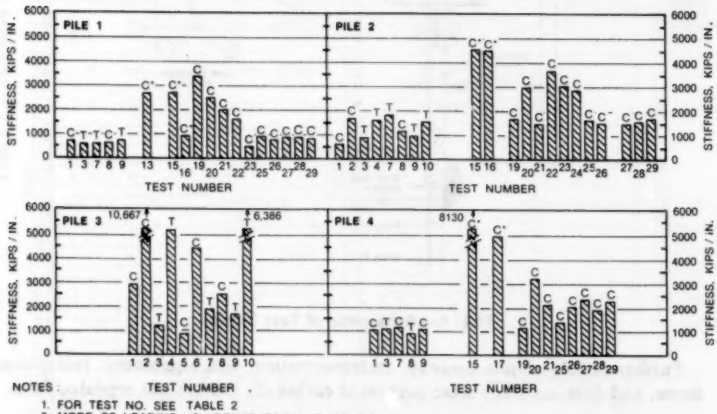

FIG. 6.—Chronological Summary of Measured Pile-Soil Stiffness (1 kip/in. = 0.175 kN/mm)

of the parameter measured subsequent to the very first test may be biased by the loading history. Therefore, in many cases qualitative rather than quantitative conclusions have to be drawn from the test data.

Comparisons were made between measured and predicted results; the latter were determined prior to evaluation of the pile test data. No effort was made in this study to modify any input data to fit computed with measured values or to develop a modified predictive method with the advantage of hindsight and test data now available.

Historical Summary of Capacity and Pile-Soil Stiffness.—The capacity of a pile can be defined in terms of either a yield or ultimate load. For this study, ultimate load was defined as the maximum load in a test, while yield was defined as the load corresponding to the greatest curvature in the load-displacement curve. The ultimate capacities and yield loads of the four piles are presented in Fig. 5 in chronological sequence of the test events.

Pile-soil stiffness values, as observed from the load-displacement records of the tests, vary with the load level at which they are measured and with the definition of stiffness. The pile-soil stiffnesses of the four piles in terms of the secant modulus at yield are chronologically summarized in Fig. 6.

Pile Capacity

Measured Static Capacity.—A comparison of the peak capacities of the first test of each series (Tests 1 and 7 in Fig. 5) show that, after adjusting for end bearing, Piles 2, 3, and 4 of the second series have lower capacities than the first series despite about 320 days of setup for the second series as compared to about 7 days for the first series. Only Pile 1 showed a higher capacity during the second series compared to the first series.

For Pile 4, the first test of both series was a compression test. Although those tests should allow a one-to-one comparison of compressive capacity due to a large setup time, the amount of end bearing that could be developed in the second series is questionable as the location of the pile tip in the first test of the second series was above its deepest penetration in the first series. Fig. 7 summarizes the residual displacements of the pile after each test sequence. The capacity of Pile 4 was only 380 kips (1,690 kN) in the first test of the second series at 327 days after the first series compared to 539 kips (2,400 kN) for the very first test. The computed end bearing of only 38 kips (170 kN) cannot account for the 159 kip (710 kN) lesser capacity in the test with greatest setup time.

A comparison of the first test of the first and second series shows the following differences relative to the first series—Pile 1: +21.6%; Pile 2: −10.2%; Pile 3: −26.8%; Pile 4: −24.1%. To make this comparison with the tension tests of the second series a computed end bearing component was deducted from the measured capacity of the first series. The relative difference increases with depth and a decrease in pile length.

The lower capacities during the second series were unexpected. The cause for the lesser capacities in the second test series as well as the low capacity of the second tests in the first series is probably due to residual strength effects. Bergemann (2) observed a similar reduction in capacity after an initial loading to failure. In this case, the friction capacity was reduced by 33%, and the reduction was not recovered even after 2 months of setup.

A "residual" strength surface, particularly for Piles 2, 3, and 4, was probably created in the first tests. If such a surface was created by the relatively large pile movements in the first tests and the reversal in pile movement due to subsequent tension and compression testing, the second series of tests would have then indicated the "frictional" resistance developed by 320 days of setup on this "prefailed" surface.

Some suggestion of residual strength development and possible strain sensitivity was evidenced by the difference in the shape of the post-peak portion of the load-deformation curves for the first few load applications and those for later load applications. Load-displacement curves for all static tests on each of the four piles are presented in Fig. 8. In the first test on each pile, the load on

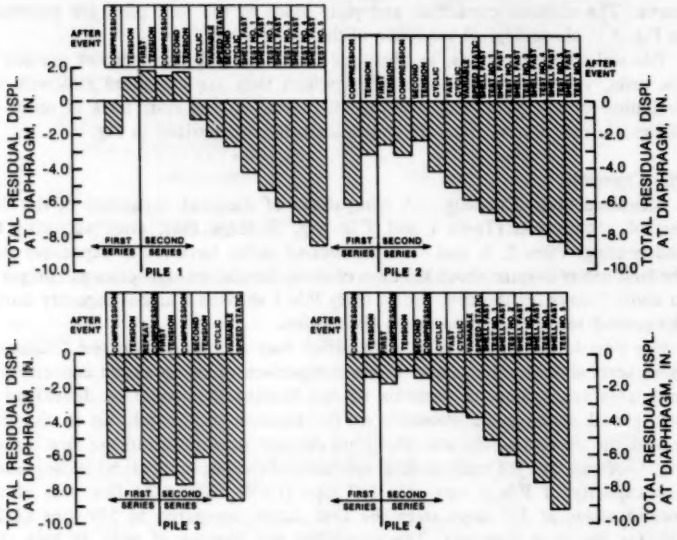

FIG. 7.—Histories of Loading and Residual Displacement (1 in. = 25.4 mm)

the test section exhibited "strain softening" after the peak load was achieved. These were all compression tests, the degree of softening was much less for Pile 1. Subsequent tests in the first series did not reveal any significant strain softening, and the load-deflection curves for the first tension and compression tests in the second series exhibited only a slight strain-softening tendency.

Strain softening behavior in the laboratory usually occurs with the development of a pronounced failure surface in the specimen, and the shear resistance at large strain is a measure of the residual strength. Stress-strain curves from simple shear tests show that the susceptibility of the soil to exhibit a strain softening behavior increased with an increase in sample depth. Similar behavior was observed for the direct shear soil-steel adhesion tests. The shape of the load-displacement curves of the pile tests and the laboratory data both support

the contention that a "residual" strength surface developed with the large pile movements during the first test. Subsequent tests results, therefore, are a measure of pile response affected by a residual strength.

Predicted Static Capacity.—Procedures to compute pile capacities have historically been developed from data on pile tests loaded to failure slowly (an elapsed time of several hours). The first test of both the first and second series was a slow test and, because of the setup time, should be least affected by the loading history. The ultimate axial capacities were computed with three methods to predict shaft friction [American Petroleum Institute (API), Burland, and Lambda (λ) methods]. For the soil conditions at the site the unit shaft friction, f, for the API method (1) is equal to the interpreted undrained shear strength, s_u. Burland (4) equates the unit skin friction to an earth pressure coefficient ($1 - \sin \bar{\Phi}$, in which $\bar{\Phi}$ = the effective angle of internal friction of the soil) and the effective overburden pressure prior to pile installation. The λ method

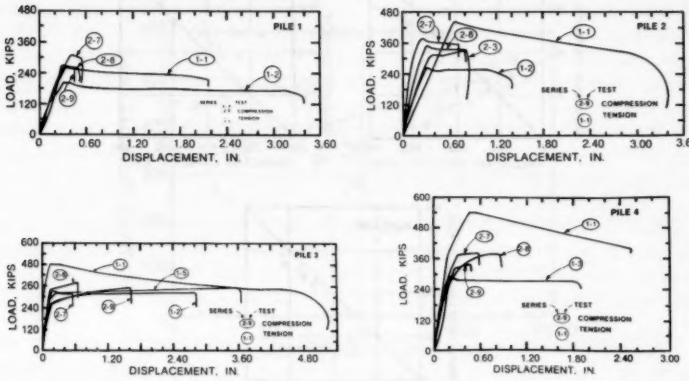

FIG. 8.—Load-Displacement Curves (1 in. = 25.4 mm; 1 kip = 4.45 kN)

is a quasi-effective stress approach in which the average unit shaft friction is related to the undrained shear strength, the effective overburden pressure, and an empirical coefficient that varies with pile penetration (10).

The undrained shear strengths used in the analysis are shown on the interpreted profile in Fig. 2. The average angle of internal friction from the laboratory tests was 25°. Effective overburden pressures equal to the mean of the range shown in Table 1 were used for the predictions. These mean effective stresses correspond to 90% consolidation for Piles 1 and 2 and 95% consolidation for Piles 3 and 4.

The computed results for each of the methods are compared in Fig. 9 with the measured axial capacities from the first compression test in the first series. Comparisons are not shown for subsequent tests as the measured results were influenced by the previous loadings to failure that are not accounted for by the prediction methods. The capacities shown for the λ method are based on a λ correlation for piles in normally consolidated soils (8).

The accuracy of the measured load was estimated to be within ±5 kips (23 kN). The uncertainty in the computed values of shaft friction for a given method can be related to the uncertainty in the undrained shear strength for the API method, the undrained shear strength and effective stress for the λ method, and the effective stress and angle of internal friction, $\bar{\Phi}$, for Burland's method. The uncertainty in computed end bearing is related to uncertainty in the bearing capacity factor, N_c, and the undrained shear strength. The value of N_c ranges from about 7 to 18.

The variations in computed values of pile capacity for the uncertainties in the soil parameters that are reflected by the range in properties in Table 1 and for independence between uncertainties are about ±10% for the API method for the piles in the upper two zones and ±20% for the other two piles, about

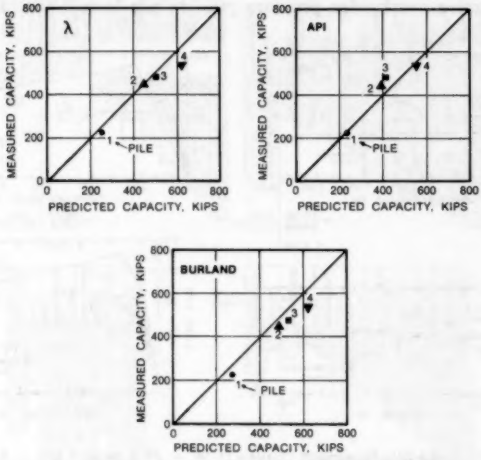

FIG. 9.—Comparison of Measured and Predicted Ultimate Capacities for First Compression Tests of First Test Series (1 kip = 4.45 kN)

±10% for the λ method, and about ±15% for Burland's procedure. The differences between the measured and predicted values are generally within the expected uncertainty for each of the methods. The variability about a mean "predicted-to-measured" ratio is less for Burland's method and greatest for the API method. The Burland and λ methods tended to overpredict the capacities. The predicted capacities for the Burland method ranged from about 109% to 123% of the measured capacities. The predicted capacities for the λ method ranged from 100% to 115% of the measured capacities; this may be due to an overestimation of the in situ effective overburden stress. The results from the API method show the least bias toward under- or overprediction.

Effect of Loading Rate.—To protect the test piles and loading equipment during the fast tests, a relief valve was installed in the hydraulic system to prevent overloads. Prior to testing, the relief valve was set to a pressure considerably

above the maximum pressure expected during testing. The valve settings, made on a 2-in. (50-mm) diam pressure gage, corresponded to 408 kips (1,815 kN) for Pile 1, 526 kips (2,340 kN) for Pile 2, and 666 kips (2,965 kN) for Pile 4. The maximum loads developed during the fast tests were much larger than those for the slower pile tests. Maximum loads obtained in the fast tests corresponded to about 93% of the relief-valve settings. The difference in load between the maximum obtained loads and the loads set on the pressure relief valve may be attributable to a premature opening of the relief valve, to inaccuracy in setting the valve, or to a combination of the two.

Loading rate was defined as the difference between yield load and load at the beginning of the test divided by the elapsed time between initiation of loading and reaching the yield load. Fig. 10 shows the ultimate capacity versus loading rate for Pile 2. Although the scatter is large, a definite trend exists. A comparison of the fast test results with the first compression test of the second series demonstrates a significant increase in capacity with loading rate. The capacities

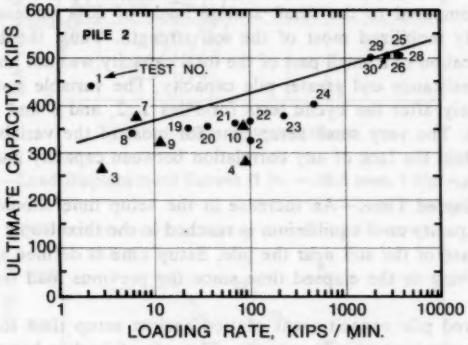

FIG. 10.—Influence of Loading Rate on Capacity (1 kip = 4.45 kN; 1 kip/min = 4.45 kN/min)

from the fast tests assume that the measured ultimate load was a measure of the pile capacity and not a measure of the load associated with an opening of the relief valve. If, however, the opening of the relief valve affected the maximum load applied to the piles, the interpretations and conclusions derived here about pile capacities are conservative.

The results showed that the ultimate pile capacity may be increased by 40% to 75% if the loading rate is increased by about three orders of magnitude. Even if the measured "slow" compressive capacity, however, is increased by the full computed end bearing due to the uncertainty in the development of the end bearing, the implied increase in ultimate capacity is not affected significantly. This 40%–75% range between results for the different piles may be due to differences in the soil properties, differences between the relative percent of the load carried in end bearing compared to shaft friction, loading history, or some other causes. Pile 4, e.g., showed the greatest increase in capacity with loading rate. In this case the fast tests were performed prior

to the variable static tests, while for the other piles the fast tests were performed after the variable static tests. The less severe loading history for Pile 4 may have contributed to the greater increase in capacity with loading rate.

Analyses with simple lumped parameter models demonstrated that the increase in resistance cannot be accounted for by inertia effects. Results of laboratory tests at different loading rates showed an increase in undrained shear strength of about 50% for a three-order magnitude increase in loading rate. Application of these results to the API pile capacity prediction method (1) suggests a corresponding 50% increase in pile capacity for a three-order magnitude increase in loading rate. Thus, the pile test results were in agreement with the laboratory measured increase in undrained shear strength for a corresponding increase in strain rate or loading rate.

The variable static tests did not reveal any significant increase in capacity even though the loading rate was one to two orders of magnitude greater than the slow tests. The variable static tests, however, were only unloaded to 46%–70% of the static capacity prior to each test. These residual seating loads, which were large compared to the small seating loads of 20% or less for the fast tests, probably mobilized most of the soil strength. Thus, the higher loading rate for application of a small part of the total capacity was not able to generate greater soil resistance and greater pile capacity. The variable static tests were run immediately after the cyclic tests for Piles 1, 2, and 3 and after the fast test on Pile 4. The very small setup time for most of the variable static tests may also explain the lack of any correlation between capacity and loading rate for these tests.

Effect of Elapsed Time.—An increase in the setup time should result in an increase in capacity until equilibrium is reached in the thixotropic and reconsolidation response of the soil near the pile. Setup time is defined as the elapsed time after driving or the elapsed time since the previous load test, whichever is less.

The measured pile capacity was plotted against setup time to evaluate the influence of setup time on pile capacity. The rate of loading has a significantly greater influence on the capacity than elapsed time for the conditions of these tests. Therefore, only results from the slower rate of loading tests were included in the evaluation, and the results of the first test of each series were neglected for this comparison for reasons discussed earlier. The data showed an increase in capacity with elapsed time of about 5% per log cycle of time. The impact of variables other than setup time for even the slower tests is greater than that of setup time precluding any quantitative conclusions on the changes in capacity with time after installation.

Effect of Cyclic Loading.—For the applied loading history, the cyclic loading appeared to have more effect on the load-displacement response than on capacity. Consequently, the effect of cyclic loading on pile capacity will be introduced in the next section on load-displacement response of the piles.

Load-Displacement Response

The load-displacement response was evaluated in terms of the secant spring constant at yield load for all of the tests and comparisons of the load-displacement curves for selected tests. The measured values ranged from about 500 kips/in. to 3500 kips/in. (87.6 kN/mm to 613 kN/mm). For any pile the variation

in the stiffness from the different tests was large. The potential relative error in the measured stiffness in the first series was about 16% to 73% due to potential errors in the displacements. Modifications were made to the instrumentation for the second test series, and these potential errors were only 2%.

Spring constants were predicted with a computer program based on elastic solutions but with slippage between the soil and pile once the limiting shear stress on the soil-pile interface was reached (9). The computed values ranged from 540 kips/in. (94.6 kN/mm) for Pile 1 to 1,120 kips/in. (196.2 kN/mm) for Pile 4.

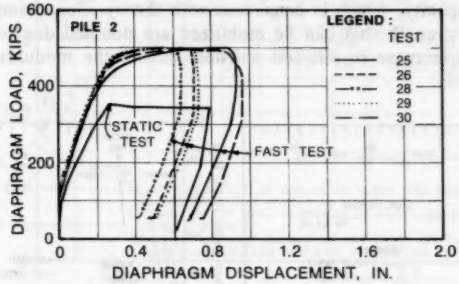

FIG. 11.—Load-Displacement Curves (1 in. = 25.4 mm, 1 kip = 4.45 kN)

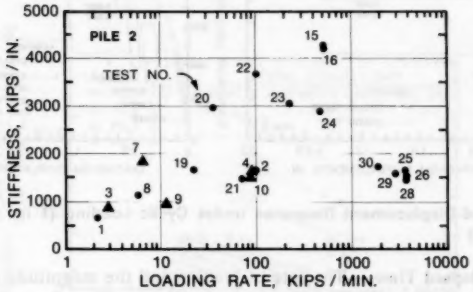

FIG. 12.—Influence of Loading Rate on Pile-Soil Stiffness (1 kip/in. = 0.175 kN/mm; 1 kip/min = 4.45 kN/min)

Effect of Loading Rate.—The load-displacement curves for Test Pile 2 of the fast tests are compared in Fig. 11 with the response of the first compression test of the second series. These comparisons illustrate a higher pile-soil stiffness for the fast tests than observed for the slower tests. The secant values at yield were plotted against loading rate in Fig. 12 to further evaluate the pile-soil stiffness. The degree of scatter is large, but some generalized trends can be deduced.

The pile-soil stiffness of the variable static tests generally exceeded the value

for the other tests even though the rate of loading was not the highest. As mentioned previously, the variable static tests were only unloaded to about 55% of their static capacity. The values of pile-soil stiffness measured in this case are for reloading between about 55% and 100% of the capacity. The reloading response for a partially unloaded pile is expected to be stiffer than that for a fully loaded pile.

A representative increase in pile-soil stiffness per decade of loading rate was 10% for Piles 1 and 2, and 25% for Pile 4. The results of Pile 3 exhibited considerable scatter, and the range in loading rate was too small to determine any trend. The increase in pile-soil stiffness with loading rate is less than the increase in capacity, which is consistent with theory. For example, if the soil modulus and strength that can be mobilized are doubled due to loading rate, the computed increase in pile-soil stiffness due to the modulus increase was only about 60%.

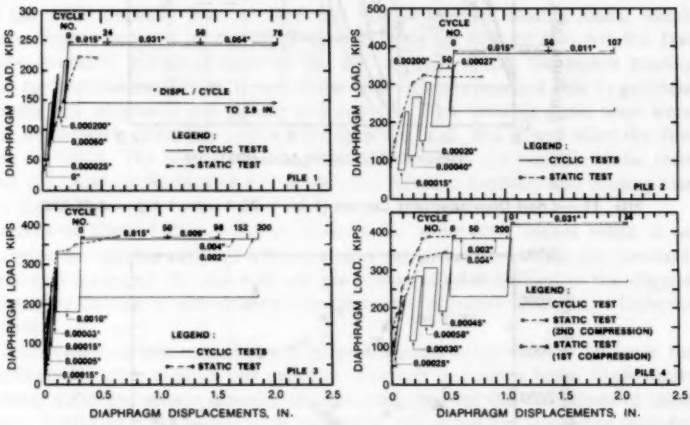

FIG. 13.—Load-Displacement Response under Cyclic Loading (1 in. = 25.4 mm; 1 kip = 4.45 kN)

Effect of Elapsed Time.—The rate of loading and the magnitude of the seating load have a significant influence on the stiffness. Therefore, only the slow tests were used to evaluate the relation between pile-soil stiffness and elapsed time after driving or the previous test. The data showed that the effect of setup time on the pile-soil stiffness was negligible.

Effect of Cyclic Loading.—The load-displacement response of the four piles subjected to one-way cyclic loading are compared in Fig. 13 with the static load-displacement curves of the last compression test prior to cyclic loading. The cumulative permanent displacement is shown in Fig. 14 against the ratio of maximum cyclic load to static capacity. Results from the Empire cyclic tests are in general agreement with data reported by Broms (3). The results demonstrated for the given load history that piles can support cyclic loads equal to and greater than the static capacity due to the higher loading rate.

The tests were load controlled. When the load reached the predetermined level, the direction of load was reversed. At higher loads, the rate of deformation had to be increased to maintain the period. Displacements began to accumulate when the maximum cyclic load reached about 80% of the static capacity, and these displacements increased appreciably when the maximum cyclic load approached 110% of the static capacity. At very high loads there was very little rebound in a load cycle.

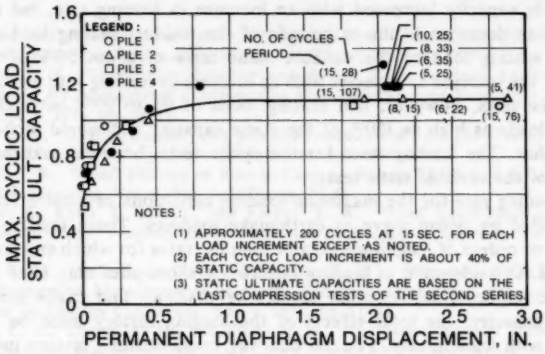

FIG. 14.—Influence of Loading on Permanent Displacement (1 in. = 25.4 mm)

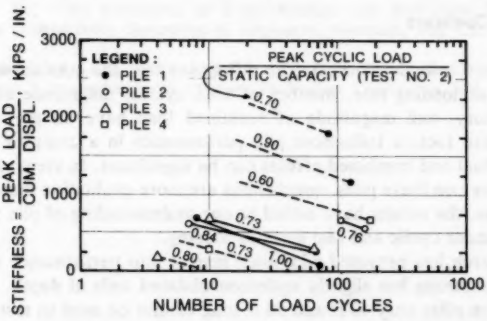

FIG. 15.—Pile-Soil Stiffness under Cyclic Loading (1 kip/in. = 0.175 kN/mm)

The pile-soil stiffness during cyclic loading was determined for several load-displacement hysteretic loops. The measured stiffness, which was defined by an average slope of the loops, is plotted in Fig. 15 against the number of load cycles and in terms of the ratio of the peak cyclic load to static capacity. The stiffness decreases with increases in the number of cycles, the cyclic load, and the pile capacity.

Data are available at Bridges 2 and 4 for the cyclic tests on Piles 3 and

4. For Pile 1, data are available at Bridge 4. These data were used to evaluate the redistribution of load in the pile during cyclic loading. The load distribution was initially transferred to deeper pile sections with each successive load cycle of a given amplitude, but after several cycles this trend was reversed and the upper portion of the pile began to carry more of the load again.

The fast tests performed after the cyclic tests gave capacities that exceeded the static capacity. Thus, the capacity after cyclic loading did not appear to be affected significantly by the type of cyclic loading used in this study.

The pile capacity increased with an increase in loading rate, but the effect appeared to decrease as the magnitude of the residual seating load increased. For the seating load of the variable static tests of about 50% of the static capacity, the increase in capacity with an increase in loading rate was negligible. The cyclic tests, however, had seating loads of up to 90% but were able to develop loads as high as 130% of the static capacity and would probably have gone higher. The loading rates for the cyclic tests, however, exceeded those of most of the variable static tests.

The loading rate for the maximum loading conditions of most offshore piles is controlled by ocean wave or earthquake loadings. These loading rates are two or four orders of magnitude greater than the rates for which static capacities are based. Consideration of loading rate for offshore piles may have important economic implications. As other studies have shown that cyclic loading may degrade capacity, the total effects of the loading history must be evaluated together with loading rate. For the one-way cyclic loading history used in this study, the combined effect of cyclic loading and rate of loading resulted in a pile resistance in excess of the static capacity.

Concluding Comments

The Empire tests demonstrate the influences that the combined but complex interaction of loading rate, number of load cycles, magnitude of cyclic load, loading history, and magnitude of sustained load have on pile performance. Each of these factors influences pile performance in a complex manner, and their individual and combined effects can be significant. In view of the complex loading history on these piles, conclusions are more qualitative than quantitative. Nevertheless, the results have added to our understanding of pile performance, especially under cyclic and fast rates of loading.

This research has provided additional insight into performance of short piles embedded in strong but slightly underconsolidated soils at depth. Results from these tests on piles only 40 ft and 50 ft long cannot be used to test conclusively the applicability of the predictive methods to piles of 200 ft to 300 ft or more in length that are used to support offshore structures. Pile test data on long piles are still needed, as the information generated by this study does not provide a complete answer to the performance of long, large-diameter piles.

Acknowledgments

The tests were funded by 14 oil companies: Amoco, Aminoil, British Petroleum, Chevron, Cities Service, Conoco, Exxon, Gulf, Marathon, Mobil, Pennzoil, Shell, Texaco, and Union. Chevron Oil Field Research Company served as

operator for the program. Chevron personnel who participated in the administration, planning, and pile installation were C. P. Besse, J. H. Bigham, Gary M. Connell, and Gordon E. Strickland. Soil borings and geotechnical engineering were performed by McClelland Engineers, Inc. Field construction was under the joint control of Chevron and TERA, Inc. Pile instrumentation, field tests, and data reduction were the responsibility of TERA, Inc.

APPENDIX.—REFERENCES

1. *Recommended Practice for Planning, Designing, and Constructing Fixed Offshore Platforms,* American Petroleum Institute, API RP 2A, 10th ed., 1979.
2. Bergemann, H., "Alternating Loading and Pulling Tests on Steel I-beam Piles," *Proceedings, 8th International Conference on Soil Mechanics and Foundation Engineering,* Vol. 2.1, 1973, pp. 13–17.
3. Broms, B. B., "Bearing Capacity of Cyclically Loaded Piles," *On The Bearing Capacity of Driven Piles,* Swedish Geotechnical Institute, No. 44–4, 1972.
4. Burland, J. B., "Shaft Friction of Piles in Clay—A Simple Fundamental Approach," *Ground Engineering,* Vol. 6, No. 3, 1973, pp. 30–42.
5. Cox, W. R., Kraft, L. M., Jr., and Verner, E. A., "Axial Load Tests on 14-inch Pipe Piles in Clay," *Proceedings, 11th Offshore Technology Conference,* Vol. 2, 1979, pp. 1147–1158.
6. Doyle, E. H., McClelland, B., and Ferguson, G. H., "Wire-Line Vane Probe for Deep Penetration Measurements of Ocean Sediment Strengths," *Proceedings, 3rd Offshore Technology Conference,* Vol. 1, 1971, pp. 21–32.
7. Ehlers, C. J., Young, A. G., and Focht, J. A., Jr., "Advantages of Using In Situ Vane Tests for Marine Soil Investigations," presented at the February 14–15, 1980 International Symposium on Marine Soil Mechanics, held at Mexico City, Mexico.
8. Kraft, L. M., Jr.. Focht, J. A., Jr., and Amerasinghe, S., "Friction Capacity of Piles Driven into Clay," 1980, submitted for publication.
9. Poulos, H. G., "The Settlement of Under-Reamed and Step-Taper Piles," *Civil Engineering Transactions,* Institution of Engineers, Australia, Vol. CE11, 1969, pp. 83–87.
10. Vijayvergiya, V. A., and Focht, J. A., Jr., "A New Way to Predict Capacity of Piles in Clays," *Proceedings, 4th Offshore Technology Conference,* Vol. 3, 1972, pp. 465–474.

JOURNAL OF THE GEOTECHNICAL ENGINEERING DIVISION

LONGITUDINAL VIBRATIONS OF EMBANKMENT DAMS

By George Gazetas,[1] A. M. ASCE

INTRODUCTION

The types of serious damage that are most frequently observed in embankment dams after strong earthquakes can be grouped into the following four categories in order of increasing frequency of occurrence (9):

1. Longitudinal cracks that develop especially near the crest due either to tensile stresses caused by the lateral vibrations of the dam or to differential settlements caused by different degrees of dynamic compaction of various dam zones (core, shell) or foundation soils.
2. Slides of soil masses from the upstream or downstream slope of the dam triggered by lateral vibrations that induce along sliding surfaces shear stresses that exceed, on the average, the shear strength of the soil.
3. Transverse cracks that develop usually near the abutment-dam interfaces either due to tensile stresses created by longitudinal vibrations of the dam or due to differential settlements of various sections of the dam in the longitudinal direction.
4. Large displacements or bearing capacity failure due to liquefaction of saturated cohesionless soils in the dam or the foundation.

Transverse cracking due to longitudinal vibrations is neither as serious damage as are the large permanent deformations caused by liquefaction or sliding, nor as frequent a phenomenon as is the development of longitudinal cracks. This perhaps explains why so little attention has been directed towards understanding the behavior of earth dams when excited in a direction parallel to their axis. In contrast, extensive experimental and theoretical research has been related to lateral vibrations of earth dams or embankments (1,2,3,4,5,7,9).

[1]Asst. Prof. of Civ. Engrg., Case Western Reserve Univ., Cleveland, Ohio 44106.

Note.—Discussion open until June 1, 1981. To extend the closing date one month, a written request must be filed with the Manager of Technical and Professional Publications, ASCE. Manuscript was submitted for review for possible publication on December 18, 1979. This paper is part of the Journal of the Geotechnical Engineering Division, Proceedings of the American Society of Civil Engineers, © ASCE, Vol. 107, No. GT1, January, 1981. ISSN 0093-6405/81/0001-0021/$01.00.

However, transverse cracks can be potentially very dangerous since they can induce uncontrolled seepage through the dam and thereby create piping failure(s). Such cracks are highly probable to occur especially at the contact surfaces of an embankment dam with its steep-sloping rock abutments, because of the different dynamic response of the two media, and because no tensile forces can develop between them. The 1/16-in. wide (1.6 mm) lateral crack which occurred at the east abutment of the Santa Felicia Dam during the San Fernando Earthquake of February 9, 1971, as reported by Abdel-Ghaffar and Scott (1) seems to have been of this nature.

The contact areas between soil and outlet works such as side spillways, sluiceways, and buried pipes are also vulnerable to tensile longitudinal stresses. Furthermore, cracking and ruptures of pipes observed after earthquakes have been attributed to the incompatibility of their displacements with the larger longitudinal deformations of the surrounding soil (9). Since many of these damages occur within the body of the dam and can easily remain undetected they may cause additional problems in the post-earthquake life of the structure. Consequently, experimental and theoretical research on the behavior of embankment dams during earthquake-induced longitudinal vibrations is urgently needed to develop methods of analysis, establish performance criteria, improve current design procedures, and invent rehabilitation techniques to ensure the safety of new or existing earth and rockfill dams during and after earthquakes.

As a first step in the aforementioned direction, this paper presents a theoretical analysis of free and forced vibrations of embankment dams. The method accounts for both dilatational and shear deformations and models the dam as a linear homogeneous triangular prism, bounded in the longitudinal direction by two vertical planes (rectangular canyon). Numerical results are presented for the natural frequencies, modal displacement, modal strain shapes, and modal participation factors. It is shown that in relatively long dams shear deformations are more important than axial deformations, whereas the reverse is true with dams that are built in narrow canyons. Two case studies are then presented in order to evaluate the ability of the presented theory to explain with reasonable accuracy observed field behavior. Natural frequencies, participation factors, and mode shapes computed with the theory for the Santa Felicia Dam in California and the Kisenyama Dam in Japan are examined in the light of observed predominant frequencies and peak response amplitudes of motions recorded during actual earthquakes (1,9). Finally the method is extended to approximately account for a realistic variation of shear modulus at various depths below the crest of the dam.

Analysis for Homogeneous Dam in Rectangular Canyon

Free Vibrations.—Let x, y, and z be the orthogonal coordinates of any point in a symmetrical earth dam built in a rectangular canyon, as shown in Fig. 1(*a*). To derive the governing equation of motion the simplifying assumption is made that normal and shear stresses, σ_x and τ_{zx}, are independent of y and, therefore, that σ_x and τ_{zx} are uniformly distributed over infinitesimal areas $b_y \cdot dz$ and $b_y \cdot dx$ respectively, as shown in Fig. 1(*b*). This assumption is reminiscent of the hypothesis of uniform shear stresses τ_{zy} over areas $b_y \cdot dx$ that is the basis of the shear-beam theory for lateral vibrations (3,4,7,9). It seems, however,

that the present hypothesis is more realistic since it does not violate the physical requirement of zero shear and normal stresses on the upstream and downstream faces of the dam, in contrast with the shear-beam assumption.

As a direct consequence of the foregoing assumption, the horizontal displacements are considered independent of y, i.e., $u = u(x, z; t)$. The differential

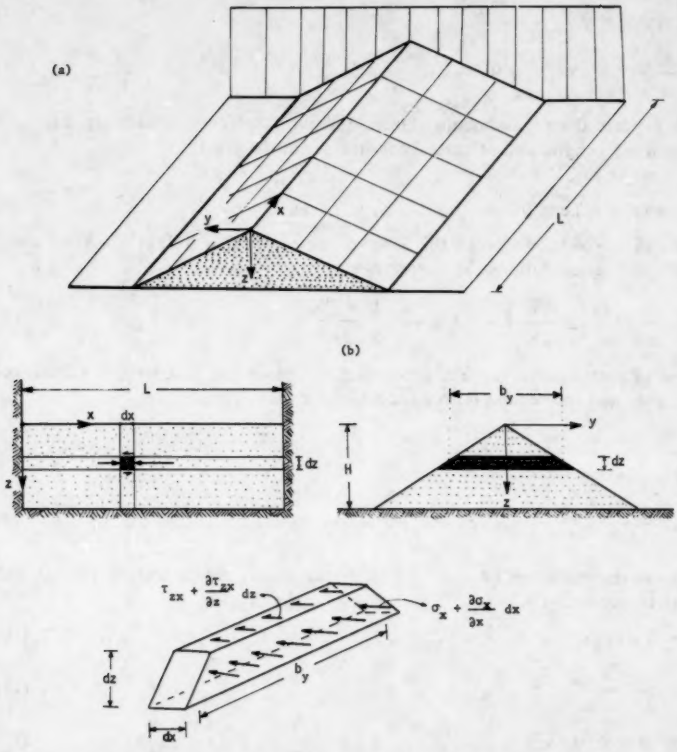

FIG. 1.—(*a*) Dam Geometry in Perspective; and (*b*) Longitudinal and Cross Section of Dam: Stresses Acting on Infinitesimal Body

equation that governs the spatial and temporal variation of u is subsequently derived from the dynamic equilibrium of an infinitesimal body of volume $b_y \cdot dx \cdot dz$ [Fig. 1(*b*)]:

$$\rho \ddot{u} - \frac{1}{z} \frac{\partial}{\partial z} \left(G z \frac{\partial u}{\partial z} \right) - \frac{\partial}{\partial x} \left(E \frac{\partial u}{\partial x} \right) = 0 \quad \ldots \ldots \ldots \ldots \ldots \ldots \quad (1)$$

in which G and E = the shear and Young's moduli of the soil, herein taken as constants throughout the dam. The three terms in Eq. 1 express respectively the inertia, shear, and axial forces acting on the said infinitesimal body.

Solutions of Eq. 1 would be physically acceptable only if they satisfy the boundary conditions:

$$u(o, z; t) = 0 \quad \ldots\ldots (2)$$

$$u(L, z; t) = 0 \quad \ldots\ldots (3)$$

$$u(x, H; t) = 0 \quad \ldots\ldots (4)$$

$$G \frac{\partial}{\partial z} u(x, z; t) \Big]_{z=0} = 0 \quad \ldots\ldots (5)$$

that express the requirements of zero relative displacement between dam and supporting canyon and of zero shear stresses at the crest.

To solve Eq. 1, let

$$u = \Phi(z)\Psi(x) \exp(i\omega t) \quad \ldots\ldots (6)$$

and call $k = \omega/C$, in which the S-wave velocity is $C = [G/\rho]^{1/2}$. After some mathematical operations Eq. 1 becomes

$$k^2 + \frac{1}{z\Phi} \frac{d}{dz} \left(z \frac{d\Phi}{dz} \right) = -2(1 + \nu) \frac{1}{\Psi} \frac{d^2\Psi}{dx^2} \quad \ldots\ldots (7)$$

Each of the terms in Eq. 1 is a constant, a^2, since the first term is a function of z only and the second term a function of x only. Thus

$$\frac{d^2\Psi}{dx^2} + \frac{a^2}{2(1 + \nu)} \Psi = 0 \quad \ldots\ldots (8)$$

$$\text{and} \quad \frac{d^2\Phi}{dz^2} + \frac{1}{z} \frac{d\Phi}{dz} + (k^2 - a^2)\Phi = 0 \quad \ldots\ldots (9)$$

The general solutions of Eqs. 8 and 9 that satisfy the boundary Eqs. 2 and 5 are respectively:

$$\Psi = B' \sin qx \quad \ldots\ldots (10)$$

$$q^2 = \frac{a^2}{2(1 + \nu)} \quad \ldots\ldots (11)$$

$$\text{and} \quad \Phi = B'' J_0(bz) \quad \ldots\ldots (12)$$

$$b^2 = k^2 - a^2 \quad \ldots\ldots (13)$$

in which B', B'' = integration constants; and $J_0(\cdot)$ = Bessel Function of the first kind and zero order.

Enforcement of the other two boundary conditions (Eq. 3 and Eq. 4) leads to

$$a_r = \frac{[2(1 + \nu)]^{1/2}}{L} r\pi; \quad r = 1, 2, 3, \ldots \quad \ldots\ldots (14)$$

$$b_n = \frac{S_n}{H}; \quad n = 1, 2, 3, \ldots \quad \ldots\ldots (15)$$

in which S_n = the roots of $J_0(S) = 0$, e.g., $S_1 = 2.4048$, $S_2 = 8.6530$, etc. The natural frequencies for longitudinal vibrations are then obtained by combining Eqs. 13, 14, and 15:

$$\omega_{nr} = \frac{C}{H}\left[S_n^2 + 2(1+\nu)\pi^2\left(\frac{H}{L}\right)^2 r^2\right]^{1/2} \quad \ldots\ldots\ldots\ldots\ldots\ldots \quad (16)$$

while the displacement shapes, normalized to a unit peak amplitude, are given by

$$U_{nr} = J_0\left(S_n \frac{z}{H}\right) \sin\left(r\pi \frac{x}{L}\right) \quad \ldots\ldots\ldots\ldots\ldots\ldots\ldots\ldots \quad (17a)$$

$$u_{nr} = U_{nr} \exp(i\omega_{nr} t); \quad n, r = 1, 2, 3, \ldots \quad \ldots\ldots\ldots\ldots\ldots\ldots \quad (17b)$$

and the normal and shear strains by

$$\epsilon_{x,nr} = \frac{\partial u_{nr}}{\partial x} = \frac{r\pi}{L} J_0\left(S_n \frac{z}{H}\right) \cos\left(r\pi \frac{x}{L}\right) \exp(i\omega_{nr} t) \quad \ldots\ldots\ldots\ldots \quad (18)$$

$$\gamma_{zx,nr} = \frac{\partial u_{nr}}{\partial z} = \frac{S_n}{H} J_1\left(S_n \frac{z}{H}\right) \sin\left(r\pi \frac{x}{L}\right) \exp(i\omega_{nr} t) \quad \ldots\ldots\ldots\ldots \quad (19)$$

Earthquake-Induced Vibrations.—During earthquake shaking that consists exclusively of vertically propagating S-waves polarized in the x direction, the longitudinal motion of the dam relative to the surrounding canyon is described by

$$\rho\ddot{u} - \frac{1}{z}\frac{\partial}{\partial z}\left(Gz\frac{\partial u}{\partial z}\right) - \frac{\partial}{\partial x}\left(E\frac{\partial u}{\partial x}\right) = \rho\,\ddot{u}_{gx} \quad \ldots\ldots\ldots\ldots\ldots\ldots \quad (20)$$

in which $\ddot{u}_{gx}(t)$ = the ground acceleration (in the x direction), and by Eqs. 2, 3, 4, and 5 (boundary conditions). The solution is obtained by modal superposition (8):

$$u(x, z; t) = \sum_{n=1,2}^{\infty} \sum_{r=1,2}^{\infty} \Gamma_{nr} U_{nr}(x, z)\, D_{nr}(t) \quad \ldots\ldots\ldots\ldots\ldots\ldots \quad (21)$$

whereby, the modal participation factor Γ_{nr} of the n, r mode is

$$\Gamma_{nr} = \frac{\int_0^H \int_0^L U_{nr} \cdot y \cdot dx \cdot dz}{\int_0^H \int_0^L U_{nr}^2 \cdot y \cdot dx \cdot dz} = \frac{8}{\pi\, r\, S_n J_1(S_n)} \quad \ldots\ldots\ldots\ldots\ldots \quad (22)$$

while the modal response $D_{nr}(t)$ is obtained from the Duhamel integral:

$$D_{nr}(t) = \frac{1}{\omega_{nr}^*} \int_0^t \ddot{u}_{gx}(t) \exp\left[-\beta_{nr}\omega_{nr}(t-p)\right] \sin\left[\omega_{nr}^*(t-p)\right] dp \quad \ldots\ldots \quad (23a)$$

$$\omega_{nr}^* = \omega_{nr}(1 - \beta_{nr}^2)^{1/2} \quad \ldots\ldots\ldots\ldots\ldots\ldots\ldots\ldots \quad (23b)$$

in which β_{nr} = damping ratio in the n, r mode.

Numerical Results

Fig. 2 demonstrates the relationship between natural frequencies, ω_{nr}, of a homogeneous dam in a rectangular canyon and the key geometric parameter, i.e., the length-to-height ratio, L/H. Specifically, Fig. 2(*a*) shows the decrease of the fundamental frequency-ratio, $\omega_{11} H/C$, as L/H increases, for two values

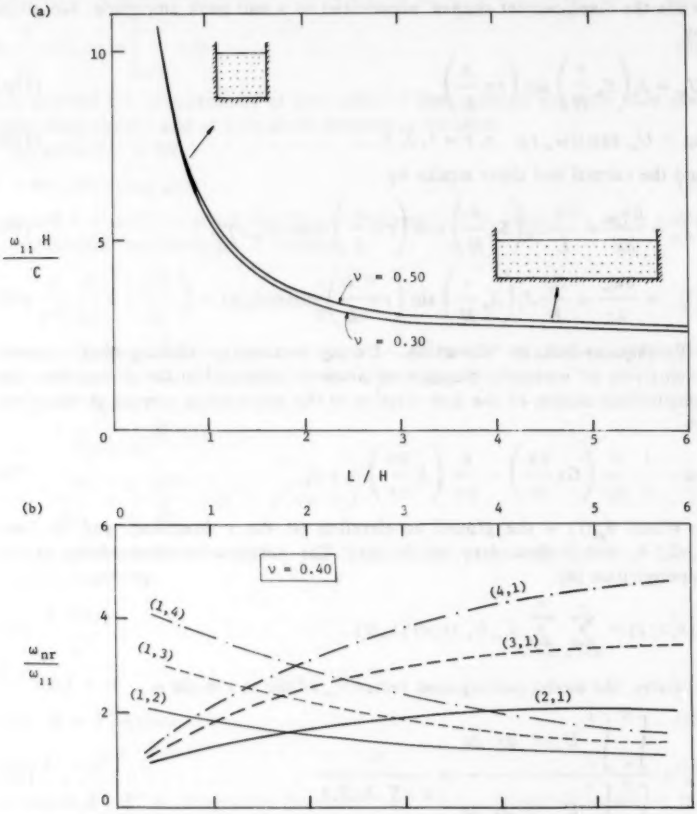

FIG. 2.—Dependence of Natural Frequencies on Length-to-Height Ratio

of Poisson's ratio, $\nu = 0.30$ and $\nu = 0.5$. One can clearly distinguish two regions in the frequency-ratio spectrum, corresponding to "narrow" or "wide" canyons, respectively. When L/H is less than about 1.5 ("narrow" canyon) $\omega_{11} H/C$ is inversely proportional to L/H, whereas when L/H is greater than about 2 ("wide" canyon) $\omega_{11} H/C$ is practically independent of L/H. The following expressions can be derived from Fig. 2(*a*) for the fundamental period in

longitudinal vibrations of "narrow" or "long" dams:

$$T_{11} \simeq 1.20\frac{L}{C} \quad \text{for} \quad \frac{L}{C} \leq 1.5 \quad \ldots\ldots\ldots\ldots\ldots\ldots\ldots\ldots \quad (24a)$$

and $$T_{11} \simeq 2.80\frac{H}{C} \quad \text{for} \quad \frac{L}{H} \geq 2 \quad \ldots\ldots\ldots\ldots\ldots\ldots\ldots\ldots \quad (24b)$$

Eq. 24*a* states that, for a narrow dam, T_{11} is independent of the height, H, and is only a function of the length, L, and the S-wave velocity, C. This result can be compared with the fundamental period in axial vibrations of a uniform rod fixed at both ends and having a Poisson's ratio $\nu = 0.40$:

$$T_1 \simeq 1.19\frac{L}{C} \quad \ldots\ldots\ldots\ldots\ldots\ldots\ldots\ldots\ldots\ldots\ldots\ldots \quad (25a)$$

The similarity of Eq. 24*a* and Eq. 25*a* suggests that axial deformations are more significant than shear deformations in narrow dams.

The reverse appears to be true in long dams; T_{11} depends only on the height, H, of the dam and Eq. 2 is reminiscent of the fundamental period of a two dimensional wedge-shaped beam due to lateral shear vibrations (3,4,7):

$$T_1 \simeq 2.60\frac{H}{C} \quad \ldots\ldots\ldots\ldots\ldots\ldots\ldots\ldots\ldots\ldots\ldots\ldots \quad (25b)$$

Therefore, shear deformations are more important than axial deformations in relatively long dams.

Another way of studying the relative significance of axial versus shear deformations is by considering the peak-strain ratio

$$(SR)_{nr} = \frac{\max \epsilon_{x,nr}}{\max \gamma_{zx,nr}} \quad \ldots\ldots\ldots\ldots\ldots\ldots\ldots\ldots\ldots\ldots\ldots\ldots \quad (26)$$

From Eqs. 18 and 19:

$$(SR)_1 \simeq 3.10\frac{H}{L} \quad \ldots\ldots\ldots\ldots\ldots\ldots\ldots\ldots\ldots\ldots\ldots\ldots \quad (26a)$$

which also demonstrates that as the canyon becomes wider (H/L decreases) the importance of shear deformations increases.

Notice also in Fig. 2(*a*) and in Eqs. 24 that Poisson's ratio, ν, has a practically negligible effect on the fundamental frequency. Also negligible is the influence of ν on the higher frequencies. Only results for a typical value of $\nu = 0.40$ are thus shown hereafter, except when otherwise stated.

Fig. 2(*b*) portrays the variation with L/H of the ratio ω_{nr}/ω_{11} of six higher frequencies (n, $r = 1, 2, 3, 4$) over the fundamental frequency. Two conclusions can be drawn: (1) Successive natural frequencies are very close to each other, e.g., a dam with $L/H = 2$ has $\omega_{12} \simeq \omega_{21} \simeq 1.60\ \omega_{11}$, $\omega_{13} \simeq 1.40\ \omega_{12}$, $\omega_{31} \simeq 1.06\ \omega_{13}$, etc., therefore, in general, no reliable estimate of response parameters can be obtained through empirical combination(s) of the maximum modal responses that are determined from a design spectrum (8). Instead, superposition of time histories of modal responses (as Eq. 21) must be performed; and (2)

the ratio ω_{nr}/ω_1 is an increasing or decreasing function of L/H depending on whether n is larger or smaller than r. When $n = r$, the ratio [not shown in Fig. 2(*b*)] has an approximately constant value, i.e., independent of L/H (e.g., $\omega_{22}/\omega_{11} \simeq 2.15$, $\omega_{13}/\omega_{11} \simeq 3.30$, etc.).

Finally, Fig. 3 shows in perspective the deformation of an earth dam in the

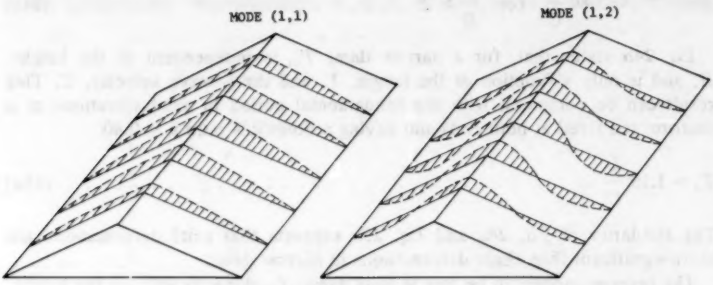

FIG. 3.—Distortion of Dam Vibrating in Two Natural Modes (perspective)

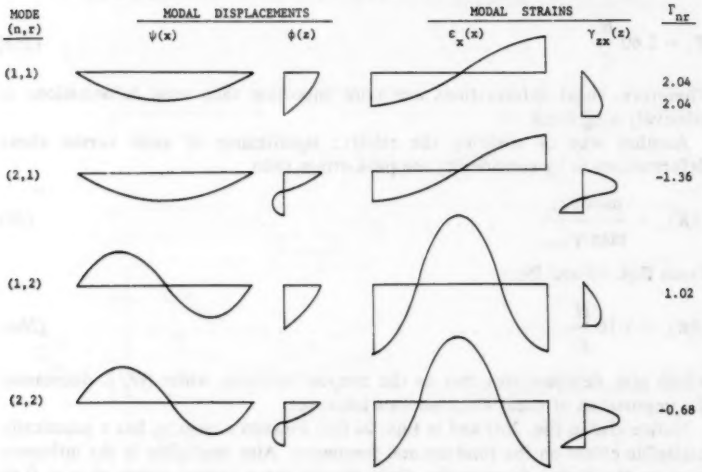

FIG. 4.—Modal Displacement and Modal Strain Components of First Two Symmetric and First Two Antisymmetric Modes

first two symmetrical modes of longitudinal vibrations [(1,1) and (2,1)] and Fig. 4 displays the x and z components of modal displacement shapes with the corresponding axial and shear components of modal strain shapes and the mode participation factors. It can be seen that maximum axial strains (which are of major concern with longitudinal vibrations) develop at the crest level of the abutment dam interface. Significant contributions to these strains come

from both symmetric ($r = 1$) and antisymmetric ($r = 2$) modes of vibration. Maximum shear strains develop at points with $x = L/2$ (middle section) and depth $z \simeq 0.75\ H$ or $0.34\ H$ etc. depending on the mode of vibration ($n = 1$ or 2 etc.).

Case Study I: Santa Felicia Earth Dam

Abdel-Ghaffar and Scott (1) have reported the analyses of two "complete" records of the response of Santa Felicia Dam in Southern California during

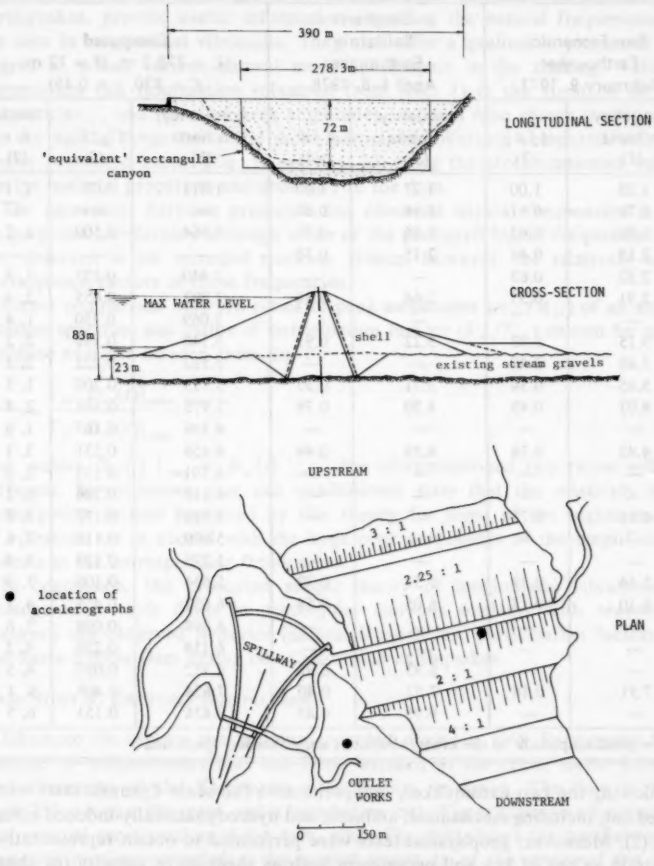

FIG. 5.—Santa Felicia Dam (1)

the San Fernando Earthquake of February 9, 1971 ($M = 6.5$, $R = 33$ km) and the Southern California Earthquake of April 8, 1976 ($M = 5$, $R = 14$

km). Santa Felicia Dam is a modern rolled-fill embankment whose geometric characteristics are shown in Fig. 5 (reproduced from Ref. 1). The dam, located 65 km northwest of Los Angeles, is approx 83 m high above its lowest foundation, 61 m above the original stream bed, and 390 m long at the crest. It has a central impervious core and pervious shells upstream and downstream. All materials are of alluvial origin.

TABLE 1.—Comparison between Computed and Observed Natural Frequencies and Participations: Santa Felicia Dam, California

San Fernando Earthquake: February 9, 1971		Southern California Earthquake: April 4–8, 1976		Computed (L = 278.3 m, H = 72 m, C = 230, ν = 0.45)		
Frequency, in hertz (1)	A/A_{11} (2)	Frequency, in hertz (3)	A/A_{11} (4)	Frequency, in hertz (5)	Γ_{nr}/Γ_{11} (6)	Mode n, r (7)
1.35	1.00	1.27	1.00	1.411	1.00	1, 1
1.70	0.61	1.66	0.67	—	—	—
1.86	0.62	1.86	0.73	1.864	0.500	1, 2
2.15	0.44	2.15	0.38	—	—	—
2.32	0.62	—	—	2.440	0.333	1, 3
2.91	0.53	2.64	0.38	2.893	0.655	2, 1
—		—		3.069	0.250	1, 4
3.15	0.53	3.22	0.91	3.140	0.332	2, 2
3.49	0.49	—	—	3.512	0.222	2, 3
3.85	0.34	3.71	0.55	3.725	0.200	1, 5
4.03	0.43	4.20	0.79	3.975	0.166	2, 4
—	—	—	—	4.396	0.167	1, 6
4.42	0.36	4.59	0.44	4.456	0.531	3, 1
—	—	—	—	4.501	0.133	2, 5
—	—	—	—	4.619	0.266	3, 2
4.88	0.75	—	—	4.880	0.177	3, 3
—	—	—	—	5.070	0.111	2, 6
—	—	—	—	5.223	0.133	3, 4
5.44	0.39	5.57	0.79	5.634	0.106	3, 5
6.10	0.17	6.05	0.54	6.037	0.455	4, 1
—	—	—	—	6.098	0.098	3, 6
—	—	—	—	6.158	0.228	4, 2
—	—	6.93	0.92	6.952	0.091	4, 5
7.91	0.18	7.52	0.40	7.624	0.405	5, 1
—	—	9.96	0.83	9.838	0.153	6, 5

[a] A = peak amplitude of the crest/abutment amplification spectrum.

Following the two earthquakes, comprehensive full-scale dynamic tests were carried out, including mechanical, ambient, and hydrodynamically-induced vibrations (2). Moreover, geophysical tests were performed to obtain representative low-strain values of key soil parameters such as shear-wave velocity (or shear modulus) and Poisson's ratio (1). Wave velocity estimates were also obtained from observed resonant frequencies of lateral vibrations, utilizing existing shear-beam theories (3,7). It was suggested that the average velocity of the

Santa Felicia dam lies between approx 220 m/sec and 270 m/sec, while a Poisson's ratio equal to 0.45 seems reasonable.

An "equivalent" dam in a rectangular canyon shown in Fig. 1(*a*) is chosen to approximate the actual dam geometry. Its dimensions are: $L = 278.3$ m and $H = 72$ m. Shear-wave velocity is taken equal to 230 m/s, i.e., near the lower bound of the suggested range, as is appropriate for relatively strong earthquake motions that are analyzed here.

The ratios of Fourier Spectra, i.e., Amplification Spectra, computed from the two pairs of parallel-to-the-dam-axis components of motions that were recorded at the middle of the crest and the right abutment during the two earthquakes, provide useful information regarding the natural frequencies of the dam in longitudinal vibrations. They also offer a qualitative picture of the degree to which various natural modes participate in the shaking. Table 1 summarizes this information (obtained from Ref. 1) in the form of natural frequencies, f, and ratios of peak amplitudes, A/A_{11}. Also shown in this table are the natural frequencies and mode participation factors computed with the theory presented herein (Eq. 16 and Eq. 22) using the aforementioned values for the material properties and geometry of the dam.

The agreement between predicted and observed natural frequencies is for all purposes satisfactory although some of the predicted higher frequencies are not observed in the recorded motions. Notice, however, the relatively small participation factors of these frequencies.

Direct comparison between ratios of peak amplitudes (A_{nr}/A_{11}) of an amplification spectrum and ratios of participation factors (Γ_{nr}/Γ_{11}) cannot be made Because as it can be seen from Eq. 21

$$\frac{A_{nr}}{A_{11}} = \frac{\Gamma_{nr}}{\Gamma_{11}} \frac{D_{nr}(t)|_{\max}}{D_{11}(t)|_{\max}} \quad \ldots\ldots\ldots\ldots\ldots\ldots\ldots\ldots\ldots\ldots\ldots\ldots \quad (27)$$

and, unless $D_{nr}(t)\,|_{\max} = D_{11}(t)\,|_{\max}$, the aforementioned two ratios will be different. Nevertheless, one can qualitatively state that the relatively large participation factors predicted by this theory for some of the higher modes of vibration are in accord with the large peak amplitudes of the amplification spectra at the corresponding frequencies.

In conclusion, the presented simple theory of longitudinal vibrations of homogeneous earth dams in rectangular canyons explains with reasonable accuracy the observed behavior (natural frequencies, participation factors) of the Santa Felicia Dam during two Californian earthquakes.

Case Study II: Kisenyama Rockfill Dam

Okamoto (9) reports the motions recorded during a 1969 Earthquake by a number of seismometers that had been installed at the crest, slope, interior, and abutments of the Kisenyama rockfill dam, in Japan. The dam is 95 m high, 255 m long at the crest, and is founded on rock. Fig. 6(*a*) shows a longitudinal and vertical cross section of the dam, while Fig. 6(*b*) shows the parallel-to-the-dam-axis motions recorded at the ground (point 1), at the center of the crest (point 2), and at 25 m below the crest in the clay-core (point 3). The earthquakes occured at the northwestern part of the Giru Prefecture on September 9, 1969, shortly after construction of the dam had been completed. Visual examination

of the records reveals that essentially only the fundamental and a few higher modes of the dam are excited; the motions (at point 2 and point 3) are very nearly sinusoidal with an average period $T = 0.42$ sec. Also apparent is the huge amplification of the motion at the crest (point 2), whereas at a relatively shallow depth of approximately $(1/3)$ H from the crest (point 3), the motion is only moderately higher than the ground motion (point 1). The distribution with depth from the crest of the peak recorded accelerations is depicted in Fig. 6(*c*) (black points).

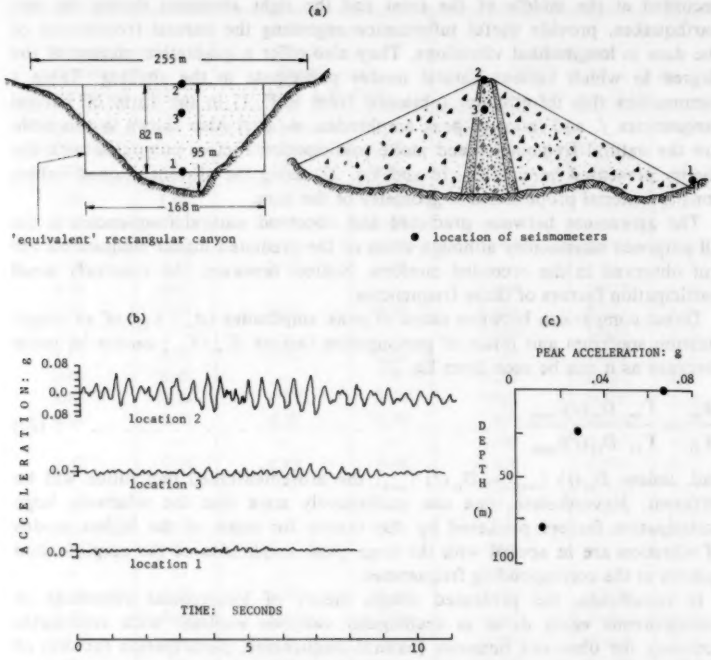

FIG. 6.—Kisenyama Rockfill Dam: (*a*) Geometry; (*b*) Accelerograms in Dam and on Ground; and (*c*) Variation of Peak Acceleration with Depth from Crest

Similar trends are observed in the normal-to-the-dam-axis records (shown in Ref. 9): (1) Nearly sinusoidal motions with an average period $T \simeq 0.48$ sec; and (2) large amplification of the motion near the crest.

Estimation of S-Wave Velocity.—On the basis of the observed fundamental period $T = 0.42$ sec, the theory of longitudinal vibrations of embankment dams presented in this paper can establish an "effective" value of the average S-wave velocity, consistent with the experienced level of shear deformations during this particular earthquake. This velocity can then be utilized to explain the actual response of the dam.

An "equivalent" dam in a rectangular canyon is chosen to approximate the actual geometry, as sketched in Fig. 6(*a*). Its dimensions are $L \simeq 168$ m and $H \simeq 82$ m. Poisson's ratio is taken as $\nu \simeq 0.25$. This is believed to be a representative value for rockfill dams immediately after construction, i.e., before the water of the lake has saturated the clay core.

Now, substituting $T_{11} = 0.42$ sec and the aforementioned geometric and material properties in the frequency relation (Eq. 16) gives:

$$C = \frac{2\pi H}{T_{11}} \left[S_1^2 + 2(1+\nu)\pi^2 \left(\frac{H}{L}\right)^2 \right]^{-1/2}$$

$$\simeq \frac{2\pi(82)}{(0.42)} \left[(2.405)^2 + 2(1.25)\pi^2 \left(\frac{82}{168}\right)^2 \right]^{-1/2} \quad \ldots\ldots\ldots\ldots\ldots\ldots \quad (28)$$

or $C = 359$ m/sec. The theory of lateral shear vibrations of embankment dams in a rectangular canyon (3,7) is subsequently used in connection with the observed fundamental period $T \simeq 0.48$ sec to check the accuracy of the preceding value of velocity. Solving for C, the corresponding frequency equation, e.g., Eq. 12 in Ref. 3, one obtains:

$$C = \frac{2\pi H}{T_{11}} \left[S_1^2 + \pi^2 \left(\frac{H}{L}\right)^2 \right]^{-1/2} \simeq \frac{2\pi(82)}{0.48} \left[(2.405)^2 + \pi^2 \left(\frac{82}{168}\right)^2 \right]^{-1/2} \quad (29)$$

or $C = 375$ m/sec. The two backfigured values of C are in fairly good agreement with each other (difference ≃4%). Moreover, 359 m/sec–375 m/sec is a realistic range for the S-wave velocity of a rockfill dam experiencing moderate levels of excitation (≃0.10 *g* peak-crest acceleration in the lateral direction; and ≃0.07 *g* in the longitudinal direction).

The natural periods of the two higher symmetric modes of vibrations are obtained by means of Fig. 2(*b*) (or through Eq. 16):

$$T_{21} \simeq \frac{T_{11}}{1.68} \simeq 0.25 \text{ sec} \quad \ldots\ldots\ldots\ldots\ldots\ldots\ldots\ldots\ldots\ldots \quad (30a)$$

$$T_{31} \simeq \frac{T_{11}}{2.58} \simeq 0.16 \text{ sec} \quad \ldots\ldots\ldots\ldots\ldots\ldots\ldots\ldots\ldots\ldots \quad (30b)$$

One can easily identify these two modes with some of the peaks of the recorded motions, e.g., the crest accelerogram (point 2) at time $t \simeq 2$ sec and in the time interval between 4 sec and 5 sec consists of cycles having periods around 0.20 sec. Note, also, that the higher antisymmetric modes [(1,2), (1,3), etc.] have a negligible contribution to the motion of points 2 and 3 because they are located close to the central cross section of the dam, i.e., at $x = L/2$.

Distribution of Peak Responses along Height of Dam.—To explain the sharp increase of the motion near the crest of the dam in comparison with the motion at a depth of only 25 m (≃0.305 H) from the crest, one can use the presented theory to compute the acceleration ratio

$$AR = \frac{\max \ddot{u}_2(t)}{\max \ddot{u}_3(t)} \quad \ldots\ldots\ldots\ldots\ldots\ldots\ldots\ldots\ldots\ldots \quad (31)$$

The acceleration time histories at points 2 and 3, $\ddot{u}_2(t)$ and $\ddot{u}_3(t)$, can be numerically obtained by means of Eq. 21 after evaluation of the Duhamel integral (Eq. 23). Unfortunately, however, the ground record $\ddot{u}_{gx}(t)$ is not available in digitized form and in order to roughly estimate AR the response spectrum approach (8) is used with the following two simplifying assumptions: (1) Only the first three symmetric natural modes ($n = 1, 2, 3$; $r = 1$) participate in the motion; and (2) the spectral accelerations, S_a, that correspond to each of the three first natural periods are all equal. The first assumption is by no means arbitrary, as it is evident from the appearance of the two accelerograms and the previous

TABLE 2.—Predictions of Peak Acceleration Distribution in Kisenyama Rockfill Dam in Japan (9)

No	Rule of Combining Modal Maxima: Expression	'HOMOGENEOUS' THEORY $\frac{\max \ddot{u}_2}{S_a}$	'HOMOGENEOUS' THEORY $\frac{\max \ddot{u}_3}{S_a}$	'HOMOGENEOUS' THEORY AR	'INHOMOGENEOUS' THEORY $\frac{\max \ddot{u}_2}{S_a}$	'INHOMOGENEOUS' THEORY $\frac{\max \ddot{u}_3}{S_a}$	'INHOMOGENEOUS' THEORY AR
	ASSUMPTION: $S_a(T_{11}) = S_a(T_{21}) = S_a(T_{31}) \equiv S_a$						
1	$\sqrt{\sum_{i=1}^{3} Q_i^2}$	2.67	1.86	1.43	3.46	1.46	2.37
2*	$\sqrt{\sum_{i=1}^{3} Q_i^2 + \sum\sum_{i=j} \frac{Q_i Q_j}{1+\varepsilon_{ij}^2}}$	2.61	1.82	1.44	3.36	1.43	2.33
3	$Q_1 + \frac{1}{2}\sqrt{\sum_{i=2}^{3} Q_i^2}$	2.90	2.06	1.40	3.41	1.62	2.10
	ASSUMPTION: $S_a(T_{21}) = S_a(T_{31}) = 2 \cdot S_a(T_{11}) \equiv 2 \cdot S_a$						
1	$\sqrt{\sum_{i=1}^{3} Q_i^2}$	3.99	2.11	1.88	6	1.67	3.57

OBSERVED RATIO: AR = 2.34

* $\varepsilon_{ij} = \frac{\omega_i' - \omega_j'}{\beta_j' \omega_i + \beta_j' \omega_j}$, $\beta_i' = \beta_i + \frac{2}{\omega_i t}$, $\omega_i' = \omega_i [1-\beta_i^2]^{1/2}$ [Ref. 7]

analysis regarding the natural periods of the dam. However, since the details of the response spectrum are unknown, the second assumption can only be considered as a crude, although reasonable, simplification. Its justification stems from the observation (8,9) that usually damped acceleration spectra exhibit a more or less constant value in the period range between 0.16 sec and 0.42 sec, i.e., in the range of the three natural periods of interest. This would especially be so for the large value of critical damping ratio (of the order of 5%–10%) that most probably developed in the soil during this particular earthquake.

For each of the two points (2 and 3) the maximum acceleration due to each

of the three symmetric modes is obtained from

$$Q_n = \max \ddot{u}_{n1} = \Gamma_{n1} U_{n1} S_a; \quad n = 1, 2, 3 \quad \ldots \quad (32)$$

in which the participation factors, Γ_{n1}, and modal shapes, U_{n1}, of the $(n, 1)$ mode are obtained from Eqs. 22 and 17, respectively. The individual modal maxima are then combined by three empirical rules to provide an estimate of the overall expected peak accelerations. Table 2 displays the results and explains the expressions of the three rules. The "square root of the sum of the squares" (SRSS) is the most popular of these rules (8,9) but it probably overestimates the total-peak response in this case because of the proximity of the natural frequencies of the dam (a phenomenon already addressed in a previous section). The second rule, suggested by Rosenblueth (8), is perhaps more appropriate since it accounts for the interaction between modal contributions. Finally, the third rule attempts to reflect the greater importance of the fundamental mode, as seen in the two records.

The results of Table 2 demonstrate that the simple theory of longitudinal vibrations, as presented so far, cannot adequately explain the observed high amplification of the seismic motion near the crest. All three rules yield quite similar acceleration ratios not exceeding 1.44, which is only 60% of the ratio of recorded peak accelerations: $0.68/0.29 \simeq 2.34$. Of course, one might argue that higher spectral accelerations at the second and third periods (0.25 sec and 0.16 sec) would have favored the corresponding higher modes and, thus, led to prediction of sharper near-crest amplification. Nevertheless, even if one assumes $S_a(T_{21}) = S_a(T_{31}) = 2 \cdot S_a(T_{11})$, the resulting acceleration ratio will not exceed the value of 1.88 (shown also in Table 2). Larger differences in the spectral accelerations (than the factor 2 implies) are highly improbable given the relatively large amount of damping the dam must have experienced during the earthquake. After all, the two records bear no evidence whatsoever of any predominance of the higher modes. Note, furthermore, that lateral vibrations exhibited a similarly sharp amplification near the crest (8), as mentioned previously, although the corresponding natural periods (0.48 sec, 0.235 sec, and 0.158 sec) differ somewhat from the periods of longitudinal vibrations.

In conclusion, the simple theory that was previously presented cannot explain the distribution of peak responses along the height of the dam. It is believed the soil inhomogeneity, which the theory does not account for, is the primary factor that causes its failure.

Simple Model that Accounts for Soil Inhomogeneity

Shear modulus even within a uniform mass of soil is not constant but increases approximately as the square-root of the effective normal octahedral stress: $G \sim (\sigma_0')^{1/2}$. Plane-strain finite-element analyses of the static stress distribution in typical dam cross sections (Ref. 5) suggest in a reasonably consistent way that, with good accuracy, the average σ_0' across the dam width is an increasing function of the distance from the crest:

$$\sigma_0' \sim z^{4/3} \quad \ldots \quad (34)$$

Thus, it appears that the average shear modulus across the width of a dam increases as the two-third power of the depth z. The result of geophysical

investigations on numerous earth and rockfill dams in the United States and Japan have confirmed this form of variation of soil stiffness in embankment-type dams (5,6). The writer (4,5) has recently presented a theory of lateral shear vibrations of earth dams whose modulus varies in proportion to $z^{2/3}$. Successful evaluation of this theory in the light of recorded responses of several dams from United States, Japan, and Yugoslavia during earthquake, forced, and ambient vibrations (5,6), offers additional indirect evidence of the appropriateness of Eq. 34.

It is concluded that embankment dams are inhomogeneous in the vertical direction. It would, therefore, be necessary to modify the presented theory of longitudinal vibrations in order to account for an S-wave velocity that increases with depth according to:

$$\frac{C}{C_m} = \left(\frac{z}{H}\right)^{1/3} \quad \text{(34)}$$

in which C_m = the velocity at the base of the dam, i.e., at $z = H$.

Exact analytical solution of the governing differential equation of free vibrations (Eq. 1) is impossible if the soil properties are described by Eq. 34 and by a constant Poisson's ratio. A simple approximate solution can, however, be obtained by heuristically combining the solution of two extreme cases: (1) The case of a "very" long dam; and (2) the case of a "very" narrow dam. As explained previously (Eqs. 24 and 26), shear deformations are predominant in case 1, whereas axial deformations are predominant in case 2. Accordingly, in the first case, Eq. 1 is simplified to

$$-\rho\omega^2\Phi \simeq \frac{1}{z}\frac{d}{dz}\left(Gz\frac{d\Phi}{dz}\right);$$

$$\text{with} \quad G = G(z) = \rho\, C^2 = \rho\, C_m^2\left(\frac{z}{H}\right)^{2/3} \quad \text{(35)}$$

and in the second case to

$$-\rho\omega^2\Psi \simeq 2(1+\nu)\,\bar{G}\frac{d^2\Psi}{dx^2} \quad \text{(36)}$$

with $\bar{G} = (6/7)^2\,\rho\,C_m^2$ being the average shear modulus.

The exact solution of Eq. 35 that satisfies the boundary conditions (Eq. 4 and Eq. 5) is

$$\Phi_n(z) = \frac{1}{z^{2/3}}\sin\left\{n\pi\left[1-\left(\frac{z}{H}\right)^{2/3}\right]\right\}; \quad n = 1, 2, 3, \ldots \quad \text{(37)}$$

and the corresponding eigenvalues are

$$\omega_n = \frac{7\pi}{9}\frac{\bar{C}}{H}n; \quad n = 1, 2, 3, \ldots \quad \text{(38)}$$

in which $\bar{C} = (6/7)\,C_m$ is the average S-wave velocity. The reader is referred to Ref. 4 for a detailed derivation of this solution. Direct substitution of Eq. 37 and Eq. 38 in Eq. 35 is, however, sufficient to convince of its correctness.

The solution of Eq. 36 and the corresponding and eigenvalues are

$$\Psi_r(x) = \sin\left(r\pi\frac{x}{L}\right) \quad \ldots\ldots\ldots\ldots\ldots\ldots\ldots\ldots\ldots\ldots \quad (39)$$

$$\omega_r = \pi\,[2(1+\nu)]^{1/2}\frac{\bar{C}}{L}r; \quad r = 1, 2, 3, \ldots \quad \ldots\ldots\ldots\ldots\ldots\ldots\ldots \quad (40)$$

In heuristic fashion, guided by the form of Eqs. 16 and 17, one can combine Eqs. 37–39 and Eqs. 38–40 to obtain approximate general formulas for the longitudinal mode shapes and natural frequencies of an embankment dam whose moduli increase with the 2/3 power of depth:

$$U_{nr} \simeq \frac{1}{z^{2/3}}\sin\left\{n\pi\left[1-\left(\frac{z}{H}\right)^{2/3}\right]\right\}\sin\left(\frac{r\pi x}{L}\right) \quad \ldots\ldots\ldots\ldots\ldots\ldots\ldots \quad (41)$$

$$\omega_{nr} \simeq \frac{\bar{C}}{H}\left[\left(\frac{7\pi}{9}n\right)^2 + 2(1+\nu)\pi^2\left(\frac{H}{L}\right)^2 r^2\right]^{1/2}; \quad n, r = 1, 2, 3, \ldots\ldots \quad (42)$$

The modal participation factor due to earthquake shaking that consists of vertically propagating waves is also given here:

$$\Gamma_{nr} = \frac{8}{\pi^2 nr} \quad \ldots\ldots\ldots\ldots\ldots\ldots\ldots\ldots\ldots\ldots\ldots\ldots\ldots \quad (43)$$

Notice that despite its approximate character, the preceding solution is exact in the two limiting cases of $L/H \to 0$ (narrow dam) and of $L/H \to \infty$ (long dam). It is moreover believed that for intermediate ranges of the L/H ratio, Eqs. 41 and 42 describe the behavior of the dam more accurately than Eqs. 16 and 17, since the former capture both the two dimensional character of the response and the inhomogeneous nature of the material properties.

Comparison of Eq. 42 and Eq. 16, portrayed in Fig. 7(*a*), reveals that the two theories (hereafter referred to as "homogeneous" or "inhomogeneous") predict very similar natural frequencies. The maximum discrepancy between fundamental frequencies is only 1.6%, in the extreme case of $L/H = \infty$; it tends to zero as L/H decreases. Larger discrepancies are observed with the higher modes, as the inhomogeneous theory predicts frequencies that are closer to the fundamental frequency, in comparison with the higher frequencies of the homogeneous theory (Eq. 16), e.g., for a very long dam Eq. 42 yields

$$\frac{\omega_{21}}{\omega_{11}} \simeq 2 \quad \text{and} \quad \frac{\omega_{31}}{\omega_{11}} \simeq 3 \quad \ldots\ldots\ldots\ldots\ldots\ldots\ldots\ldots\ldots\ldots \quad (44a)$$

whereas Eq. 16 gives

$$\frac{\omega_{21}}{\omega_{11}} \simeq 2.3 \quad \text{and} \quad \frac{\omega_{31}}{\omega_{11}} \simeq 3.6 \quad \ldots\ldots\ldots\ldots\ldots\ldots\ldots\ldots\ldots\ldots \quad (44b)$$

As, however, L/H decreases, the discrepancies become insignificant converging to zero for $L/H \to 0$ [Fig. 7(*a*)].

The important difference between the two theories lies in their mode shapes. As shown in Fig. 7(*b*), the inhomogeneous theory (Eq. 41) leads to a sharp

deamplification of modal displacements with depth, not anticipated by the homogeneous theory (Eq. 16). This discrepancy is not decreasing with L/H, although its consequence on the shear-strain/axial-strain ratio is, indeed, diminishing as the dam becomes narrower.

Reinterpretation of Kisenyama Dam Records.—The new theory appears to be able to explain the sharp increase of motion near the crest of the Kisenyama rockfill dam during the September 9, 1969 earthquake.

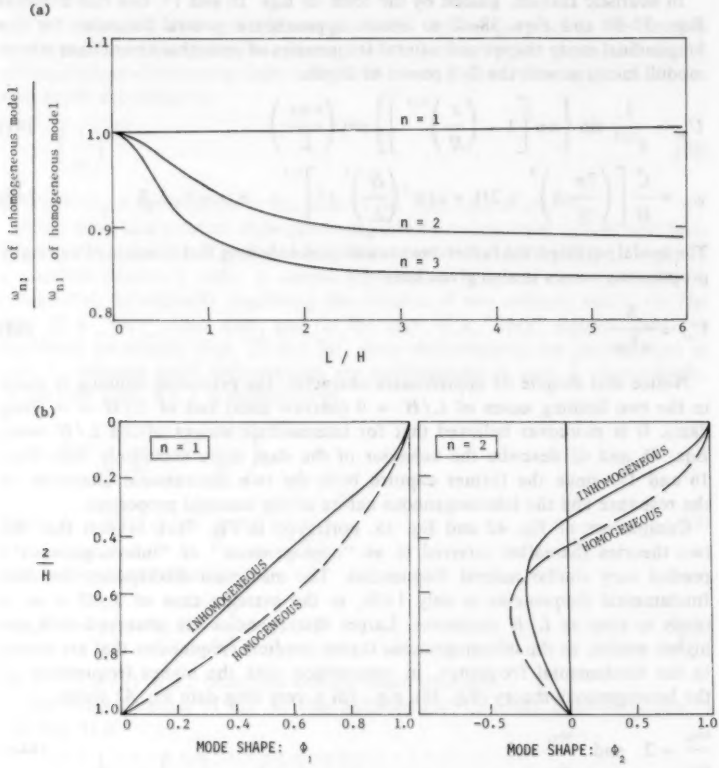

FIG. 7.—Comparison of: (*a*) Three Natural Frequencies; and (*b*) Vertical Components of Two Mode Shapes Obtained with Homogeneous (Eqs. 16, 17) and Inhomogeneous Models (Eqs. 41, 42)

First, using Eq. 42 instead of Eq. 16, the effective S-wave velocity of the dam during this earthquake is estimated to be

$$\bar{C} \simeq \frac{2\pi(82)}{(0.42)}\left[(2.443)^2 + 2(1.25)\pi^2\left(\frac{82}{168}\right)^2\right]^{-1/2} \simeq 356\,\frac{\text{m}}{\text{s}} \quad \ldots\ldots\ldots \quad (45)$$

i.e., smaller by only about 0.84% than the value 359 m/s derived previously from Eq. 16.

The natural periods of the two higher symmetric modes are now expected to be [Fig. 6(*a*)]

$$T_{21} \simeq \frac{T_{11}}{1.58} \simeq 0.27 \text{ sec} \quad \ldots \quad (46a)$$

$$T_{31} \simeq \frac{T_{11}}{2.24} \simeq 0.19 \text{ sec} \quad \ldots \quad (46b)$$

compared with the values of 0.25 sec and 0.16 sec derived from Fig. 2(*b*).

Finally, the peak accelerations at points 2 and 3 are reestimated on the basis of the same, aforementioned assumptions, i.e., only three modes participate in the motion; the corresponding three spectral accelerations are the same. The results are displayed in Table 2 for all three rules of combining modal maxima. The agreement of the predicted peak acceleration ratios with the observed value of 2.34 clearly demonstrates that inhomogeneity (of the form described by Eqs. 33 or 34) has been the primary factor that caused the high amplification of the motion near the top of the dam. Also shown in this table is the prediction of the peak values and their ratio under the assumption that the spectral acceleration, S_a, of the second and third higher modes is two times larger than the spectral acceleration of the fundamental mode. The result ($AR \simeq 3.57 > 2.34$) further supports the assumption of not very different S_a values for the three modes. Thus, it appears that the homogeneous theory cannot even roughly explain the observed distribution of accelerations along the height of the dam. The superiority of the inhomogeneous theory, in this respect, is clear. Whether or not the theory will always yield results comparing as favorably with reality as in this single case, remains to be seen. The reader is cautioned, nevertheless, that factors other than those accounted for by the theory, such as the nonrectangular geometry of the canyon and the nonlinear soil deformations during strong, earthquake-induced vibrations, may also play a predominant role in certain cases. Their effect should, therefore, at least qualitatively be assessed when studying the longitudinal as well as the lateral vibrational behavior of earth and rockfill dams.

Summary and Conclusions

Longitudinal vibrations of embankment dams are of concern in geotechnical engineering since they can cause transverse cracking at the abutment dam or the dam-outlet works interfaces. Such cracking is quite dangerous as it may allow water to flow through the dam and thus lead to piping failure.

Free and forced longitudinal vibrations of embankment dams in a rectangular canyon have been studied with a method that accounts for both shear and dilatational deformations and models the dam as a linear homogeneous medium. Presented numerical results demonstrate the effect of the length and height of the dam on its natural frequencies and its modal displacement and strain shapes. The method has been successfully evaluated by comparing the predicted natural frequencies for the Santa Felicia Dam with the observed predominant

frequencies of the amplification spectra obtained from recorded motions on this Dam during two earthquakes (1).

Failure of the method to explain the observed sharp increase of the motion near the crest of the Kiseneyama rockfill dam in Japan during a moderate earthquake (9) motivated the study of the importance of soil inhomogeneity. An approximate method has thus been developed that considers the shear modulus in the dam as increasing with the 2/3 power of depth, a variation that has been confirmed from in situ measurement in several dams (1,2,5,6). This simple "inhomogeneous" method is negligibly different from the "homogeneous" theory when natural frequencies are compared. It yields, however, mode shapes that exhibit a sharp attenuation with depth near the crest, and, consequently, it explains very well the observed behavior of the Kisenyama Dam.

In conclusion, it appears that additional theoretical and, even more, experimental research may be needed in order to develop reliable methods of design of embankment dams to resist longitudinal vibrations.

Acknowledgment

The writer acknowledges useful comments by the ASCE reviewers.

Appendix.—References

1. Abdel-Ghaffar, A. M., and Scott, R. F., "An Investigation of the Dynamic Characteristics of an Earth Dam," *Earthquake Engineering Research Laboratory Report EERL 78-02*, California Institute of Technology, Pasadena, Calif., 1978.
2. Abdel-Ghaffar, A. M., Scott, R. F., and Craig, M. J., "Full-Scale Experimental Investigation of a Modern Earth Dam," *Earthquake Engineering Research Laboratory Report EERL 80-02*, California Institute of Technology, Pasadena, Calif., 1978.
3. Ambraseys, N. N., "On the Shear Response of a Two-Dimensional Truncated Wedge Subjected to an Arbitrary Disturbance," *Bulletin of the Seismological Society of America*, Vol. 50, No. 1, 1960, pp. 45–56.
4. Gazetas, G., "Shear Vibrations of Vertically Inhomogeneous Earth Dams," *International Journal for Numerical and Analytical Methods in Geomechanics*, 1981.
5. Gazetas, G., "A New Dynamic Model for Earth Dams Evaluated Through Case Histories," *Soils and Foundations*, Japanese Society of Civil Engineers, 1981.
6. Gazetas, G., and Abdel-Ghaffar, A. M., "Earth Dam Characteristics from Full-Scale Vibrations," to be presented at the June, 1981, International Conference of Soil Mechanics and Foundation Engineering, to be held at Stockholm, Sweden.
7. Hatanaka, M., "Fundamental Considerations on the Earthquake Resistant Properties of the Earth Dam," *Disaster Prevention Research Institute Bulletin No. 41*, Kyoto University, Kyoto, Japan, 1955.
8. Newmark, N. M., and Rosenblueth, E., *Fundamentals of Earthquake Engineering*, Prentice-Hall, Inc., Englewood Cliffs, N.J., 1971.
9. Okamoto, S., *Introduction to Earthquake Engineering*, John Wiley and Sons, Inc., New York, N.Y., 1973.
10. Seed, H. B., and Martin, G. R., "The Seismic Coefficient in Earth Dam Design," *Journal of the Soil Mechanics and Foundations Division*, ASCE, Vol. 92, No. SM3, Proc. Paper 4824, May, 1966, pp. 25–58.
11. Seed, H. B., "Considerations of Earthquake Resistance of Earth and Rockfill Dams," *Geotechnique*, Vol. 29, No. 3, 1979, pp. 15–63.

JOURNAL OF THE GEOTECHNICAL ENGINEERING DIVISION

CYCLIC AXIAL RESPONSE OF SINGLE PILE

By Harry G. Poulos,[1] M. ASCE

INTRODUCTION

The majority of early data on the response of piles to cyclic axial loading was from tests on piles subjected to "one-way" cyclic loading (that is, cycling between zero minimum load and a specified maximum load), and these tests indicated that there was no significant effect on pile capacity as a result of the previous cyclic loading (5).

However, Holmquist and Matlock (6) described a series of model tests on piles in remolded clay which indicated that considerable loss of skin friction could occur if a pile was subjected to "two-way" cyclic loading (loading alternating between tension and compression with a zero or small mean value), if the load magnitude approached the static pile capacity. Their tests also confirmed the previous finding that "one-way" cyclic loading caused relatively little deterioration of axial performance. Other data summarized by Bea, et al. (3) indicated a trend toward decreasing load capacity and stiffness with increasing number of cycles and cyclic load level.

Because of the possibility of "two-way" cyclic loading on pile foundations supporting offshore structures, it is essential to develop a means for predicting the circumstances under which cyclic loading will affect pile performance. Sangrey (17) has suggested a method of application of critical state concepts to calculate the ultimate axial capacity of cyclically-loaded piles, but this approach does not consider deformations. Matlock and Foo (12) have described an analysis in which a pile in a relatively simple hysteretic and degrading soil model is considered; soil degradation is assumed to occur if a full reversal of yielding in both directions occurs. Boulen, et al. (4) have described a finite element analysis in which a hyperbolic relationship between strain and number of cycles is employed to analyze a pile in sand. Poulos (13) has outlined an effective

[1]Reader in Civ. Engrg., Univ. of Sydney, Sydney 2006, New South Wales, Australia.

Note.—Discussion open until June 1, 1981. To extend the closing date one month, a written request must be filed with the Manager of Technical and Professional Publications, ASCE. Manuscript was submitted for review for possible publication on March 25, 1980. This paper is part of the Journal of the Geotechnical Engineering Division, Proceedings of the American Society of Civil Engineers, © ASCE, Vol. 107, No. GT1, January, 1981. ISSN 0093-6405/81/0001-0041/$01.00.

stress approach based on elastic theory, in which cyclic loading is assumed to develop excess pore pressures in the soil adjacent to the pile with a consequent reduction in soil modulus and skin resistance. However, some of the assumptions upon which the effective stress analysis was based are of limited generality, and the results presented may not be applicable to a wide range of problems. Moreover, recent tests by Grosch and Reese (6) suggest that cyclic degradation of skin friction arises primarily from destruction of interparticle bonds, and particle realinement, rather than the development of pore pressures.

A further evolution of the previous analysis (13) is described herein, allowing for the consideration of cyclic degradation of the soil in terms of total stress. The major objectives are to answer two questions:

1. Will prior cyclic loading of a pile affect its ultimate axial capacity?
2. How does the axial stiffness of the pile change as the number of cycles of load increases?

A brief outline of the analysis for static loading is given and various methods of allowing for cyclic degradation of the soil are described. A series of solutions for a typical offshore pile is then presented and the effects on cyclic axial

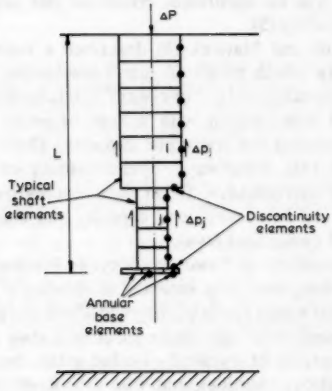

FIG. 1.—Discretization of Pile (Note: Interaction Stresses Shown on Only a Few Elements; Each Dot Represents Element Collocation Point)

response of various pile and soil parameters are examined. Finally, the theory is compared with the results of some small-scale laboratory model tests.

Analysis of Pile Subjected to Static Loading

The static loading analysis has been described by Poulos (3) and will be only briefly reviewed here. It is a simplified form of boundary element analysis in which the pile is discretized into a series of elements and the soil is considered to be a linearly elastic continuum. To allow for piles of nonuniform section, three types of elements can be used: cylindrical shaft elements, annular base

elements, and annular elements at discontinuities in shaft diameter (see Fig. 1). By considerations of equilibrium and compatibility between the vertical movements of pile and soil at each element, relationships may be derived between the pile-soil interaction stresses, the pile vertical displacement, and the increment of axial load. These relationships may be solved for the interaction stress increments and the incremental pile deflections, from which the over-all values can be obtained by addition to the existing values.

Allowance for pile-soil slip or yield of an element may be made by specifying an upper limit to the value of the interaction stress at each element, and carrying out an iterative analysis. This allows a static load-settlement curve to failure to be computed, and also allows for unloading of a pile to be analyzed. If pile-soil slip has occurred, unloading to zero load will result in residual stresses being developed in the pile (in addition to those which may be present due to installation of the pile).

An important feature of the foregoing analysis is that it can take into account, approximately, nonhomogeneity of the soil along and beneath the pile shaft, as described in Ref. 14. The ability to consider soil nonhomogeneity in a convenient and economical manner is essential when considering a cyclically loaded pile, as "degradation" of soil properties will occur at different rates along the pile, depending on the local stress level. Even in an initially homogeneous soil, a nonuniform distribution of soil modulus and skin friction will result from cyclic loading because of the nonuniformity of stress distribution along the pile.

Extension of Analysis to Cyclic Loading

The foregoing static analysis can be extended to cyclic loading in two ways:

1. By carrying out an incremental analysis in which the entire cyclic load history of the pile is applied, with the soil parameters being progressively adjusted at each increment to reflect the effects of the cyclic loading.
2. By carrying out an analysis to ascertain the response of a pile after a number of cycles N of uniform magnitude (maximum P_{max}, minimum P_{min}) have been applied to the pile, with the soil parameters being adjusted to reflect the effects of cyclic loading at the end of the load sequence.

The first approach, although more satisfactory, would involve enormous computational effort if the load sequence involved a large number of cycles; consequently, the second approach has been adopted.

The detailed analysis procedure is as follows:

1. First estimates of soil modulus E_s, ultimate skin friction τ_u, and ultimate base resistance p_{bu} are chosen for each element (e.g., the values for static loading).
2. The pile is analyzed for the maximum load P_{max}, and the distribution of shear stress and displacement along the pile determined.
3. The pile is similarly analyzed for the minimum load P_{min}.
4. The cyclic shear stress τ_c and cyclic displacement ρ_c are determined from the two foregoing analyses by subtracting the minimum values from the maximum values.

5. For the specified number of cycles and the appropriate level of cyclic shear stress, the following determinations are made: Cyclic displacement or cyclic shear strain at each element (depending on the type of degradation analysis being performed); the change in soil modulus; and ultimate skin friction (and ultimate base resistance for base elements).

6. The new modulus and ultimate skin friction values are compared with the estimated values, and if the difference is greater than a specified tolerance, new values are selected and steps 2 to 6 repeated until the desired degree of convergence is attained.

7. The cyclic deflection, the mean deflection, and the values of ultimate skin friction and base resistance are thus obtained, from which the available ultimate load capacity after cycling may be readily calculated.

Degradation Factors

To simplify the computations and give a better insight into the progress of cyclic degradation, the concept of degradation factors has been introduced (13), a degradation factor being the ratio of the value of a parameter after cyclic loading to the corresponding value for static loading. Three types of degradation factor are relevant here:

1. Ultimate skin friction degradation factor D_τ, that is

$$D_\tau = \frac{\tau_{ac}}{\tau_{as}} \quad (1)$$

in which τ_{ac} = ultimate skin friction on a pile element after it has been subjected to cyclic loading; and τ_{as} = ultimate skin friction for static loading.

2. Ultimate base resistance degradation factor D_b, that is

$$D_b = \frac{p_{buc}}{p_{bus}} \quad (2)$$

in which p_{buc} = ultimate base resistance after cyclic loading; and p_{bus} = ultimate base resistance for static loading.

3. Modulus degradation factor D_E, that is

$$D_E = \frac{E_c}{E_s} \quad (3)$$

in which E_c = soil modulus at an element after cyclic loading; and E_s = soil modulus at element, for static loading. Normally, the degradation factors will be less than or equal to 1.0, although values larger than unity may apply in some cohesionless soils, or if the effects of rapid rates of loading are taken into account.

The major problem in analyzing the cyclic response of a pile is to determine how these degradation factors vary with increasing stress or strain level and number of cycles. Some possible approaches are described subsequently.

Methods of Estimating Degradation Factors

The ideal data to have available would be the variation of the three degradation factors D_τ, D_b, and D_E with cyclic interface shear stress level, number of cycles, and cycle frequency. Unfortunately, no such data are currently available and it is therefore necessary to resort to approximate means of estimating the degradation factors. Two broad approaches could be adopted:

1. A total stress approach, in which cyclic loading is assumed to occur under undrained conditions, and no attempt is made to distinguish between the various factors contributing to cyclic degradation. This approach is straightforward, but has the limitation that no account can be taken of time effects, as conditions are assumed to remain undrained.
2. An effective stress approach, in which the effects of cyclic loading are accounted for only by the excess pore pressure generated by cyclic loading (13). By determining the effect of a change in excess pore pressure (and hence effective stress) on τ_a, p_{bu}, and E_s, the corresponding degradation factors may be obtained. Such an approach has the advantage that time effects resulting from pore pressure dissipation during cycling may be incorporated. However, no allowance is made for other factors contributing to cyclic degradation, e.g., structural breakdown of the soil particles, creep of the soil skeleton, and as previously mentioned, such factors may be the predominant cause of the degradation.

A total stress approach will be used herein, and it will be assumed that cyclic degradation is dependent on the cyclic strain level, and not on the permanent strain level. Data to support the validity of this assumption have been presented by Andersen (1).

Degradation of Ultimate Skin Friction and Base Resistance.—Because of the lack of direct data on the degradation of ultimate skin friction τ_a or base resistance p_{bu}, an indirect means of estimation is necessary. Use has been made of the observations of Thiers and Seed (18) and Lee and Focht (11), that the reduction in undrained shear strength s_u is a function of the cyclic shear strain γ_c prior to failure, normalized with respect to the static shear strain to failure, γ_s. Since it is reasonable to assume that τ_a and p_{bu} both depend on s_u, it should also be possible to relate the degradation of τ_a and p_{bu} to γ_c/γ_s. However, it is well known that full mobilization of skin friction occurs at strains or displacements which are only about 10% to 25% of those associated with either the failure of the pile base or of a triaxial sample. It therefore seems appropriate to reference the cyclic shear strain along the pile to a critical shear strain for interface skin friction γ_{ss}, and γ_{ss} would be expected to be on the order of 0.1 to 0.25 times γ_s. To estimate the cyclic shear strain γ_c in the soil adjacent to the pile, use may be made of the analysis developed by Randolph and Wroth (15), from which may be derived, for a pile in a deep elastic soil layer

$$\gamma_c = \frac{2\rho_c}{\zeta d} \quad \text{(4)}$$

in which ρ_c = cyclic displacement of pile at a point on the pile shaft; d =

pile diameter; ν_s = Poisson's ratio of soil; L = embedded pile length; $\zeta = \ln [5\psi(1 - \nu_s) L/d]$; and ψ = 1.0 if the soil is homogeneous and infinitely deep, or 0.5 if the soil has a modulus which increases linearly with depth from zero at the surface. Eq. 4 will be only approximate if the soil ceases to be elastic or pile-soil slip occurs, and in the latter case, may tend to overestimate the cyclic shear strain of the soil. For the pile base, a similar approximate

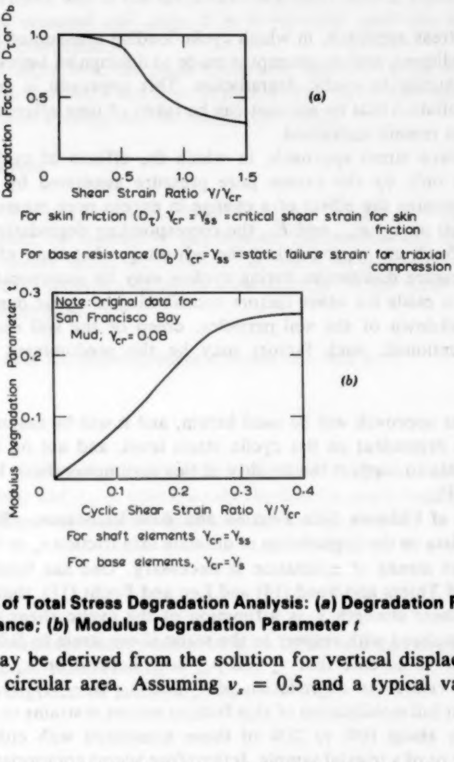

FIG. 2.—Basis of Total Stress Degradation Analysis: (a) Degradation Factors Adopted for Pile Resistance; (b) Modulus Degradation Parameter t

expression may be derived from the solution for vertical displacement beneath a subsurface circular area. Assuming ν_s = 0.5 and a typical value of L/d of about 100

$$\gamma_c \simeq \frac{0.4\,\rho_{bc}}{d_b} \quad \ldots\ldots\ldots\ldots\ldots\ldots\ldots\ldots (5)$$

in which ρ_{bc} = cyclic displacement of pile base; and d_b = diameter of pile base.

The degradation curves for τ_a and p_{bu} used for the solutions described herein are shown in Fig. 2(*a*), and have been derived from the data of Lee and Focht (11).

Degradation of Soil Modulus E_s.—At least two approaches to obtaining soil modulus degradation factors can be contemplated: (1) By making use of plots of cyclic shear strain contours against cyclic stress level and number of cycles, such as those presented by Andersen (1) for Drammen Clay; and (2) by using

the expression derived by Idriss, et al. (8), which gives the modulus degradation factor D_E as

$$D_E = N^{-t} \quad (6)$$

in which N = number of cycles; and t = degradation parameter depending on cycling axial strain. Because of the simplicity of the second approach, it has been used herein. Fig. 2(*b*) shows a plot of the degradation parameter t versus cyclic strain ratio, derived from the data presented by Idriss, et al. (8) for San Francisco Bay Mud. It is assumed that the reference strain γ_{cr} is equal to the static shear strain at failure, γ_s. In addition, because the soil modulus is influenced by a relatively larger volume of soil than is the pile-soil skin friction, only a fraction w of the cyclic strain at the interface should be used in evaluating the modulus degradation factor. From an examination of results of finite element analyses of a pile in a radially nonhomogeneous soil obtained by Balaam, et al. (2), a value of w between 0.5 and 0.25 appears to be applicable. For the solutions herein, w has been taken to be 0.4.

Effect of Rate of Loading.—The undrained behavior of soils is influenced by the rate of load application, and Sangrey (17) suggests that the undrained strength varies approximately linearly with the logarithm of time to failure. It seems reasonable to assume that the soil modulus, ultimate skin friction, and ultimate base resistance vary with loading rate in a similar fashion to undrained strength. Consequently, to allow for loading rate effects, the degradation factors D_τ, D_b, and D_E can be multiplied by a rate factor D_R, as

$$D_R = 1 - F_\rho \cdot \log_{10}\left(\frac{\lambda_r}{\lambda}\right) \quad (7)$$

in which λ_r = reference loading rate (e.g., for static load test); λ = actual loading rate; and F_ρ = rate factor, which the limited available data suggest is on the order of 0.1 (range 0.05 to 0.3).

Solutions for Typical Offshore Pile

To investigate the influence of various parameters on cyclic pile response, a typical offshore pile in clay has been analyzed, as shown in Fig. 3. The soil parameters shown therein are considered to be representative of a normally-consolidated clay deposit. In Fig. 3, degradation of ultimate skin friction as shown in Fig. 2(*a*) γ_{ss} = 0.02; degradation of ultimate base resistance as shown in Fig. 2(*a*) γ_s = 0.08; and soil modulus degradation as shown in Fig. 2(*b*) γ_{cr} = 0.08. The effects of variations in some of the pile and soil parameters will be examined subsequently. Attention is concentrated on the following quantities: (1) The ultimate load capacity after cycling, P_{uc}; and (2) the cyclic "stiffness" (cyclic load divided by cyclic deflection) of the pile after N cycles, K_c.

To give the results greater generality, P_{uc} will be normalized with respect to P_{us}, the ultimate static load capacity of the pile, and K_c will be normalized with respect to K_{c1}, the cyclic stiffness of the pile for the first cycle of loading. The two other important parameters to be considered are the magnitude of the cyclic load P_c (normalized as P_c/P_{us}), and the number of cycles N. In all cases it will be assumed that the N load cycles will be of uniform half-amplitude

P_c (i.e., $+P_c$ to $-P_c$ range). Fig. 4 summarizes the definitions of the foregoing cyclic response variables. In particular, the following four relationships will be considered: P_{uc}/P_{us} versus P_c/P_{us}; K_c/K_{c1} versus P_c/P_{us}; P_{uc}/P_{us} versus N; and K_c/K_{c1} versus N.

All solutions have been obtained from a computer program CYCPL6, using 10 shaft elements and one base element to divide the pile. For simplicity, the ultimate skin friction and base resistance in compression and tension are assumed to be equal although in reality this would not be the case, particularly for the base resistance. Also, the ambient static load P_o is taken as zero, i.e., the cyclic load has a zero mean value.

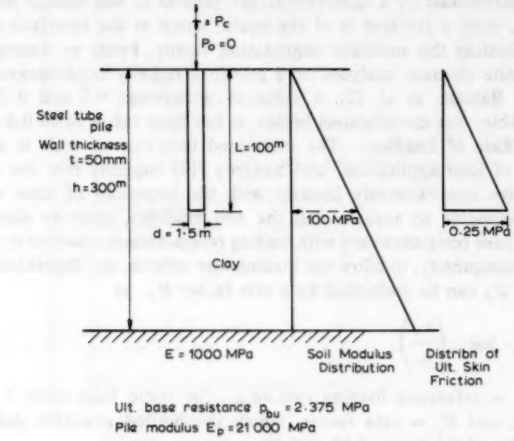

FIG. 3.—Typical Offshore Pile Analyzed: Standard Parameters

Effect of Cyclic Load Level and Number of Cycles.—The dimensionless ultimate load and cyclic stiffness are plotted in Fig. 5 as functions of the number of cycles N, for various dimensionless cyclic load levels P_c/P_{us}. Relatively little reduction in ultimate load capacity occurs for cyclic load levels less than ±50% of the ultimate static value, and data quoted by Bea, et al. (3) support this conclusion. There is relatively little effect on cyclic stiffness, although as noted also by Boulon, et al. (4), the stiffness decreases continuously with increasing numbers of cycles, even at relatively low cyclic load levels. However, for $P_c/P_{us} = \pm 0.6$, failure during cycling ($P_{uc} = P_c$) occurs after about 5000 cycles.

This sudden drop in ultimate load capacity with increasing cyclic load level is further illustrated in Fig. 6, in which P_{uc}/P_{us} and K_c/K_{c1} are plotted against P_c/P_{us} for various values of N. It is clearly seen that cyclic load levels in excess of about 55% of P_{us} are likely to cause failure during cycling.

For $N = 1000$ cycles, Fig. 7 plots distributions of the degradation factors, cyclic load, cyclic displacement, and cyclic shear stress along the pile, for three values of P_c/P_{us}. As the cyclic load level increases, the degradation of both τ_s and E_s becomes more marked, particularly near the top of the pile. Consequently, more load is then carried in the lower part of the pile. These characteristics

are also observed by Boulon, et al. (4) in their finite element analysis. Fig. 7 clearly shows the progress of "unzipping" of the pile (i.e., the loss of ultimate skin friction) due to increasing the intensity of cyclic loading. Similar characteris-

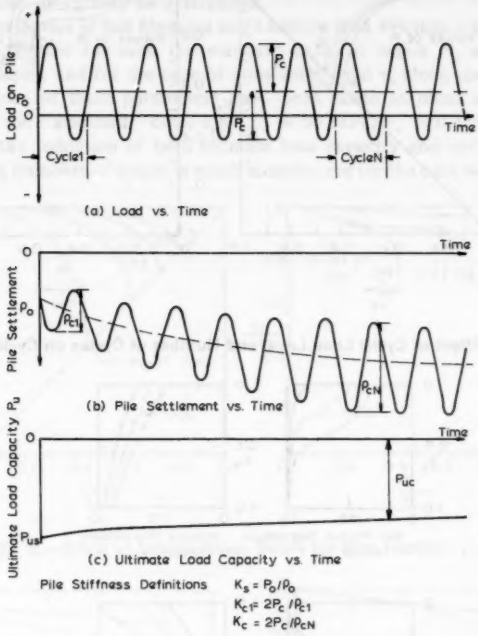

FIG. 4.—Definition of Key Cyclic Response Variables

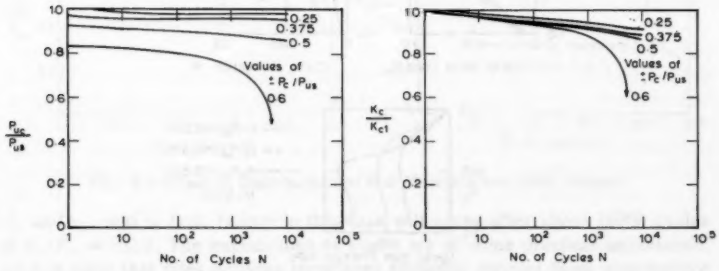

FIG. 5.—Effect of Cyclic Load Level and Number of Cycles on Cyclic Response

tics are found if the degradation factors and shear stress distribution are plotted for increasing numbers of cycles at a constant cyclic load level.

Effect of Critical Cyclic Strain for Skin Friction, γ_{ss}.—Fig. 8 shows the effect

of the critical cyclic shear strain γ_{ss} for skin friction on the ultimate pile capacity and cyclic stiffness after 1,000 cycles. In all cases, the critical strain for ultimate

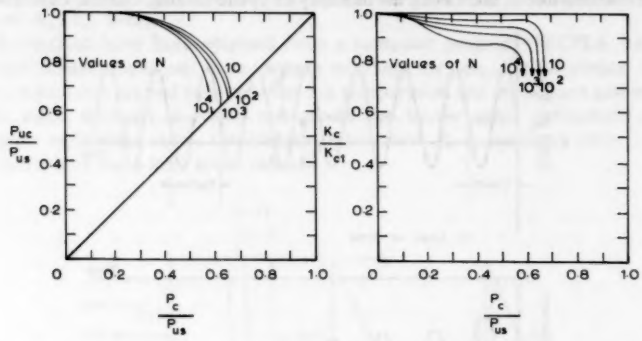

FIG. 6.—Effect of Cyclic Load Level and Number of Cycles on Cyclic Response

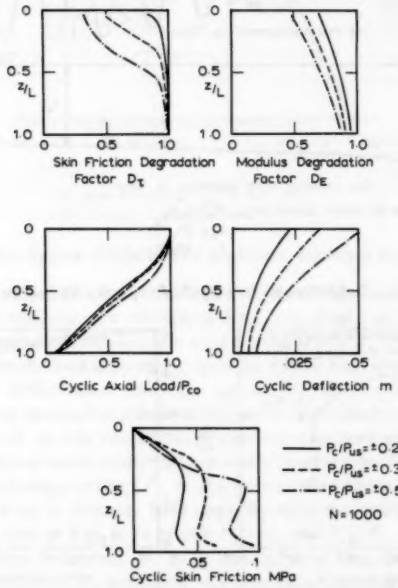

FIG. 7.—Influence of Cyclic Load Level on Pile Behavior

base resistance and soil modulus γ_s has been kept constant at a typical value of 0.08. A decrease in γ_{ss} results in a significant decrease in both ultimate load capacity and cyclic stiffness, with failure during cycling occurring at smaller

cyclic load levels. The sensitivity of the results to γ_{ss} indicates that it would be worth while performing model and field tests to obtain further data on values of cyclic displacement necessary to cause significant degradation of skin friction, whence the value of γ_{ss} may be determined.

Effect of Distribution of Soil Modulus and Ultimate Skin Friction.—Calculations have been performed for both the standard case, in which E_s and τ_a vary linearly with depth, and for the case of constant E_s and τ_a along the pile shaft. The static values of these parameters have been taken as those at middepth of the pile in the "standard" case, i.e., $E_s = 50$ MPa, $\tau_a = 0.125$ MPa. Fig. 9 shows that the reduction of both ultimate load capacity and cyclic stiffness with increasing numbers of cycles is much more severe for the case with constant

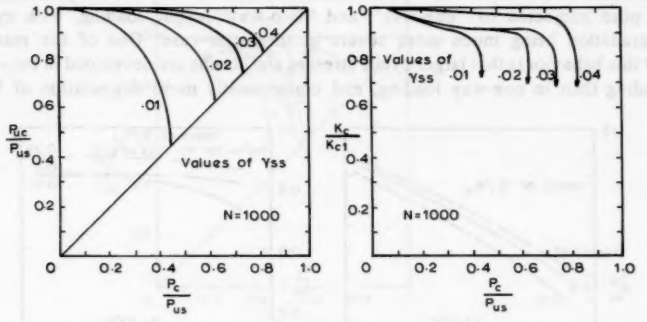

FIG. 8.—Effect of Critical Shear Strain for Skin Friction, γ_{ss}

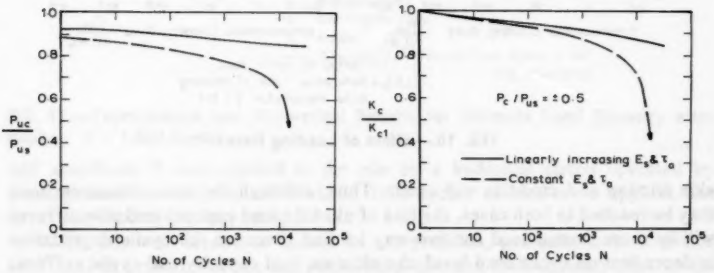

FIG. 9.—Effect of Distribution of Soil Modulus and Skin Friction

E_s and τ_a, and in fact, failure in this case will occur after about 16000 cycles if $P_c/P_{us} = \pm 0.5$. The implications of Fig. 9 are of some practical importance, as it is clear that piles deriving significant frictional support from near-surface soil layers under static loading conditions may lose a significant amount of this support due to the severe cyclic degradation which occurs near the top of the pile. Piles in overconsolidated clays may fall into this category.

Effect of Loading Rate.—The preceding solutions assume no effects of the loading rate on ultimate skin friction or soil modulus. An indication of the

influence of rate effects is given in Fig. 10, in which these quantities, in dimensionless form, are plotted against a dimensionless loading rate factor, $P_{us}/T\lambda_r$, in which T = cyclic loading period, and λ_r = reference rate of loading for which the values of static soil modulus and skin friction are determined. As would be expected, an increase in the rate of cyclic load application (and hence in $P_{us}/T\lambda_r$) significantly increases the ultimate pile capacity, although it does not have much effect on the cyclic stiffness ratio K_{cN}/K_{c1}. The beneficial effect of increased loading rate becomes more pronounced as P_c/P_{us} increases. The increase in pile capacity with increasing load rate is consistent with data quoted by Bea, et al. (4).

One-Way and Two-Way Cyclic Loading.—As previously mentioned, Holmquist and Matlock (7) have found considerable differences between the performance of piles subjected to "one-way" and "two-way" cyclic loading, with cyclic degradation being much more severe in the latter case. One of the reasons for this behavior is that larger cyclic stresses and strains are developed in two-way loading than in one-way loading, and consequently more degradation of both

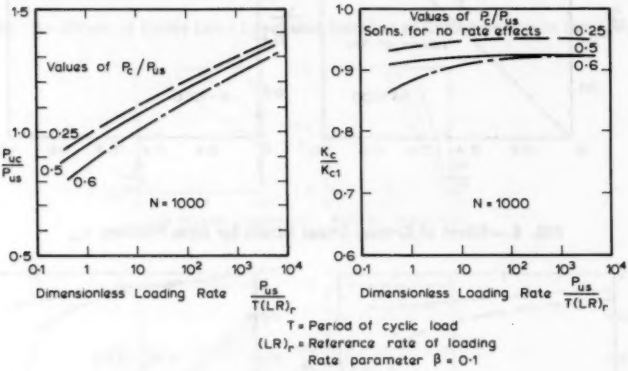

FIG. 10.—Effect of Loading Rate

skin friction and modulus will occur. Thus, although the same maximum load may be reached in both cases, the loss of ultimate load capacity and pile stiffness will be more pronounced for two-way loading. Because the cyclic degradation is dependent on cyclic load level, the ultimate load capacity and cyclic stiffness for one-way loading for a maximum load P_{max} will in fact be the same as those for two-way loading with a maximum load of 0.5 P_{max}.

Model Piles Tests

A series of small-scale model pile tests was carried out in four different soils: Sydney Kaolin (LL = 47, PL = 18); Hurstville Clay (LL = 65, PL = 20); Redfern Clay (LL = 42, PL = 22); and Darlington Clay (LL = 55, PL = 33). In each case, the soil was remolded and placed in a cylindrical container 152 mm (6 in.) diam and 230 mm (9 in.) deep. The piles were of

solid aluminum 20 mm (0.78 in.) diam and 250 mm (10 in.) long, and were jacked through the clay so that the end of the pile protruded from the bottom of the soil. Consequently, only the skin friction characteristics were measured. After allowing a suitable rest period (typically two to three hours), the following test procedure was carried out:

1. The pile was loaded to failure in compression over a period of about 2 min in order to obtain the static ultimate load capacity P_{us} (failure being defined as a deflection of about 2.5% of the diameter).
2. After unloading and leaving the pile to rest for 1 hr, a cyclic load of

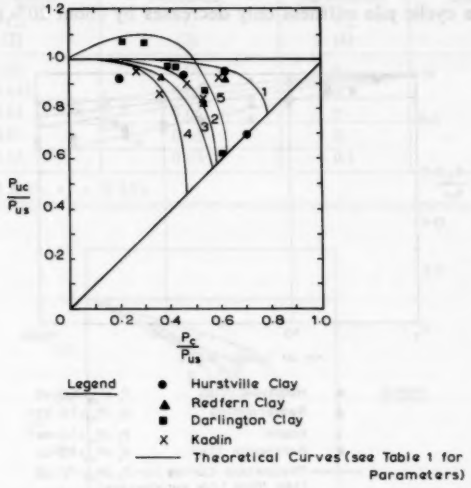

FIG. 11.—Experimental and Theoretical Results for Ultimate Load Capacity after Cycling; $N = 1{,}000$ Cycles

half amplitude P_c was applied to the pile by a hydraulic piston operated by a compressed air-actuated relay valve; 1000 cycles of load were applied, the average period of loading being 2.5 sec.

3. The pile was loaded to failure in compression, generally over a period of 2 min, in order to obtain the postcycling ultimate load capacity P_{uc}. In the case of the pile in Darlington Clay, the time to failure was typically about 20 sec.

4. Steps 2 and 3 were repeated a number of times for different values of the cyclic load P_c.

Because of the nature of the apparatus, the mean load about which cycling occurred was about 37 N (8.34 lb) (approximately 10% of the ultimate static load). The load was measured using a strain-gaged proving ring, and the axial deflection of the pile head by a displacement transducer. Load versus time and deflection versus time relationships were plotted directly on a chart recorder,

while load-deflection curves were plotted on an X-Y recorder.

Fig. 11 summarizes the experimental data on ultimate load capacity after cycling, and plots P_{uc}/P_{us} versus P_c/P_{us} for $N = 1000$ cycles. The experimental results for the four soils are reasonably consistent and indicate little reduction in ultimate load capacity unless the half amplitude of cyclic load P_c exceeds about 60%–70% of the ultimate static load capacity P_{us}. The results for Darlington Clay, indicating values of P_{uc}/P_{us} greater than unity, may reflect the influence of the higher loading rate used in these tests.

Fig. 12 shows experimental results for the variation of cyclic stiffness with number of cycles, for a cyclic load level of approximately $\pm 0.45\ P_{us}$. Again, there is reasonable consistency among the results from the various soils, and in general, the cyclic pile stiffness only decreases by about 20% ($\pm 10\%$) after 1,000 cycles.

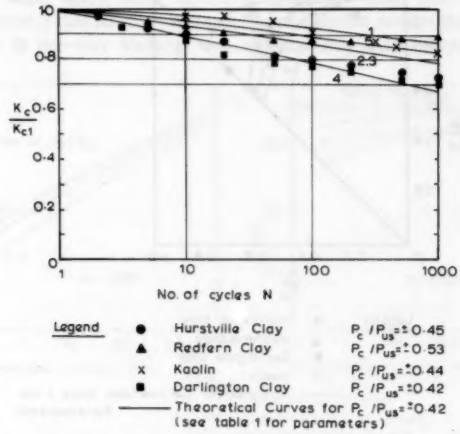

FIG. 12.—Experimental and Theoretical Results for Cyclic Stiffness Versus Number of Cycles

The influence of cyclic load level on cyclic pile stiffness is plotted in Fig. 13 for $N = 1{,}000$. As would be expected, the decrease in cyclic stiffness (as expressed by the ratio K_c/K_c') becomes more pronounced as the cyclic load level P_c/P_{us} increases.

Because of the difficulty of assigning accurate values to the various parameters required in the analysis, theoretical solutions have been obtained for a range of parameters. The soil modulus E_s and the static ultimate skin friction τ_a are assumed constant with depth, the values being chosen to give reasonable correspondence with the static performance in most of the tests. The parameters used are shown in Table 1. The degradation of skin friction and soil modulus has been determined from Fig. 2.

The theoretical solutions thus obtained are shown in Figs. 11 through 13 and show similar trends to the experimental data. Curve 5, which includes allowance for loading rate effects, is relevant only to the tests on Darlington

Clay. The following points are worthy of note:

1. The theory predicts a very sudden drop in ultimate load capacity P_{uc} after a certain critical ratio of P_c/P_{us} is reached; this behavior is substantiated by the model test results.

TABLE 1.—Parameters Used in Theoretical Solutions for Model Pile Tests

Curve (1)	Critical cyclic strain for skin friction, γ_{ss} (2)	Critical cyclic strain for modulus, γ_s (3)	Loading rate parameter, F_p (4)	Proportion of interface stress used for E_s, w (5)
1	0.02	0.08	0	0.4
2	0.012	0.05	0	0.4
3	0.01	0.05	0	0.4
4	0.01	0.05	0	0.6
5	0.01	0.05	0.1	0.4

Note: $E_s = 9$ MPa; $\tau_a = 30$ kPa.

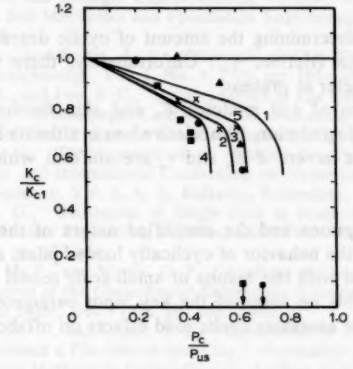

FIG. 13.—Effect of Cyclic Load Level on Cyclic Pile Stiffness; $N = 1{,}000$ Cycles

2. The value of γ_{ss} (the critical shear strain for strain friction) to obtain agreement with the experimental results is quite small, on the order of 0.01.

Despite the uncertainties still existing in the values of the input parameters, there are indications that the cyclic response predicted by the theory is in broad

agreement with that measured in the model tests. It is interesting to note that the present total stress solutions are in better agreement with the test results than are the effective stress solutions presented previously by the writer (13) when considering the results of the tests in Darlington Clay.

Conclusions

The analysis presented herein is an extension of an elastic-based analysis of a statically loaded pile which uses a total stress approach to incorporate the effects of cyclic loading, and which involves an iterative analysis to determine the ultimate load capacity and the cyclic stiffness of the pile after a given number of load cycles of a given magnitude.

Some solutions have been obtained for a typical offshore pile, and from these the following observations have been made:

1. The ultimate load capacity and cyclic stiffness decrease with increasing number of cycles N and increasing cyclic load level. The effect of N becomes more significant when the cyclic load P_c (half peak to peak) approaches 50% of the static ultimate load P_{us}.
2. Cyclic degradation begins at the top of the pile and progresses downward as P_c or N increases, resulting in gradual transfer of load to lower parts of the pile.
3. The crucial factor in determining the amount of cyclic degradation is the critical shear strain for skin friction, γ_{ss}. Unfortunately, there is little data available on this key parameter at present.
4. The static distributions of soil modulus E_s and skin friction τ_a have a marked effect on the cyclic degradation. The relative loss in ultimate load capacity and cyclic stiffness is more severe if E_s and τ_a are uniform with depth than if they increase with depth.

Despite the many assumptions and the simplified nature of the analysis, it does give some insight into the behavior of cyclically loaded piles, and indicates behavior which is consistent with the results of small-scale model tests. When further data become available on some of the key input parameters required, they may provide a basis for assessing cyclic load effects on offshore piles.

Acknowledgments

The work described herein forms part of a research project on deformation of foundations being carried out at the University of Sydney under the general direction of E. H. Davis. This work is supported by the Australian Research Grants Committee. The writer gratefully acknowledges the assistance of K. L. Larymore and G. S. Young in carrying out the model tests.

Appendix I.—References

1. Andersen, K., "Behaviour of Clay Subjected to Undrained Cyclic Loading," *Proceedings of Conference on Behaviour of Offshore Structures (BOSS)*, Trondheim, Norway, Vol. 1, 1976, pp. 392–403.

2. Balaam, N. P., Poulos, H. G., and Booker, J. R., "Finite Element Analysis of the Effects of Installation on Pile Load-Settlement Behaviour," *Geotechnical Engineering*, Vol. 6, No. 1, 1975, pp. 33–48.
3. Bea, R. G., Audibert, J. M. E., and Dover, A. R., "Dynamic Response of Laterally and Axially Loaded Piles," *Paper OTC 3749, Proceedings*, 12th Offshore Technology Conference, Houston, Tex., 1980, pp. 129–139.
4. Boulon, M., Desrves, J., Foray, P., and Forgue, M., "Numerical Model for Foundation Under Cyclic Loading, Application to Piles," International Symposium on Soils Under Cyclic and Transient Loading, Swansea, Wales, A. A. Balkema, Rotterdam, 1980, pp. 681–694.
5. Broms, B. B., "Bearing Capacity of Cyclically Loaded Piles," *Report No. 44*, Swedish Geotechnical Institute Stockholm, Sweden, 1972, pp. 1–16.
6. Grosch, J. J. and Reese, L. C., "Field Tests of Small-Scale Pile Segments in a Soft Clay Deposit under Repeated Axial Loading," *Paper OTC 3869, Proceedings*, 12th Official Technical Conference, Houston, Tex., 1980, pp. 143–151.
7. Holmquist, D. V., and Matlock, H., "Resistance-Displacement Relationships for Axially-Loaded Piles in Soft Clay," *Proceedings*, 8th Offshore Technical Conference, Houston, Tex., Paper OTC2474, 1976, pp. 554–569.
8. Idriss, I. M., Dobry, R., and Singh, R. D., "Nonlinear Behavior of Soft Clays During Cyclic Loading," *Journal of the Geotechnical Engineering Division*, ASCE, Vol. 104, No. GT12, Proc. Paper 14265, Dec., 1978, pp. 1427–1447.
9. Ladd, C. C., and Foott, R., "New Design Procedure for Stability of Soft Clays," *Journal of the Geotechnical Engineering Division*, ASCE, Vol. 100, No. GT7, Proc. Paper 10664, July, 1974, pp. 763–786.
10. Ladd, C. C., Foott, R., Ishihara, K., Schlosser, F., and Poulos, H. G., "Stress-Deformation and Strength Characteristics," S.O.A. Report, 9th International Conference on Soil Mechanics and Foundation Engineering, Tokyo, Japan, Vol. 2, 1977, pp. 421–494.
11. Lee, K. L., and Focht, J. A., "Strength of Clay Subjected to Cyclic Loading," *Marine Geotechnology*, Vol. 1, No. 3, 1976, pp. 165–185.
12. Matlock, H., and Foo, S. C., "Axial Analysis of Pile Using a Hysteretic and Degrading Soil Model," *Proceedings*, Conference on Numerical Methods in Offshore Piling, Institution of Civil Engineers, London, England, 1979, pp. 99–106.
13. Poulos, H. G., "Development of an Analysis for Cyclic Axial Loading of Piles," *Proceedings*, 3rd International Conference on Numerical Methods in Geomechanics, Aachen, Germany, Vol. 4, A. A. Balkema, Rotterdam, 1979.
14. Poulos, H. G., "Settlement of Single Piles in Nonhomogeneous Soils," *Journal of the Geotechanical Engineering Division*, ASCE, Vol. 105, No. GT5, Proc. Paper 14575, May, 1979, pp. 627–641.
15. Randolph, M. P., and Wroth, C. P., "Analysis of Deformation of Vertically Loaded Piles," *Journal of the Geotechnical Engineering Division*, ASCE, Vol. 104, No. GT12, Proc. Paper 14262, Dec., 1978, pp. 1465–1488.
16. Randolph, M. P., and Carter, J. P., "The Effect of Pile Permeability on the Stress Changes Around a Pile Driven into Clay," *Proceedings*, 3rd International Conference on Numerical Methods in Geomechanics, Aachen, Germany, Vol. 3, A. A. Balkema, Rotterdam, 1979, pp. 1097–1105.
17. Sangrey, D. A., "Response of Offshore Piles to Cyclic Loading," *Paper OTC2944, Proceedings*, 9th Official Technical Conference, Houston, Tex., 1977, pp. 507–512.
18. Thiers, G. R., and Seed, H. B., "Strength and Stress-Strain Characteristics of Clay Subjected to Seismic Loading Conditions," *Vibration Effects of Earthquakes on Soils and Foundations*, American Society for Testing and Materials, STP450, 1969, p. 3056.
19. Van Eekelen, H. A. M., and Potts, D. M., "The Behaviour of Drammen Clay Under Cyclic Loading," *Geotechnique*, London, England, Vol. 28, No. 2, 1978, pp. 173–196.

APPENDIX II.—NOTATION

The following symbols are used in this paper:

D_b = degradation factor for ultimate base resistance;

D_E = degradation factor for soil modulus;
D_τ = degradation factor for ultimate skin friction;
d = pile diameter;
d_b = diameter of pile base;
E_c = soil modulus after cyclic loading;
E_p = pile modulus;
E_s = soil modulus for static loading;
F_ρ = loading rate parameter;
K_c = cyclic stiffness of pile;
K_{c1} = cyclic stiffness of pile after 1 cycle;
L = embedded pile length;
N = number of cycles;
P_c = half amplitude of cyclic load = $(P_{max} - P_{min})/2$;
P_o = ambient (or mean) axial load;
P_{uc} = ultimate load capacity after cycling;
P_{us} = ultimate static load capacity;
P_{max} = maximum load;
P_{min} = minimum load;
p_{bu} = ultimate base pressure;
p_{bus} = value of p_{bu} after cycling;
p_{bs} = value of p_{bu} for static loading;
s_u = undrained shear strength of soil;
T = cyclic loading period;
t = modulus degradation parameter;
w = proportion of interface cyclic stress or strain used for modulus degradation estimate;
z = depth below surface;
γ_c = cyclic shear strain;
γ_{cr} = critical value of shear strain;
γ_r = reference rate of loading for which static parameters are determined;
γ_s = static shear strain for failure of triaxial sample;
γ_{ss} = critical shear strain for skin friction;
ζ = parameter defined in Eq. 4;
ν_s = Poisson's ratio of soil;
ρ_c = cyclic displacement (double amplitude);
ρ_o = mean pile settlement;
τ_a = ultimate skin friction;
τ_{ac} = value of τ_a after cycling;
τ_{as} = static falue of τ_a; and
ψ = number defined in Eq. 4.

JOURNAL OF THE GEOTECHNICAL ENGINEERING DIVISION

EMBEDDED ANCHOR RESPONSE TO UPLIFT LOADING

By Andreas Andreadis,[1] Roger C. Harvey,[2] and Eldon Burley[3]

INTRODUCTION

Embedded anchors or ground achors which may consist of a deeply embedded plate, bulb, or flukes connected to the anchored structure by means of a cable or tie-rod have recently been the subject of much technical literature dealing with both research and practice (8,10,19,21). Their potential as an acceptable anchor for close station keeping in the marine environment has also been recognized and a number of systems have been developed (6,14,17,26) which, as ocean operations move into yet deeper waters, may prove increasing importance (12,13,15,16).

As a sea bed anchor can be subjected to a wide range of loading conditions including sustained or static, repeated, and sustained-repeated combinations, it is essential to obtain a thorough understanding of soil-anchor interaction. In particular, an appreciation of the life of the system and influence of installation techniques (3) are important factors as the ability to efficiently design these anchors may significantly reflect on the overall economics of future facilities.

TEST EQUIPMENT

The anchor models used in the investigation are shown in Figs. 1 and 2. Those in Fig. 1 were designed to be installed vertically using a fluidization process. Some cylindrical anchors contained pore pressure gages and a system capable, if required, of eliminating cyclic creep effects (4).

[1]Civ. Engr., Sani S.A., Thessaloniki, Greece.
[2]Lect. in Civ. Engrg., Queen Mary Coll., Univ. of London, Mile End Rd., London, E1 4N5, England; also Dir. of Queen Mary Coll. Anchor Tech. Limited, London, England.
[3]Sr. Lect. in Civ. Engrg., Queen Mary Coll., Univ. of London, Mile End Rd., London, E1 4N5, England; also Dir. of Queen Mary Coll. Anchor Tech. Limited, London, England.

Note.—Discussion open until June 1, 1981. To extend the closing date one month, a written request must be filed with the Manager of Technical and Professional Publications, ASCE. Manuscript was submitted for review for possible publication on February 21, 1980. This paper is part of the Journal of the Geotechnical Engineering Division, Proceedings of the American Society of Civil Engineers, © ASCE, Vol. 107, No. GT1, January, 1981. ISSN 0093-6405/81/0001-0059/$01.00.

Fig. 2 shows a model fluke system which was installed (with closed flukes) by driving. At a predetermined depth the flukes were unlocked by activating an explosive bolt. The final phase of driving caused the soil bearing pressure to force the flukes open until the contained angle was 90°; the locked flukes then offered a substantial withdrawal resistance during subsequent testing.

The tests were performed in a steel tank measuring 8 ft (2.44 m) in diam and 4 ft (1.22 m) deep, positioned on a vibrating table and filled with a fine–medium, uniform, saturated sand (Borough Green sand) with engineering properties presented in Table 1. Additional tests were carried out in Bush Farm sand,

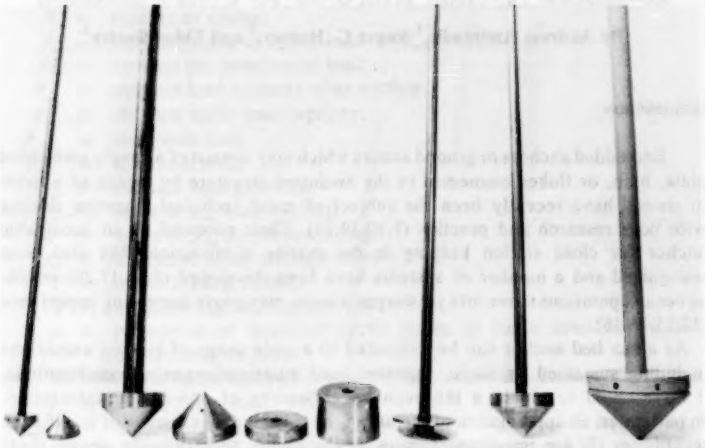

FIG. 1.—Cylindrical, Conical, and Plate Anchors

also shown in Table 1. The table has been drawn up in accordance with the Unified Soil Classification, with the visual information following the Rittenhouse and Krumbein methods. The standard methods used for determining the soil properties were in accordance with the American Society for Testing and Materials (ASTM) (1970).

The size of the test container was chosen to reduce boundary effects (which have been shown (22,27) (for deep anchors embedded in dense sands) to be present at a distance in excess of 10 anchor diameters from the loaded anchor. Additionally, the method of soil bed preparation had to take into account the large masses of soil and water involved, a total of approximately 10 metric tons. Repeatable soil beds of known properties were obtained using vibratory techniques (2,5) after installation of the model anchors. Soil pressure gages embedded in the sand mass monitored the soil pressures before and during testing.

The complete testing equipment is shown in Fig. 3 and consists of the test tank mounted on a vibrating table with a servo-controlled hydraulic loading system attached to the rigid steel frame. This applied, by means of a function generator, a variety of static and cyclic uplift loading patterns to the anchor.

Static Loading Tests

These tests were carried out to determine the influence of anchor configuration and other factors involved on the ultimate static uplift capacity and response

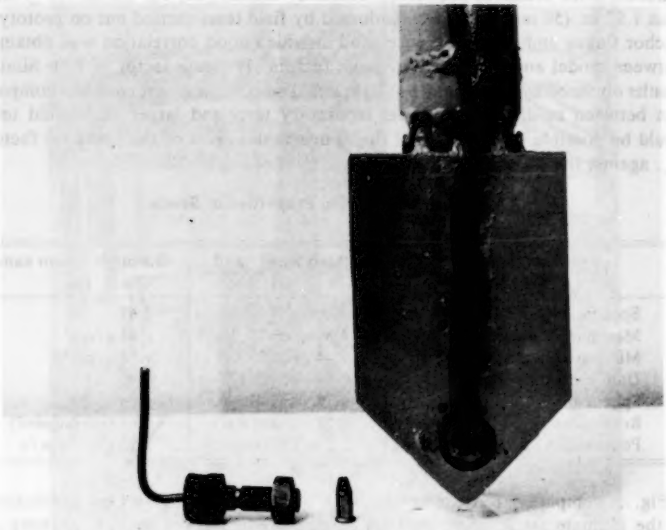

FIG. 2.—Fluke Anchor and Explosive Bolt

to different levels of static loading. A pull-out rate of 0.5 mm/min, which permitted free drainage around the anchor body during testing, was generally adopted. Similar results were found for anchor tests in both Borough Green and Bush Farm sands.

Influence of Relative Depth and Anchor Size.—Fig. 4 presents typical static test data in terms of the static breakout factor, N_γ, against the relative depth, λ, ($= D/B$) in which D = the anchor depth; and B = the lateral dimension

of the plate or fluke. The breakout factors increase with depth at shallower depths and then tend to approximately constant values. For shallow depths the ultimate uplift capacity increases at a rate greater than in proportion to D^2, but as the depth of embedment increases and failure becomes more localized there is not the same dependence on depth as for the shallow anchor, and the ultimate load-relative depth relationships tend to become linear.

It has been established (27) that significant scale effects are present when comparing small-scale anchor results with medium and larger scale results. Although breakout factors increased significantly for anchor plate diameters less than 1.97 in. (50 mm), it appeared that scale effects were considerably reduced, with breakout factors substantially unchanged, for diameters greater than 1.97 in. (50 mm). This was endorsed by field tests carried out on prototype anchor flukes embedded in dense sand in which good correlation was obtained between model and prototype breakout factors (2) (Scale factor = 3.4). Similar results obtained by other authors (7,18,25,28) who suggest that cautious comparison between medium-scale model laboratory tests and larger scale field tests could be possible on the basis of the dimensionless plot of the breakout factor, N_γ, against the relative depth, D/B.

TABLE 1.—Engineering Properties of Sands

Variable (1)	Bush Farm sand (2)	Borough Green sand (3)
Specific gravity	2.66	2.67
Maximum dry density	1.80 g/cm^3	1.67 g/cm^3
Minimum dry density	1.44 g/cm^3	1.38 g/cm^3
Uniformity coefficient	2.10	1.40
Sphericity	0.75	0.85
Roundness	0.25 (subangular)	0.41 (subrounded)
Permeability (at D_r = 70%)	2.2×10^{-2} cm/s	3.5×10^{-3} cm/s

Fig. 5 compares the test results with a number of theoretical predictions of the ultimate static uplift capacity. Uplift prediction for shallow anchors do not, in general, yield good results mainly due to the assumption of a unique failure surface shape for all soils, in addition to an inadequate representation of the soil forces at failure. The complex soil-anchor interaction problem appears to be oversimplified by these methods. Meyerhof and Adams' (22) deep anchor analysis yields comparatively good results although at greater depths the theoretically defined sliding surfaces were not observed to occur (7,20). Mariupol'skii's (21) and Vesic's (29) solutions for deep anchors grossly underestimate the observed capacities. Maddocks (20) noted that the behavior of a deep plate anchor in a dense sand bed was a combination of local compaction and shearing of the same immediately above the plate with the lifting of large zones of sand above the local activity. This response is clearly more complex than the behavior predicted by the expanding cavity method (11,29,30). Kupferman's (18) solution takes into account the observed failure mechanism, but the contribution of a much larger zone of soil observed to suffer displacements at failure is ignored.

Examination of the influence of relative depth on the relative movement, $\delta_s \delta_{sf}$, in which δ_s and δ_{sf} are the movement due to static loading and movement

at static failure, respectively, show that the relative movements increase with relative depth in a manner similar to the increase of the breakout factors. A

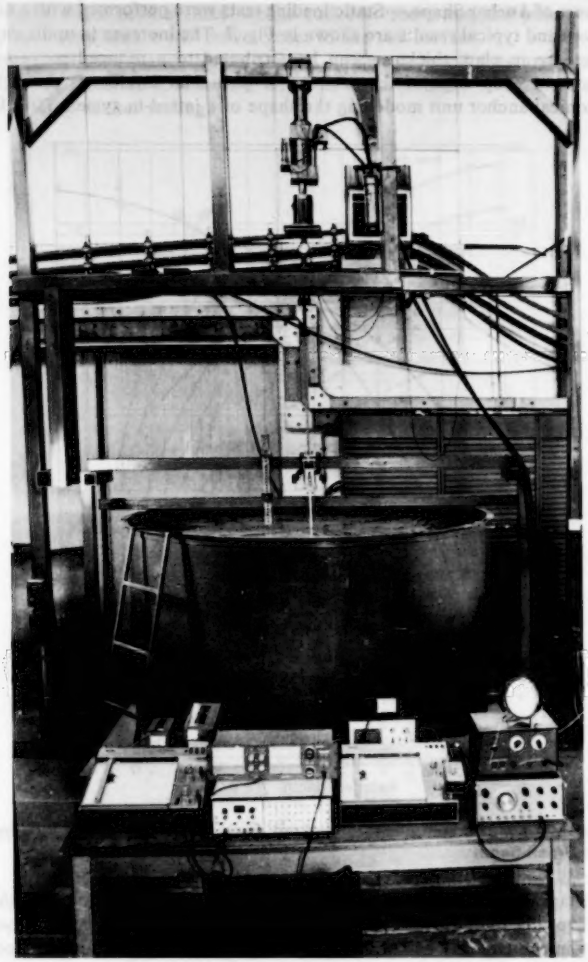

FIG. 3.—Testing Equipment

dimensionless plot of the anchor load-displacement characteristics, shown in Fig. 6, suggests that within the limits of experimental accuracy, a unique relationship for cylindrical anchors embedded in undisturbed dense sands exists

for all relative depths. Such a relationship depends mainly on the relative density of the soil and subsequently on the embedment method in addition to the total relative cyclic movement the anchor has experienced, as will be later explained.

Influence of Anchor Shape.—Static loading tests were performed with a number of anchors and typical results are shown in Fig. 7. The increase in uplift capacity with increase in plate thickness can be attributed to a reduced movement of soil around the top edge of the anchor. Of particular interest is the behavior of the conical anchor unit modelling the shape of a jetted-in system (26). During

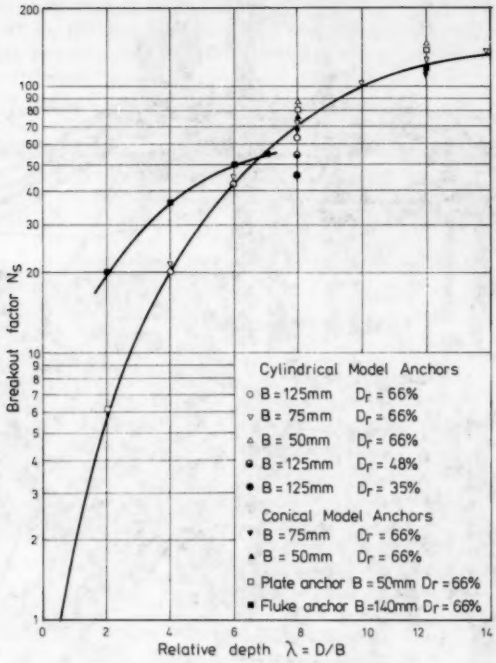

FIG. 4.—Static Load Tests: Anchor Breakout Factor, Relative Depth Relationship (Borough Green Sand)

the early stages of loading the anchor exhibits a similar load-displacement behavior to the plate and cylindrical anchor. However, as loading increases, a sudden reduction in the capacity of the conical anchor leads to a substantially reduced ultimate capacity. This reduction is considered to be due to the increased flow of soil beneath the anchor, thus reducing the effective confining soil pressures.

Comparison of the cylindrical and fluke anchor breakout factors in Fig. 4 shows that the fluke anchor displays relatively higher breakout factors at shallower depths. However, as the relative depth increases, the more "aerodynamic" wedge fluke shape apparently allows local shear failure conditions to more easily

develop at reduced depths. This conclusion was endorsed by comparison of the post-peak behavior of the anchors at shallow depths in which the fluke anchor displays a deeper failure mechanism than the cylindrical anchor. Clearly, as the apex angle of the fluke wedge reduces, the transition point between shallow and deep failure will move closer to the soil surface.

Extent of Soil Disturbance during Testing.—Electronic soil pressure gages were embedded at specified locations in the soil mass in order to monitor the soil stresses during anchor testing.

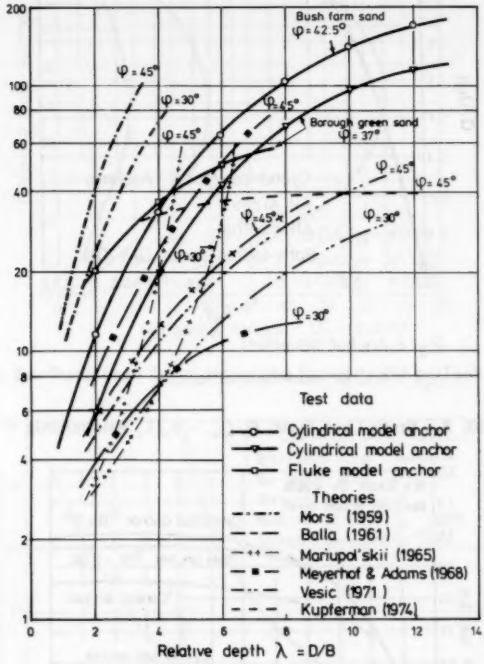

FIG. 5.—Comparison of Static Load Data with Previous Theoretical Work

Fig. 8 shows the distribution of horizontal stresses at the tank wall during the testing of a 4.92 in. (125 mm) diam cylindrical model anchor. This is equivalent to 9.6 times the anchor body diameter from the tested anchor and similar results were obtained during the testing of a 2.95 in. (75 mm) diam anchor. It is evident that at such distances significant horizontal stresses are generated in the soil mass. The stresses increase rapidly from zero at the soil surface to a maximum value and then decrease again to zero just below the level of embedment of the anchor plate. The position of the peak value depends on the distance of the monitored stress profile from the loaded anchor, e.g., at distances greater than five anchor diameters, maximum horizontal stresses develop at a depth

equal to half the embedment depth of the anchor. Closer to the loaded anchor body horizontal soil stresses substantially increase (see Fig. 9) and the position of the peak value shifts nearer to the anchor body. The magnitude of the stresses

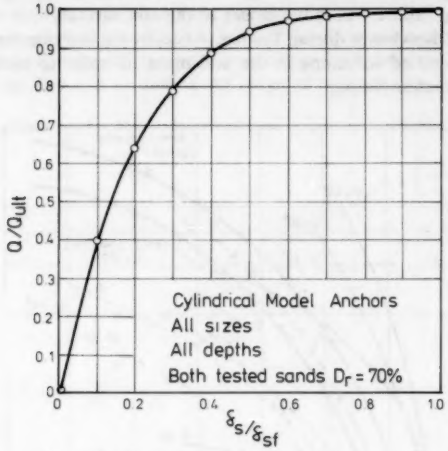

FIG. 6.—Static Load Tests: $Q/Q_{ult} - \delta_s/\delta_{sf}$ Relationship

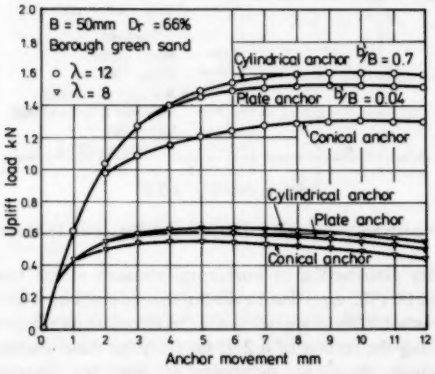

FIG. 7.—Static Load Tests: Uplift Load-Anchor Movement Relationship

appears to be significantly affected by both anchor size and relative depth of embedment.

Fig. 10 shows typical increases in the horizontal stress at a specified location

in the soil mass during a static loading test. Horizontal soil stresses measured as distant as 16 anchor diameters from the loaded anchor continue to increase in a mode characteristically similar to the load-displacement behavior of the anchor. After the anchor resistance peaks and displacement takes place at constant

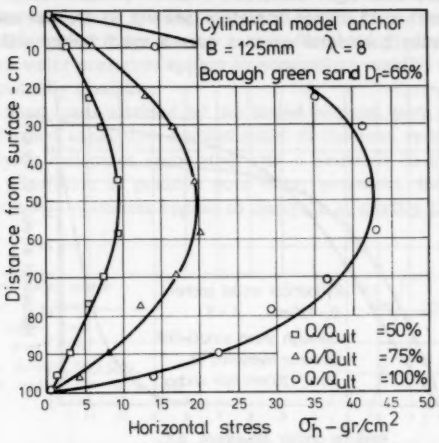

FIG. 8.—Static Load Tests: Horizontal Stress Profile on Tank Wall

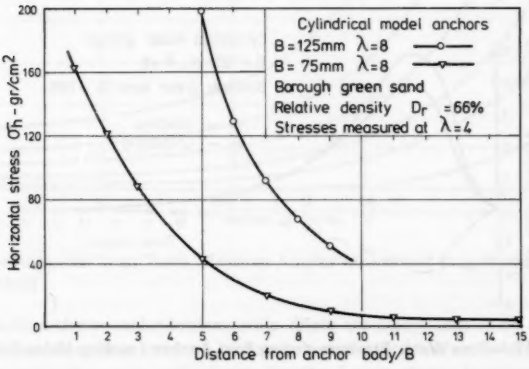

FIG. 9.—Static Load Tests: Horizontal Stress-Relative Distance from Anchor Body Relationship

load, the soil stresses continue to increase at a reduced rate and tend to a constant value when the anchor resistance falls.

This behavior suggests that a much larger mass of sand is affected by anchor testing than had previously been considered. Stereo photogrammetric techniques,

used to obtain accurate representations of sand grain displacements around the anchor plate (7,20) are probably unable to reveal the entire zone of stressed soil, as dense sands appear capable of mobilizing and transferring substantial stresses without easily detectable grain movements. For anchors embedded at relative depths, less than eight horizontal stresses become rather insignificant at distances greater than 15 anchor diameters (see Fig. 9). Deeper anchors appear to develop significant horizontal stresses over a much larger soil zone and if

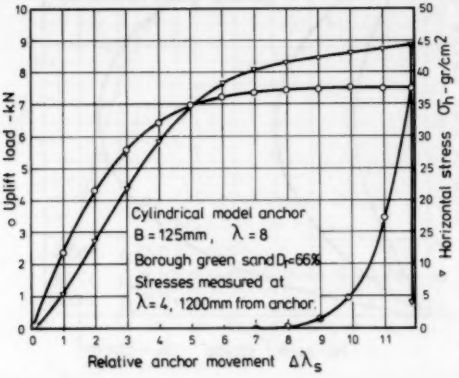

FIG. 10.—Static Load Tests: Horizontal Stress-Relative Anchor Movement Relationship

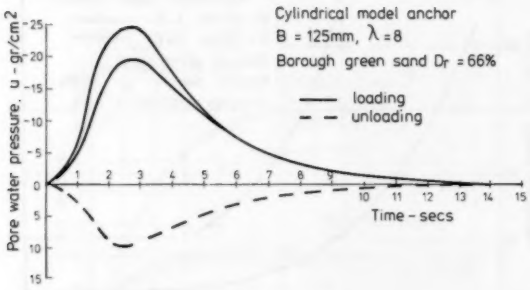

FIG. 11.—Pore Water Pressure during Fast Anchor Loading-Unloading

this zone is restrained some interference in the static loading behavior of an anchor could be anticipated (27).

Vertical soil stresses, developed due to anchor testing, were also measured. These stresses were, as expected, substantial above and near the anchor body. However, their variation with distance from the anchor showed a very marked reduction compared to the horizontal stresses, and at distances greater than five anchor diameters no significant effects could be detected.

Influence of Pore Water Pressures.—The selected testing rates were chosen to provide essentially drained tests. However, if stresses are rapidly applied to dense cohesionless soils, only a limited dissipation of induced negative pore pressures will take place resulting in partially drained conditions, and therefore increased initial holding capacities.

Fig. 11 presents typical readings obtained by the pore pressure gages fitted below the anchor plate edge during a very fast load application (snap load). Negative pore water pressures appear to accumulate rapidly, reach a maximum value, and gradually dissipate.

Maximum snap loads attained by the tested anchors were more than double their static drained capacities. Sudden relief of the load resulted in a rebound of the overlying soil mass associated with a decrease in the volume of the voids and a generation of positive pore water pressures. Induced negative or positive pore water pressures appear to dissipate at exactly the same rate (Fig. 11).

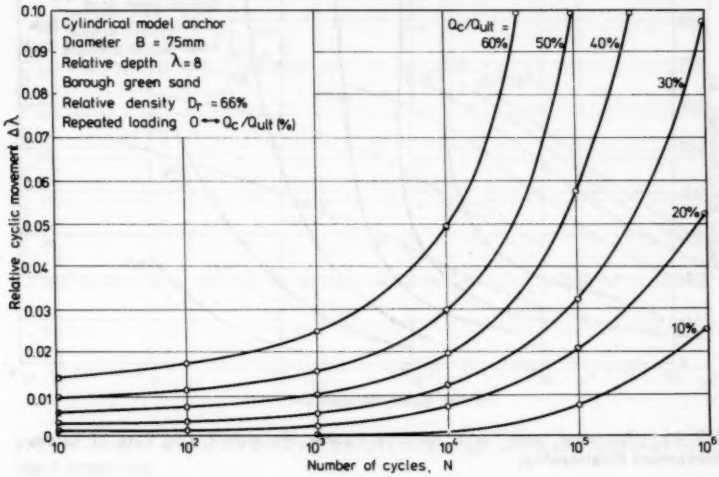

FIG. 12.—Repeated Load Tests: Relative Anchor Movement (Log Number of Cycles Relationship)

As medium dense cohesionless soils dilate markedly less than denser soils when subjected to shear stresses, increases in undrained anchor holding capacities decreased with decreasing soil relative density. Loose or very loose sands develop positive pore pressures, and the undrained holding capacities are expected to be reduced in comparison with the drained case.

Repeated and Sustained-Repeated Loading Tests

Each anchor was subjected to repeated loading which consisted of a continuous sinusoidal loading pattern. Various different repeated loading and sustained-

repeated loading combinations were used and similar results were found for anchor tests in both soils.

A standard cyclic period of 2 sec was adopted as a result of preliminary investigations employing several loading periods from 1–30 sec. It was judged that a frequency of 0.5 Hz introduced negligible inertia forces and testing was therefore essentially nondynamic. Additionally, the pore pressure gage readings indicated drained conditions. The adoption of a 2-sec loading period advantageously permitted accelerated testing and approximately 500,000 loading cycles could be obtained in 12 days.

Influence of Relative Depth and Anchor Size.—Previous investigations into the repeated loading characteristics of shallow and deeply embedded fluke, plate, and cylindrical anchors (1,18,20,23,24) suggest that the basic response of each

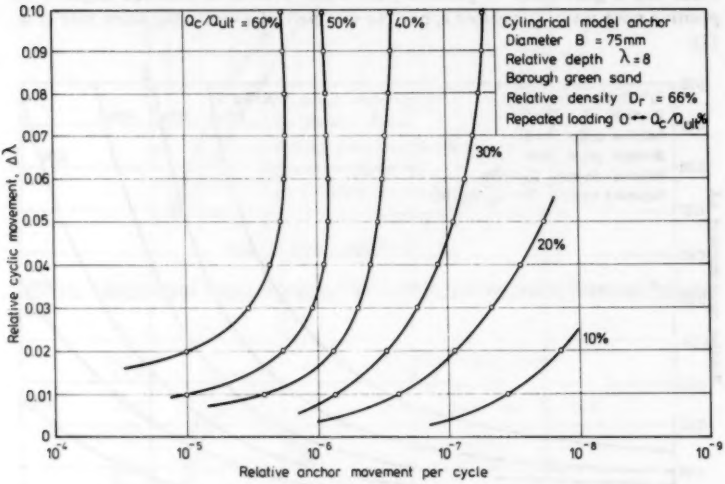

FIG. 13.—Repeated Load Tests: Relative Anchor Movement (Log Rate of Relative Movement Relationship)

anchor is similar. In the early stages of the test the upward displacement accumulates rapidly. However, if cyclic loading amplitudes are kept below a critical value, the rate of displacement of the anchor continues to reduce but never ceases. For shallow anchors, $D/B < 8$, an increase in the rate of movement may eventually occur (18) due to reduction of the relative depth as the anchor displaces upwards. For very deep anchors, $D/B > 40$, however, the soil surface influence is limited and as the test progresses the system appears to become more stable (9). On the other hand, if cyclic loading amplitudes exceed a critical value, the net upward displacement for successive load repetitions increases, instability occurs, and the system fails.

Fig. 12 presents a typical repeated loading response of a cylindrical model anchor embedded in dense Borough Green sand. The data is presented in terms of the accumulating relative anchor movement, $\Delta\lambda$, against the logarithm of

number of load cycles, log N. The anchor is subjected to loadings which are in the form of sine waves oscillating between zero load and specified peak relative cyclic load values, Q_c/Q_{ult}, expressed as a percentage of the ultimate drained static capacity of the anchor. In all cases, an unceasing anchor movement develops, its rate initially tending to decrease with time. As the test progresses, however, the gradients of the curves increase indicating approaching failure.

Repeated loading behavior of a particular anchor system can be represented by a family of hyperbolic curves expressed by equations of the form

$$\log\left(\frac{N}{10}\right) = \frac{\Delta\lambda - c}{a + b(\Delta\lambda - c)} \quad (1)$$

in which a, b, and c = cyclic loading constants.

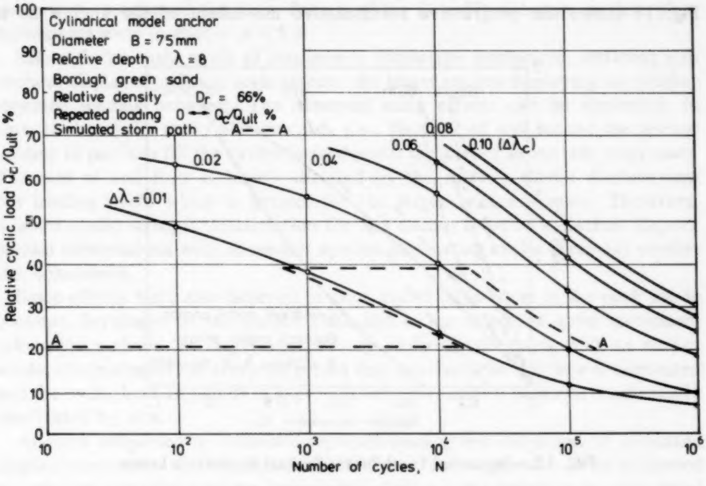

FIG. 14.—Life of Anchor for Different Relative Movement Limits as Function of Cyclic Load Amplitude

Similar families of hyperbolic curves were found to exist for different relative depths, sand densities, anchor sizes and shapes, installation methods, sustained-repeated loading combinations, as well as for varying degrees of soil flow around and under the anchor. It appears, therefore, that the proposed method of analysis could be formalized to express the basic cyclic loading displacement and failure characteristics of the majority of embedded sea bed anchors.

Fig. 13 shows the accumulated relative anchor movement plotted against the rate of relative deformation on a semilogarithmic scale. Failure of the anchor system, the definition of which has caused difficulties in the past, can be defined as the turning point on the rate of relative movement against the relative anchor displacement curve. Past the critical point, the net anchor movements per cycle increase and failure takes place rapidly.

The strain corresponding to the minimum point is the critical cyclic relative

movement, $\Delta\lambda_c$, and appears to vary both with depth of embedment and relative cyclic load. For design purposes, however, a mean value of $\Delta\lambda_c$ equal to 0.1 for the tested anchors can be used. Accumulated relative anchor movements in excess of the critical value will imply imminent failure. Subsequent testing showed that anchors experiencing total strains below the critical value display negligible drops in their ultimate static capacities.

The definition of repeated loading failure clearly implies that cyclic strength deterioration can be best explained as a strain dependent phenomenon. Further proof was obtained by the post-cyclic response to loading, in addition to subjecting the anchors to groups of cycles with the same frequency but with varying stress amplitudes. It appears that the deterioration in the cyclic loading-relative movement properties is due to the accumulated amount of anchor cyclic relative movement, whether developed by a few strong or many small stress pulses. Fig. 14 shows the progressive accumulative movement of the anchor as it

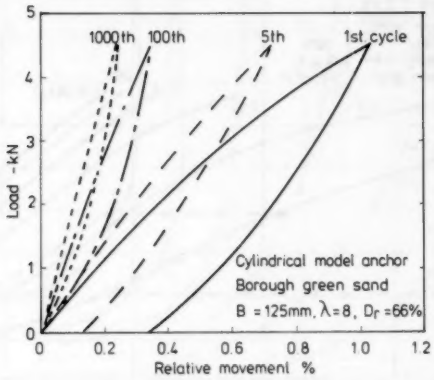

FIG. 15.—Repeated Load Tests: Typical Hysteresis Loops

developed after three simulated consecutive two-day storms with equivalent uniform repeated load amplitudes, Q_c/Q_{ult}, of 20%, 40%, and 20%, respectively.

During testing it was observed that the area of the hysteresis loop decreases in size (see Fig. 15). A near stable shape of hysteresis loop is achieved after the first few thousand cycles although a small permanent upward displacement continues to accumulate. After the critical relative movement ($\Delta\lambda_c$) is reached, the permanent upward anchor displacements increase and the hysteresis loop becomes larger until the anchor is pulled from the soil.

The repeated loading characteristics of an embedded anchor are significantly affected by the installation depth and the upward movements of an anchor subjected to a given relative cyclic load increase as the relative depth increases. Although it appears that a weaker repeated loading behavior is displayed by deeper anchors, a different picture of anchor efficiency emerges if repeated loading characteristics are compared in terms of absolute rather than relative cyclic loading amplitudes. Thus load changes between zero and 1.0 kN correspond

to 60% of the uplift capacity of an anchor for which $B = 2.95$ in. (75 mm) and $\lambda = 8$, but only 23% of the uplift capacity of the same anchor installed at $\lambda = 12$. The former, when cycled at $Q_c/Q_{ult} = 60\%$, will fail after 35,000 load repetitions whereas the latter when cycled at $Q_c/Q_{ult} = 23\%$ will fail at 175,000 cycles, a five-fold increase in life. Greater improvements in life in favor of deeper systems were observed when the repeated loading characteristics of anchors embedded at relative depths of 4 and 8 were examined.

For the tested anchors the critical cyclic relative movement, $\Delta\lambda_c$, corresponding to failure could be regarded as 0.1. Tests show, however, that $-\Delta\lambda_c$ values increase with increasing relative depth of embedment. As the soil surface influence diminishes, large cyclic relative displacements must be attained before the rate of anchor movement starts to accelerate. This conclusion has been endorsed by other writers (9) who have shown that no increase of displacements per cycle were monitored for very deep anchors ($\lambda = 87$) although anchor plate movements were in excess of 0.5 B.

Although the basic mode of response is essentially unchanged, different size anchors display significant scale effects, the larger anchor displaying the weaker repeated loading behavior. The observed scale effects can be attributed, in part, to the cyclic creep phenomenon, i.e., the flow of soil around the anchor tending to partially fill the cavity formed under the anchor as the test progresses. The rate of soil flow is largely dictated by the relative elastic displacement per loading cycle which is greater for the larger anchor system. Therefore, a faster cyclic strength deterioration for this anchor must be expected. Experimental observations with an anchor system eliminating cyclic creep (4) verifies this conclusion.

Scale effects were also believed to arise due to differences in the peak cyclic pressure developed on the anchor plate and to the increased grain movement taking place above the larger anchor body. Subsequent testing with an anchor model eliminating cyclic creep suggested that, provided the soil flow is eliminated and the cyclic load amplitude is kept relatively low, anchor behavior is essentially unaffected by size.

Anchors subjected to sustained-repeated loading are subjected to increased displacement at the commencement of the test when compared to those subjected to only the repeated loading component. This weaker behavior is considered to be caused in part by the larger cavity created under the anchor body and also by the higher imposed peak loading. As the test progresses, the stress system developed in the sand above the anchor body is such as to reduce the rate of displacement to levels experienced by the same anchor system subjected solely to the repeated loading component. Thus the cyclic relative movement of anchors subjected to sustained-repeated loading combinations, $\Delta\lambda_{sr}$ can be derived with reasonable accuracy from the equation

$$\Delta\lambda_{sr} = \Delta\lambda + d \qquad (2)$$

in which $\Delta\lambda$ = the cyclic relative movement of the anchor subjected only to the repeated loading component; and d = the corresponding cyclic loading constant.

It is interesting that the relative elastic displacement per loading cycle reduces as the sustained load amplitude increases and the most severe elastic displacements occur when the anchor is completely unloaded during each cycle of loading.

As the surface influence reduces there are indications that anchors subjected solely to repeated loading could display a marginally weaker response. Similar results have been reported by other workers (20,9).

Influence of Anchor Shape.—Comparative tests were performed on cylindrical and conical anchors and identical repeated loading behavior was found. In the case of the fluke anchor, response was similar except that the fluke anchor displayed a slightly weaker behavior.

It is of interest to record that Kupferman (18) performed repeated loading tests on model fluke anchors embedded in dense saturated sands. A direct comparison with the information obtained during the present work is attempted in Fig. 16. Considering the differences in fluke size and geometry together with the variations in the soil properties, preparation, and testing procedures, the overall correspondence appears to be reasonable.

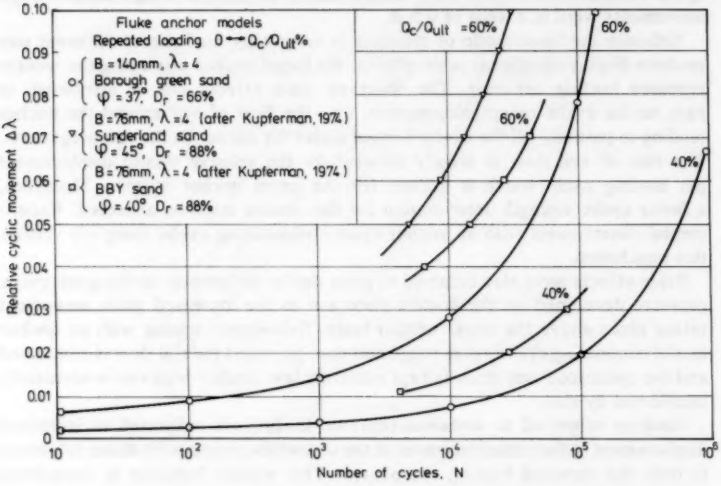

FIG. 16.—Repeated Load Tests: Comparison with Kupferman's Data (1974)

Stress Distribution around Anchor.—Cyclic soil stresses oscillate in a sinusoidal pattern identical in form to, and of the same frequency as, the loading wave. Their magnitude is mainly related to the amplitude of the loading change during each cycle and it increases substantially as the loaded anchor plate is approached.

A comparison of the static and cyclic horizontal stresses that develop in the soil mass when the anchor is loaded from 0–40% of its ultimate uplift capacity either once or in a repetitive manner is shown in Fig. 17. It is clear that after the initial application of load the effects of the repeated applications of loading are confined to a limited soil zone surrounding the anchor body.

Maddocks (20) carried out stereo-photogrammetric observations of plane strain anchor models and concluded that sand deformations associated with stresses developed by each cycle of loading were very small and restricted to a limited area.

Finally, the vertical cyclic stresses developed in the soil during repeated loading showed a very marked reduction when compared to the corresponding vertical static stresses.

Post Cyclic Response to Loading.—Tests were performed in which the anchor, after having been subjected to repeated loading, was then loaded at a constant rate to static failure. A stiffening in the anchor displacement characteristics was found, as compared to that demonstrated by only static loading, which was associated with the soil density changes and supported by evidence of progressive reductions in the area of the hysteresis loops. Anchors subjected to a few strong or many small stress pulses, or to any sustained-repeated load combination, increase their resistance to displacement at a decreasing rate as the cyclic movement accumulates. They attain an ultimate hardening value when a particular cyclic strain limit is achieved. Past this limit no further stiffening occurs.

It appears that this cyclic strain limit can be related to the critical cyclic

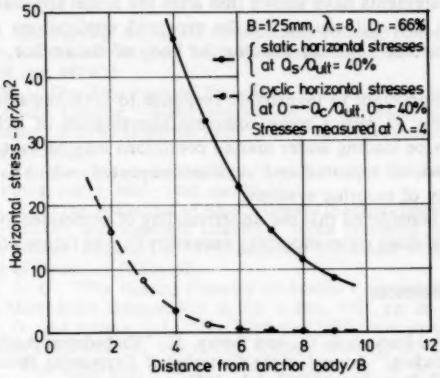

FIG. 17.—Comparison of Static: Cyclic Horizontal Stresses

relative movement as corresponding to anchor failure. Indeed, the inability of the sand mass after failure to competently resist further applications of load, denoted by gradual increase in the rate of cyclic movement, appears to be associated with its inability to mobilize greater stiffness. Anchors deeply embedded displace more before failure occurs, thus increases in their stiffness characteristics for a given cyclic movement tend to be less pronounced.

Conclusions

This work has attempted to provide a better understanding of the behavior of embedded anchors. The anchors were subjected to both sustained and sustained-repeated loading combinations. Attention has been focused on a number of important features relating to both general response and failure criteria. The following brief conclusions may be considered applicable.

1. The mode of failure of an anchor subjected to static loading is mainly controlled by the relative depth of embedment, soil relative density, and anchor shape. Static breakout factors and relative anchor movements to failure increase sharply with relative depth of embedment at shallow depths, tending to an approximate constant at greater depths.

Significant horizontal stresses develop in the sand mass in a zone which can extend considerably in excess of 10 anchor diameters either side of a deeply installed anchor.

2. The repeated applications of load to an anchor substantially reduce its resistance to load and a nonrecoverable movement develops. A realistic failure criterion can be interpreted using a rate of deformation technique which is defined by unacceptably high relative relative movements of the anchor resulting in significant reductions in post-cyclic pull-out capacity.

Anchor movement, due to successive repeated applications of load at varying amplitudes, can be predicted by using an experimentally observed strain dependent hypothesis.

Stress measurements have shown that after the initial application of the load, the effects on the soil caused by the repeated applications of the load are confined to a limited zone surrounding the body of the anchor.

It has been important to investigate response to both sustained and repeated loading, not only to gain a more complete appreciation of behavior, but also because in-service loading under marine conditions may be sustained only, e.g., sub-sea systems, or repeated and sustained-repeated, which is likely to apply for the majority of mooring systems.

Finally, it is considered that the understanding of embedded systems is crucial for the design of deep water moorings necessary for the future offshore industry.

Appendix I.—References

1. Andreadis, A., Harvey, R. C., and Burley, E., "Embedment Anchors Subjected to Repeated Loading," *Journal of the Geotechnical Engineering Division*, ASCE, Vol. 104, No. GT7, Proc. Paper 13867, July, 1978, pp. 1033–1036.
2. Andreadis, A., "Uplift Resistance of Embedded Sea Bed Anchors," thesis presented to Queen Mary College, University of London, at London, England, in 1979, in partial fulfillment of the requirements for the degree of Doctor of Philosophy.
3. Andreadis, A., Harvey, R. C., and Burley, E., "Embedded Sea Bed Anchors Subjected to Repeated Loading," *Transactions of the Royal Institution of Naval Architects*, Vol. 121, 1979.
4. Andreadis, A., and Harvey, R. C., "An Embedded Anchor with an Improved Response to Repeated Loading," *Applied Ocean Research*, Vol. 1, No. 4, Oct., 1979, pp. 171–176.
5. Andreadis, A., Tsangarides, T. S., and Harvey, R. C., "Design of Physical Models to Study Anchor Behaviour," to be published.
6. Bemben, S. M., Kalajian, E. H., and Kupferman, M., "The Vertical Holding Capacity of Marine Anchors in Sand and Clay Subjected to Static and Cyclic Loading," Presented at the May, 1973, 5th Annual Offshore Technology Conference, held at Houston, Tex., Vol. 2, Paper No. 1912, pp. 871–880.
7. Carr, R. W., "An Experimental Investigation of Plate Anchors in Sand," thesis presented to the University of Sheffield, at Sheffield, England, in 1970, in partial fulfillment of the requirements for the degree of Doctor of Philosophy.
8. Hanna, T. H., Sparks, R., and Yilmaz, M., "Anchor Behaviour in Sand," *Journal of the Soil Mechanics and Foundations Division*, ASCE, Vol. 98, No. SM11, Proc. Paper 9338, Nov., 1972, pp. 1187–1208.

9. Hanna, T. H., Sivapalan, E., and Senturk, A., "The Behaviour of Dead Anchors Subjected to Repeated and Alternating Loads," *Ground Engineering*, Vol. 11, No. 4, Apr., 1978, pp. 28–34 and 40.
10. Harvey, R. C., and Burley, E., "Behaviour of Shallow Inclined Anchorages in Cohesionless Sand," *Ground Engineering*, Vol. 6, No. 5, June, 1973, pp. 48–55.
11. Harvey, R. C., Burley, E., and Daniel, A. W. T., "Cavitation in Semi-infinite Granular Media," *Civil Engineering*, Vol. 812, Mar., 1974, pp. 52–55.
12. Harvey, R. C., and Burley, E., "Embedded Sea Bed Anchors for the North Sea," *The Naval Architect, Journal of the Royal Institution of Naval Architects*, No. 5, Sept. 1976, pp. 151–152.
13. Harvey, R. C., and Burley, E., "A Proposal for the Development of a Sea Bed Anchor," *Journal of the Society for Underwater Technology*, Vol. 3, No. 1, Apr., 1977, pp. 9–11.
14. Harvey, R. C., Burley, E., and Nath, B., "The Development of an Embedded Sea Bed Anchor to Provide Multi-Directional Restraint," Presented at the Mar., 1978, International Offshore Conference, held at Brighton, England, pp. 97–107.
15. Harvey, R. C., Burley, E., and Nath, B., "Sea Bed Anchor Development," *Civil Engineering*, No. 9, Sept., 1978, pp. 83–87.
16. Harvey, R. C., Burley, E., and Nath, B., "Some Thoughts on Sea Bed Anchors," *Journal of the Society for Underwater Technology*, Vol. 4, No. 4, Dec., 1978, pp. 8–15.
17. Kerr, N., "A Self-Burying Anchor of Considerable Holding Power," Presented at the May, 1976, 8th Annual Offshore Technology Conference, held at Houston, Tex., Paper No. 2466, pp. 447–455.
18. Kupferman, M., "The Behaviour of Embedded Marine Anchor Flukes Subjected to Static and Cyclic Loading," thesis presented to the University of Massachusetts, at Amherst, Mass., in 1974, in partial fulfillment of the requirements for the degree of Doctor of Philosophy.
19. Littlejohn, G. S., "Recent Developments in Ground Anchor Construction," *Ground Engineering*, Vol. 1, No. 3, Mar., 1968, pp. 32–36.
20. Maddocks, D. V., "The Behaviour of Model Ground Anchors Installed in Sand and Subjected to Pull-Out and Repeated Loading," thesis presented to the University of Bristol, at Bristol, England, in 1978, in partial fulfillment of the requirements for the degree of Doctor of Philosophy.
21. Mariupol'skii, L. G., "The Bearing Capacity of Anchor Foundations," *Osnovaniya, fundamenty i Meckhanika Gruntor*, Vol. 3, No. 1, Jan., 1965, pp. 26–32.
22. Meyerhof, G. G., and Admas, J. I., "The Ultimate Uplift Capacity of Foundations," *Canadian Geotechnical Journal*, Vol. 5, No. 4, Dec., 1968, pp. 225–244.
23. Senturk, A., "The Behaviour of Plate Anchors Subjected to Repeated Loading," thesis presented to the University of Sheffield, at Sheffield, England, in 1977, in partial fulfillment of the requirements for the degree of Master of Engineering.
24. Sivapalan, E., "The Behaviour of Plate Anchors Subjected to Repeated Loading," thesis presented to the University of Sheffield, at Sheffield, England, in 1976, in partial fulfillment of the requirements for the degree of Master of Engineering.
25. Sutherland, H. B., "Model Studies for Shaft Raising through Cohesionless Soils," *Proceedings of the 6th International Conference on Soil Mechanics and Foundation Engineering*, Vol. 2, Mar., 1965, pp. 410–413.
26. Taylor, R. J., Jones, D., and Beard, R. M., "Handbook for Uplift Resisting Anchors," Civil Engineering Laboratory, Naval Construction Center, Port Hueneme, Calif., Sept., 1975.
27. Tsangarides, S., "The Behaviour of Ground Anchors in Sand," thesis presented to the Queen Mary College, University of London, at London, England, in 1978, in partial fulfillment of the requirements for the degree of Doctor of Philosophy.
28. Vesic, A. S., "Experiments with Instrumented Pile groups in Sand," American Society for Testing and Materials Symposium on Performance of Deep Foundations, *Paper No. 444*, 1968, pp. 177–222.
29. Vesic, A. S., "Breakout Resistance of Objects Embedded in Ocean Bottom," *Journal of the Soil Mechanics and Foundations Division*, ASCE, Vol. 97, No. SM9, Proc. Paper 8372, Sept., 1971, pp. 1183–1205.
30. Vesic, A. S., "Expansion of Cavities in Infinite Soil Mass," *Journal of the Soil*

Mechanics and Foundations Division, ASCE, Vol. 98, No. SM3, Proc. Paper 8790, Mar., 1972, pp. 265–290.

Appendix II.—Notation

The following symbols are used in this paper:

A = net area of anchor plate;
B = lateral dimension of plate or flukes;
a, b, c, d = cyclic loading constants;
b' = thickness of anchor plate;
D = depth of embedment;
D_r = relative density of soil;
N = number of loading cycles;
$N_s = (Q_{ult})/A\delta' D)$ = static breakout factor;
Q = anchor uplift load;
Q_{ult} = ultimate static load;
Q_c = peak cyclic load;
Q_s = sustained load;
Q_c/Q_{ult} = relative cyclic load, as a percentage;
Q_s/Q_{ult} = relative sustained load, as a percentage;
δ' = submerged unit weight of soil;
$\lambda = D/B$ = anchor relative depth;
Δ = anchor movement;
$\Delta\lambda$ = anchor movement due to cyclic loading (B ratio);
$\Delta\lambda_c$ = critical anchor cyclic relative movement;
$\Delta\lambda_s = \delta_{s/B}$ = relative static movement;
$\Delta\lambda_{sr}$ = anchor movement due to sustained-repeated loading combinations (B ratio);
δ_s = anchor movement due to static loading;
δ_{sf} = anchor movement to static failure; and
ϕ = angle of internal friction of soil.

JOURNAL OF THE GEOTECHNICAL ENGINEERING DIVISION

CONSTRUCTION OF LARGE CANAL ON COLLAPSING SOILS

By Paul C. Knodel,[1] M. ASCE

INTRODUCTION

There are several areas of California where subsiding soils are of significance. Subsidence may occur because of withdrawal of fluids (usually deep subsidence), the drainage of peat lands, or by the application of water to moisture-deficient, low-density soils (usually near-surface subsidence) (7). Only one type of subsidence, i.e., subsidence caused by the compaction due to wetting, is analyzed in this paper. This process is often referred to as hydrocompaction and has produced widespread subsidence of land surfaces (5).

Deposits that subside because of hydrocompaction are generally one of two types: (1) Loose, moisture-deficient alluvial deposits; or (2) moisture-deficient loess and related eolian deposits. These deposits, laid down with an open structure and high porosity and buried with a moisture deficiency and sufficient intergranular strength to support an increasing overburden load, are readily susceptible to compaction when wetting reduces their dry strength. They are generally found in regions where rainfall seldom penetrates below the root zone, and they invariably occur above the water table. Unlike land subsidence resulting from compaction at depth-of-water-bearing deposits due to a reduction of fluid pressure, hydrocompaction is a near-surface phenomenon. Since wetting progresses from the land surface downward, hydrocompaction begins near the surface and progresses downward with the advancing waterfront. This near-surface subsidence is a serious problem and has damaged canals, roads, pipelines, and transmission towers in local areas. It presents particularly serious problems in the construction and maintenance of large canals.

[1]Chf., Geotechnical Branch, Div. of Research, United States Dept. of the Interior, Water and Power Resources Service, Engrg. and Research Center, P. O. Box 25007, Building 67, Denver Federal Center, Denver, Colo. 80225.

Note.—Discussion open until June 1, 1981. To extend the closing date one month, a written request must be filed with the Manager of Technical and Professional Publications, ASCE. Manuscript was submitted for review for possible publication on June 24, 1980. This paper is part of the Journal of the Geotechnical Engineering Division, Proceedings of the American Society of Civil Engineers, © ASCE, Vol. 107, No. GT1, January, 1981. ISSN 0093-6405/81/0001-0079/$01.00.

San Luis Canal

The San Luis Canal is part of the California Aqueduct (see Fig. 1). The canal was designed and constructed by the Water and Power Resources Service as a joint venture with the state of California. (On November, 6, 1979, the Bureau of Reclamation was renamed the Water and Power Resources Service

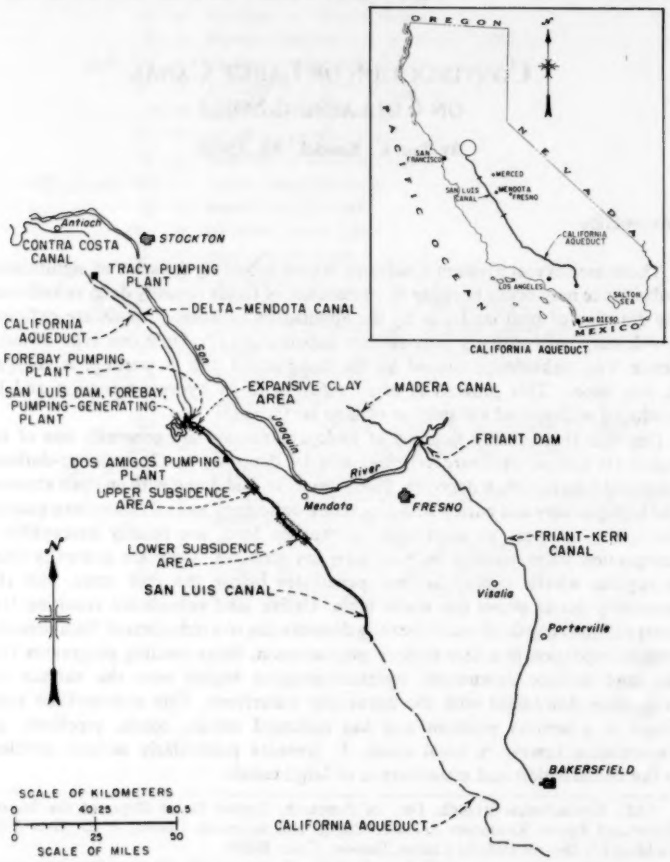

FIG. 1.—Location of Prominent Features, Central Valley, California

of the United States Department of the Interior. The new name more closely identifies the agency with its principal functions—supplying water and power. The text of this publication was prepared prior to adoption of the new name; all references to the Bureau of Reclamation or any derivative thereof are to

be considered synonymous with the Water and Power Resources Service.) The San Luis Canal is 107 miles (172 km) long and has a capacity ranging from 13,100 cu ft/s (370 m^3/sec) at the headworks to 7,750 cu ft/s (220 m^3/sec) at the lower end. It extends from the San Luis Dam near Las Banos to a point near Kettleman City, Calif., where it joins state facilities to the south (see Fig. 1). It is one of the major waterways in the western United States, more than 200 ft (61 m) wide, with water depths up to 33 ft (10 m).

Subsidence Studies of San Joaquin Valley

The United States Geological Survey, in cooperation with the California Department of Water Resources, began a study of subsiding areas in California in 1956. Some of the findings concerning shallow or near-surface subsidence were as follows.

Climate.—One of the controlling factors for the formation of collapsing soils is the climate. The southwestern San Joaquin Valley receives less than 7 in.

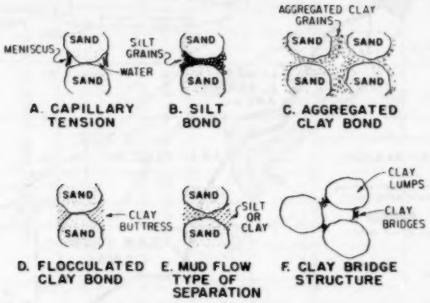

FIG. 2.—Typical Collapsing Soil Mechanisms Which Hold Loose, Bulky Grains in Place

(178 mm) of rainfall per year, and what rain does fall is generally during short, high-intensity storms, separated by long, dry periods (5).

Geomorphology.—Shallow subsidence is confined mainly to the smaller coalescing alluvial fans that apron the foothills along the west and south side of the San Joaquin Valley. Most of the drainage basins contain unconsolidated clayey sediments, have steep slopes, sparse vegetation, and short periods of high rainfall. The intense rainstorms cause impact erosion, acquire a heavy load of loose, fine-grained material, and then move the material down confining, steep-sided channels and deposit sediments on the alluvial fans. This type of deposition, with long, dry periods between rainstorms, creates unconsolidated deposits with an open structure of high porosity and low density.

Texture.—Detailed studies of the texture of the collapsing soils revealed voids between grains held in place by clay bonds, bubble cavities formed by air entrapment, interlaminar openings in thinly-laminated sediments, and voids left by disintegration of entrapped vegetation. Fig. 2 shows some typical mechanisms which hold grains together in low-density soils. The predominant clay mineral in all the subsiding fans is montmorillonite, which has a high, dry strength.

Reconaissance surveys of land subsidence in the San Joaquin Valley showed evidence that shallow subsidence might occur over several areas along the proposed alinement of the San Luis Canal. These areas were generally in the interfan regions between outwash streams and were considered to have been caused by the rapidly-deposited, low-density mudflows of fine-grained soils. Since the San Luis Canal was to be constructed through these areas, it was essential that the areas of shallow subsidence be delineated and the seriousness

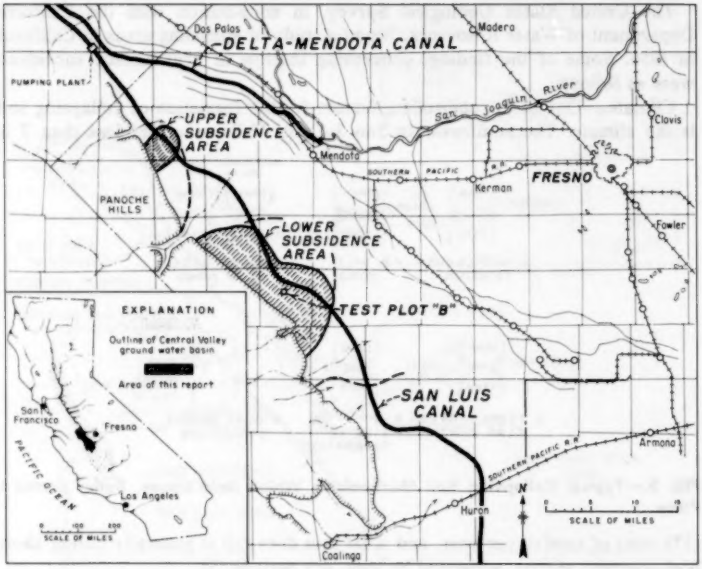

FIG. 3.—Problem Areas of Land Subsidence and Route of San Luis Canal Through These Areas

of the problem be evaluated so that pretreatment of the canal route could be accomplished prior to construction. Approx 20 miles (32 km) of the canal passed through soils which required extensive investigation to determine the potential for shallow subsidence (see Fig. 3). Because of the size and importance of the canal, limitations in settlement were of essential consideration for the maintenance of grade and the prevention of cracking in the linings and the embankments.

Previous extensive studies had been conducted in unirrigated areas where the near-surface subsidence problem was quite serious. Several ponding tests had been performed and some showed more than 10 ft (3 m) of near-surface subsidence as a result of wetting. Much of the route of the canal was to pass through areas where at least moderate, sprinkler-type irrigation supplied from

wells had already taken place. Therefore, the amount of subsidence in the irrigated areas was expected to be less than in the nonirrigated areas and of varying degrees of seriousness.

Detailed Soil Explorations

Because of the known susceptibility of subsidence upon wetting of the low-density materials along several areas of the route of the San Luis Canal, investigation procedures were used which would specifically identify the looseness of those soils. These field investigations were supplemented with laboratory tests on representative samples taken at frequent depth intervals. Finally, several field test ponds were installed to correlate the probable shallow subsidence with the varying degrees of seriousness shown by the exploration program and laboratory tests.

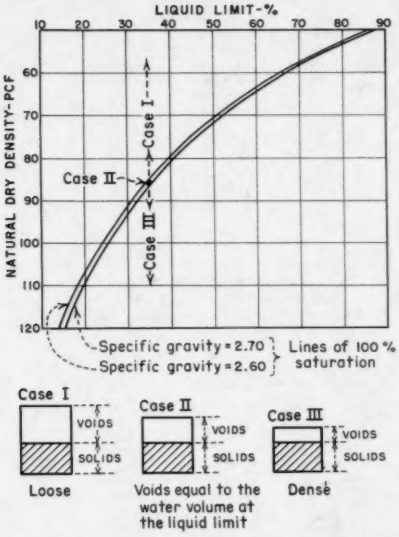

FIG. 4.—Criterion for Evaluating Looseness and Probability of Subsidence

A systematic, undisturbed soil-sampling program was conducted with drill holes 100 ft (30 m) deep, spaced at 1,000-ft (305-m) intervals along the canal alinement through the subsidence susceptible areas. Samples were taken at depth intervals of 5 ft (1.5 m) for the entire depth of the hole. Holes spaced at 1-mile (1.6-km) intervals wre extended to the groundwater table, which was generally near 200 ft (61 m) in depth. Undisturbed samples were obtained at 5-ft (1.5-m) intervals for the entire depth of these holes also. For the San Luis Canal investigation, thin-wall drive samplers were used and provided satisfactory undisturbed sample recovery. The method used was similar to that described in the American Society for Testing and Materials designation, i.e., D 1587-58T.

It was found necessary to prescribe that dry methods, such as air drilling, be used to advance the drill holes because water and drilling fluid would have affected the natural soil conditions.

Since different types of soil may be stable at quite different ranges of density,

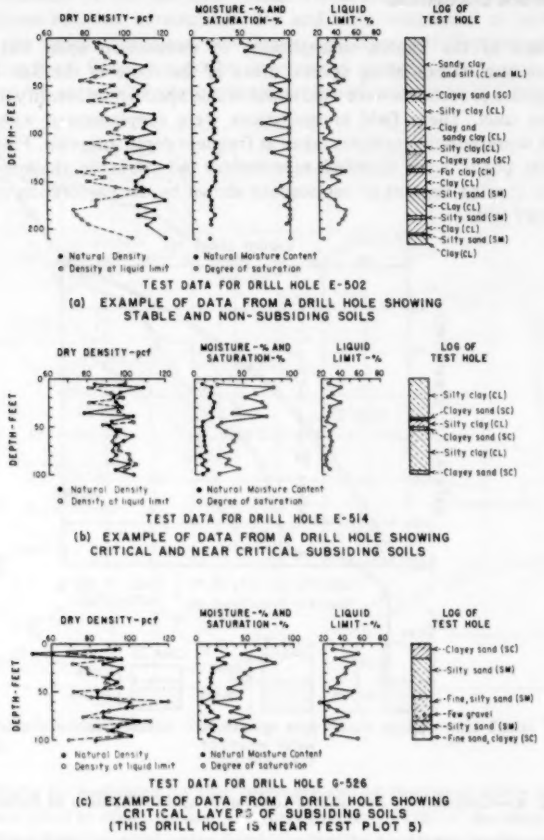

FIG. 5.—Typical Examples of Exploration Data

it was important to determine soil type and to study the characteristics of plasticity, water-holding capacity, and the effects of wetting in regard to overall canal subsidence.

Criteria for Evaluating Collapsible Soils

To explain and evaluate the critical condition for collapse, it was determined

that soil density was of highest importance because, for this type of subsidence to occur, the soils must be sufficiently loose so that they are capable of collapsing when their particle-to-particle bond is weakened by wetting. Soils of different types require different quantities of water to reduce them to a weak plastic condition. This suggests that a simple criterion can be used to indicate the limiting density at which any given soil will collapse upon wetting. Then, by the determination of in-place density, the soil can be evaluated as being loose and susceptible to subsidence, or sufficiently dense and unlikely to subside.

One of the criteria for analysis, making use of the natural in-place density and the standard liquid limit test, is slhown in Fig. 4 (3). Soils of different plasticity or water-holding capacity will collapse at different densities. The liquid limit is a moisture content, determined by standard laboratory tests, which represents the weakest plastic condition of the soil or the condition at which it is approaching the liquid state. When the soil has a low density such that its void space is just sufficiently large to hold the liquid limit moisture content (see Case II), saturation can easily cause a liquid limit consistency, at which state the soil offers little resistance to deformation. If voids are less than this amount, as shown by Case III, the soil at saturation will remain in the plastic state and have greater resistance against particle shifting and only settle as a normal result of loading. If the voids are greater than this amount, as shown by Case I, saturation would result in a moisture content in excess of the liquid limit and the potential for collapse would be high. If collapse did not occur, the soil would surely be in a very sensitive condition.

Using the aforementioned criterion of liquid limit and natural density, each drill hole was studied to determine if the natural densities were above or below this limiting density, based on the liquid limit moisture content for each sample tested. Although the soils must first be in a critically low-density condition for a collapse of structure to occur, the existing degree of saturation was also considered an important part of the analysis. Soils which were already at a high degree of saturation were expected to be minimally affected by additional wetting, whereas soils with low or moderate degrees of saturation (less than about 70%) were examined critically.

Fig. 5 shows example graphs of the detailed data studied for each drill hole. First, the natural density was compared to the limiting density based on the liquid limit. Then, the natural moisture content was examined to evaluate the existing degree of saturation. Finally, the results of these tests were compared to the descriptive log of the drill hole.

Practical Limitations to Interpreting Laboratory Test Data

The logs of the drill holes were quite important for establishing confidence in the laboratory test results, since there are practical limitations in the theoretical criteria. First, it is assumed that the soils are uncemented, and second, that they are sufficiently fine-grained so that the liquid limit test is applicable. To apply these criteria to cohesive soils containing gravel or coarse sands, consideration must be given to the fine soil fraction, because that is the portion to which the liquid limit test is applicable. Nonplastic sands are also questionable as to applicability of the criterion, unless they are fine enough so that the liquid limit can be determined. Observations have indicated that this criterion

is not applicable for soils with liquid limits less than about 20%.

There are also practical limitations regarding the accuracy of natural density determinations. It is assumed that a small sample represents the average overall surrounding mass density. If frequent changes in soil layering or deposition are present, then the natural density from relatively small samples may not

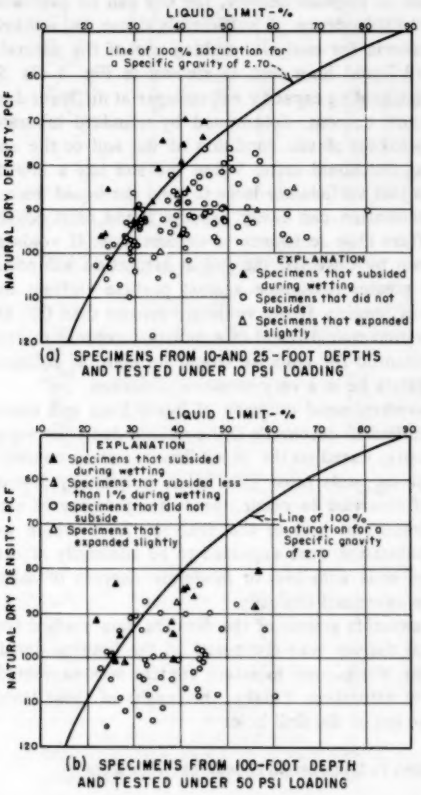

FIG. 6.—Behavior of Consolidation Test Specimens After Water Was Applied

be representative. Also in such soils, small samples selected for liquid limit and specific gravity tests may not be truly representative of the entire sample. Therefore, numerous tests at frequent depth intervals were made for the San Luis Canal investigations to establish confidence in average values. These factors were some of the principal causes of irregularities shown in some of the data, and general trends were established as the basis of major conclusions.

Laboratory Consolidation Tests

To establish trends for the effect of loading on subsidence, laboratory consolidation tests were performed on representative samples from four depths in each drill hole, generally at 10 ft, 25 ft, 50 ft, and 100 ft (3 m, 7.6 m, 15.2 m, and 30.5 m). The test loads were standardized so that samples from the 10-ft–25-ft (3-m–7.6-m), depths were tested under a loading of 10 lb/sq in. (69 kPa) to represent an approximate overburden pressure. For the same reason, the deeper samples to 50-ft (15.2-m) depth were tested under 25 lb/sq in. (172-kPa) pressures, and samples from 50-ft–100-ft (15.2-m–30.5-m) depth were tested under pressures of 50 lb/sq in. (345 kPa). These test specimens were trimmed from the 3-in. diam (76-mm), thin-wall undisturbed sample tubes. The load was applied to the specimen at natural moisture content, and settlement was recorded. At that time, some settlement was observed and considered to be largely that which would occur when any test specimen is reloaded, particularly those near critical moisture.

After final measurements were made under natural moisture conditions, the soil specimens were submerged and saturated without increasing the load. Any settlement taking place under this condition was considered to be collapse due to wetting. Many of the test specimens did not change in height, some showed further settlement due to wetting, and a few showed very slight expansion.

To compare the general results of these laboratory consolidation tests with the aforementioned liquid limit-natural density criterion, the settlement observed when water was added is indicated on the chart shown in Fig. 6. Charts such as this were prepared for samples from shallow depths, intermediate depths, and from the 100-ft depth tested under the loadings described previously.

These laboratory consolidation tests showed that the criterion of limiting density based on the liquid limit moisture content is quite logical for the near-surface soils where overburden pressures are small. At greater depths, such as 100 ft (30.5 m), these tests indicate that the limiting density should be considered to be about 10 lb/cu ft (160 kg/m^3) higher than that indicated by the liquid limit. Generally, it was found that soils most susceptible to collapse were found nearer the surface and that densities increased with increasing depth. Nevertheless, the criterion of limiting density based on the liquid limit is a very useful guide for assessing the looseness of the soil and its probability of subsiding upon initial wetting.

General Analyses of Test Results

Because the detailed characteristics of soils vary considerably over large areas, an overall examination of the soils along the canal alinement was made so that reaches of the canal to be treated would be kept to a minimum but would include those areas which were critical. Where minor looseness was found, only moderate treatment might be required and areas which were apparently stable would require no treatment. Using this approach, an attempt was made to determine for the San Luis Canal alinement areas that: (1) Were most critical; (2) had critical soils extending to considerable depth; (3) had only near-surface critical soils; and (4) were previously delineated as having subsiding soils but were found through investigation to be not critical but have normal properties.

Although each drill hole was analyzed in detail, it was found helpful to review all the results in a combined form. Fig. 7 shows the method used to summarize the data from an overall examination of results for an entire suspected subsidence area. The charts are arranged to contrast the two most important features: (1) Whether in-place density is above or below limiting density, based on the liquid limit; and (2) the degree of saturation of the soil at in-place water content. To emphasize the critical conditions with respect to probable subsidence, the areas shaded black are those where the in-place density is below the limiting density and the in-place degree of saturation is below 100%. Therefore, the

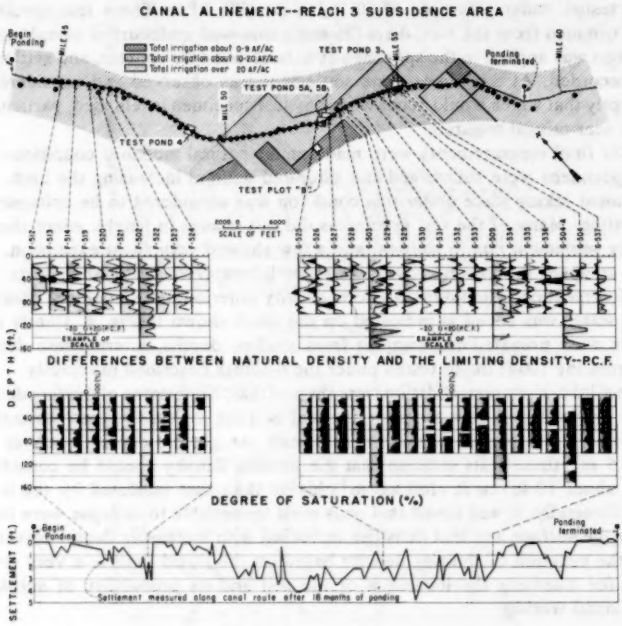

FIG. 7.—Settlement due to Ponding Compared to Pretreatment Investigations

greater the amount of black shading, the greater the likelihood of subsidence, and conversely, the greater the amount of gray shading, the better the soil conditions. The estimated amounts of past irrigation, as well as the locations of drill holes along the alinement are also shown in Fig. 7. Only one small portion of the alinement is shown on the figure for illustrative purposes. The group of 10 graphs on the left indicates that the soils from these holes would have very little subsidence potential. There is a prominence of gray area with very little black shading showing. Densities appear to be well above the limiting density based on the liquid limit. In some cases, the degree of saturation is low, but the density is correspondingly high so this area would be of little

concern. Soil conditions appear much more critical in the area shown on the right in Fig. 7. Black areas are much more prominent and only a few holes show high degrees of saturation.

It was observed that the most serious subsidence areas were generally located where the estimated amount of previous irrigation was small. Because irrigation

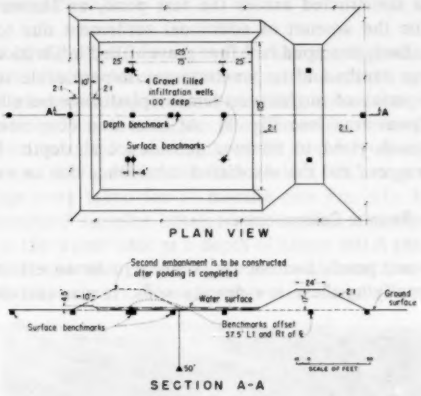

FIG. 8.—Plan and Section of Test Ponds

FIG. 9.—Ponding Test in Progress Showing Settling of Banks

records were often unreliable, the soil analyses were still the principal method of evaluating the seriousness of the problem.

Test Ponds

As mentioned previously, several field test ponds were constructed in areas where explorations had shown conditions most critical for subsidence due to

wetting. Data from these ponding tests were used to correlate with the exploration program and laboratory tests.

A diagram of a typical test pond is shown in Fig. 8. As can be seen in the figure, each test pond had an embankment constructed on one side to represent a typical canal embankment and to demonstrate the effects the embankment might have on subsidence. After the ponding tests were completed, another embankment was constructed across the test pond, as shown by the dashed lines, to determine the amount of additional settlement due to the weight of the embankment. Each test pond had four gravel-filled infiltration wells to assist in wetting at lower depths and to penetrate any impermeable soil layers. Each test pond had a series of surface settlement platforms installed, both inside and outside the pool area (see Fig. 8). At least one deep settlement marker was installed at each pond to monitor subsidence at depth. Fig. 9 shows a ponding test in progress and the associated subsidence due to wetting.

Ponding Treatment Prior to Construction

Data from the test ponds had shown ponding to be an effective method of collapsing and densifying these low-density soils. It was therefore determined

FIG. 10.—Ponding Operations to Consolidate Subsoils Prior to Construction of Canal Embankments

that ponding would be used prior to construction to densify the soils along the canal alinement, through the areas most susceptible to collapse.

Ponding (as shown in Fig. 10) performed along the canal alinement prior to construction caused subsidence of varying magnitude. Measurements or settlement devices spaced at 500-ft (152-m) intervals permitted a direct comparison with the investigation data. The aforementioned critical area subsided 4 ft and 5 ft (1.2 m and 1.5 m) in many places, as shown at the bottom of Fig. 7.

Ditchriders maintaining the dikes during the preconstruction ponding operation observed as much as 7 ft (2.1 m) of settlement under the low dikes in the critical areas. Stabilization by the ponding treatment of the loose subsoils down to the existing water table near a depth of 160 ft (49 m) was necessary, because

only variable amounts of water had been applied during perious irrigation operations. Collapsing of these loose soils was very effective in reducing the amount of differential foundation movement after the embankments were constructed and the canal was operating. A total of about 20 miles (32 km) of canal alinement was treated by ponding prior to construction.

Observation of Phreatic Surface

The movement of the phreatic surface from the ponding was observed using a commercially-available nuclear moisture meter for both the experimental plots and for those constructed during the actual ponding operations prior to construction (4). Casings in which the nuclear moisture meter was lowered to take measurements were installed to a depth of 50 ft (15.2 m) near test pond 3, at distances of about 30 ft, 50 ft, and 80 ft (9.1 m, 15.2 m, and 24.4 m) from the pond; readings were taken for 17 months (see Fig. 11). Holes were then drilled and undisturbed samples obtained to confirm that the subsoils were saturated down to the water table at a depth of about 160 ft (48.8 m).

Before the preconstruction ponds were filled with water, casings to receive the nuclear probe for moisture measurements were installed on 1-mile (1.6-km)

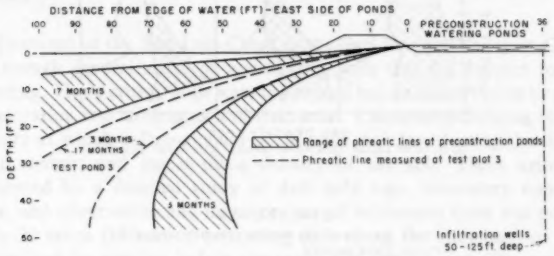

FIG. 11.—Movement of Phreatic Line with Time Traced with Nuclear Moisture Probe

centers along the right-of-way line on the east side of the canal about 100 ft (30.5 m) from the ponds. Readings were taken after 3 months, 10 months, and 17 months of ponding.

To take full advantage of the preconstruction ponding operations, water was applied to the subsoils until the upper portion of the phreatic surface had stabilized or a near steady-state flow condition had been reached at the sides of the ponds. In the areas where the phreatic surface rose rapidly, ponding was terminated in as little as 1 yr, because the water table was approaching canal-bottom grade and no significant settlement was being observed.

A comparison of the phreatic lines after 3 months and 17 months of ponding at test plot 3 and several locations along the preconstruction watering ponds is shown in Fig. 11.

Designs and Construction Considerations

The San Luis Canal embraced more extensive and greater varieties of problems than other portions of the aqueduct and other canals in the area. It has a

greater water depth, as much as 33 ft (10 m), and required considerable freeboard to account for future deep subsidence of the valley. Slope heights of as much as 40 ft (12.2 m) for fills and 50 ft (15.2 m) for cuts were required. In reach 1, expansive soils were encountered, and in reach 3, collapsing soils. It was anticipated that conventional slopes of 1-1/2:1, that were used elsewhere, were too steep for these problem soils. Therefore, flatter slopes of 2 or 2-1/2:1 were considered necessary and slope stability analyses were performed using these slopes (4). The San Luis Canal is located in a seismically-active area and this was also considered in the slope stability analyses. The canal was eventually constructed using 2:1 side slopes.

For construction in the collapsible soil area where the subsoils were subjected to preponding, special consideration was given to the probability of a soft, saturated condition of the canal foundation. After ponding was terminated, a drainage period of several months was permitted to allow the initial collapse to be as complete as possible and to extend the effect to soil at greater depth. Also, these wet soils had to dry somewhat to permit workable conditions for the contractor's equipment.

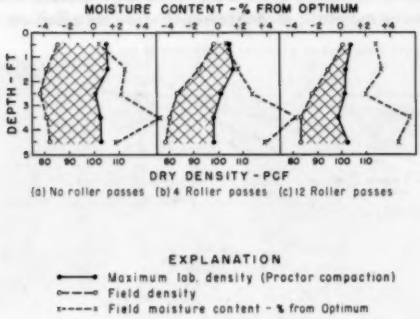

FIG. 12.—Generalized Results from Test Section Using 50-Ton Pneumatic-Tired Roller

The ponding was not expected to consolidate the natural material beyond that of initial collapse. Therefore, to provide a firmer subbase to support the concrete lining, specifications called for rolling the bottom of the canal and the embankment foundations with eight passes of a 50-ton (445-kN), pneumatic-tired roller. At a test area, the effects of this consolidation were investigated by sampling before and after rolling to determine changes in density. It was found that some increase in density occurred as deep as 3 ft (1 m), but that most densification took place in the upper 1-1/2 ft (0.5 m) (see Fig. 12). Rolling of the canal side slopes was also considered desirable, but no feasible method was developed for accomplishing it. Since experimental data showed that embankments would continue to settle after they were built, specifications required a six-month period for stabilization after construction was complete before concrete lining was placed on them. In areas not considered sufficiently critical to warrant preponding, sprinkling was required to wet the foundation soils enough for settlement development in preparation for embankment construction.

Performance of San Luis Canal

The mudflow deposits through which the canal was constructed have soils of variable plasticity and in-place density. Thin, impervious layers are not uncommon. These prevent flooding and sprinkling methods (which collapse the soils) from being effective unless unfiltration wells are installed. The northern 4 miles (6.4 km) of the subsidence area were ponded without wells for more than 1 yr. One bridge site has since settled more than 3 ft (1 m), because of an extensive impervious clay layer at a depth of 25 ft (7.6 m) which prevented subsoil saturation (2). This is considered a minor problem in relation to the magnitude of the overall conditions encountered and the performance of the canal has been excellent. Because of continuing regional deep subsidence due to groundwater overdraft, the magnitude of post-construction near-surface settlement has not been monitored in the critical subsidence areas. However, no structural damage of the canal has been observed which could be attributed to further hydrocompaction of the near surface soils. The San Luis Canal was constructed during 1963–1968 and, as a result of the extensive soil investigations and preconstruction treatment of foundation soils, has performed quite well.

Conclusions

The alinement of the San Luis Canal in the San Joaquin Valley in California, passes through several areas of low-density soils that are subject to collapse upon wetting. These critical soils were delineated before construction by extensive field exploration and laboratory and field tests. Criteria for defining the limiting soil density at which collapse could occur were developed using the liquid limit moisture content and the in-place density of the soil. These criteria were supplemented by a detailed study of drill hole logs, laboratory consolidation test data, and observation and measurement of settlement from test ponds.

Nearly 20 miles (32 km) of collapsing soils along the alinement of the canal were stabilized by ponding before the canal was constructed. The surface soils were generally saturated down to the water table which was at a depth of about 160 ft (48.8 m). Further densification of the foundation soils was accomplished during construction by requiring eight passes of a 50-ton (445-kN), pneumatic-tired roller on the canal invert and on the foundations for canal embankments.

Preponding the collapsible soils was an effective method of stabilization. The canal was built during 1963–1968 and has performed quite well to date (1979).

Appendix.—References

1. Bara, J. P., "Precollapsing Foundation Soils by Wetting," *Proceedings of the 5th Pan-American Conference on Soil Mechanics and Foundation Engineering*, Nov., 1975.
2. Bara, J. P., "Research on Wetting Collapsible Foundation Soils," *Report No. GR-14-77*, Bureau of Reclamation, Denver, Colo., Sept., 1977.
3. Gibbs, H. J., and Bara, J. P., "Predicting Surface Subsidence from Basic Soil Tests," *Report No. EM-658*, Bureau of Reclamation, Denver, Colo., June, 1962.
4. Gibbs, H. J., and Bara, J. P., *Stability Problems of Collapsing Soil*, Bureau of Reclamation, Denver, Colo., Aug., 1966.
5. Lofgren, B. E., *Land Subsidence Due to the Application of Water*, The Geological Society of America, Inc., Boulder, Colo., 1969.

6. Lucas, C. V., and Lombard, F. J., "Land Subsidence Along the California Aqueduct as Related to Environment," presented at the May, 1964, ASCE, Environmental Engineering Conference, held at Salt Lake City, Utah.
7. Poland, J. F., "Land Subsidence in Western United States," presented at the May, 1969, Geologic Hazards and Public Problems Conference, held at Santa Rosa, Calif.

JOURNAL OF THE GEOTECHNICAL ENGINEERING DIVISION

COMPUTER SIMULATION OF CREEP OF CLAY

By Roland Pusch[1] and Paul Feltham[2]

INTRODUCTION

Creep of clay under undrained conditions may be of considerable importance in practice, as illustrated by time-dependent settlement of foundations on overconsolidated clay, and "depth creep" in slopes excavated in low-permeability, homogeneous clay strata.

Applied soil mechanics still makes use of empirical laws for the prediction of creep strain since no generally accepted creep theory is yet available. The object of this paper is to present an improved, physical creep model and its mathematical analogy, and to examine the creep rate according to this model by means of a computer code. The model yields a creep law which appears to have a wide scope and it thus provides a promising basis for representing creep data, and a rational starting point for creep studies which involve structural changes.

EVOLUTION OF THE CREEP

Natural, soft, illitic clays consist of rather dense and rigid aggregates [Fig. 1(*a*)] which support each other, or are connected by links or bridges of small particles (2). Most of these are associated edge-to-edge or edge-to-face with direct mineral/mineral contacts, or separated by one or a few water molecule layers. The variable character of the contacts implies a spectrum of bond strengths, probably with a preponderance of strong bonds. When a sufficiently high external shear stress is applied, the induced internal stresses will shear the weaker, interlinking particle groups, transforming them to "domains" with the particles associated face-to-face [Fig. 1(*b*)].

[1]Prof., Div. Soil Mech., Univ. of Luleå, 95187 Lulia, Sweden.
[2]Prof., Dept. of Physics, Brunel Univ., Middlesex, England.

Note.—Discussion open until June 1, 1981. To extend the closing date one month, a written request must be filed with the Manager of Technical and Professional Publications, ASCE. Manuscript was submitted for review for possible publication on May 5, 1980. This paper is part of the Journal of the Geotechnical Engineering Division, Proceedings of the American Society of Civil Engineers, © ASCE, Vol. 107, No. GT1, January, 1981. ISSN 0093-6405/81/0001-0095/$01.00.

The interparticle distance in the domains tends towards an equilibrium value in the stress field as determined by the local mechanical stress, the interparticle atomic and molecular attraction, and the repulsion resulting from hydration at small interparticle distances, or from electrical double-layers at larger distances. Some domains may gain strength from the successive formation of interconnecting layers of clay-adsorbed water, but also "aged" domains remain the weakest structural members of the clay. Displacements in the particle network in the course of creep may therefore be favored at these locations. Such comparatively weak microvolumes may be considered as sustaining substantial deformation and thus as main slip units in the evolution of creep, their deformations and

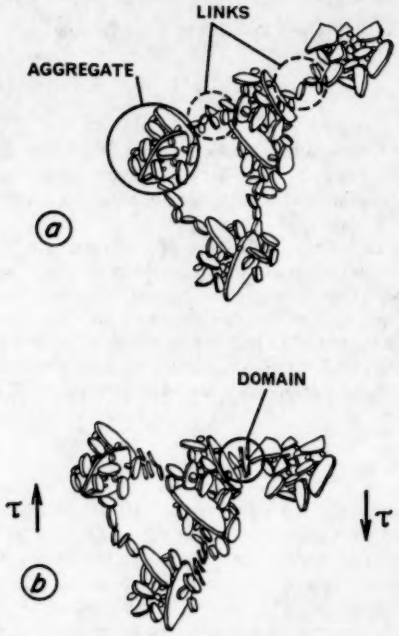

FIG. 1.—Formation of Domains: (*a*) Natural, Undisturbed Condition; (*b*) Local Overstressing Resulting in Domains

displacements, at least partly, resulting from water molecule interactions in the form of breakage and reformation of hydrogen bonds (3).

The weakness of the domains facilitates a relatively rapid initial deformation at the onset of creep which, however, becomes progressively retarded by several mechanisms. Firstly, movements of the domains will be such that strong aggregates and big grains will approach one another, make contact and strengthen the structure through mechanical interlocking. Secondly, strength may be gained through the reformation of water "lattices" and the formation of new interlinking particle groups. Such "thixotropic" healing will be favored when the relative

sliding of adjacent aggregates or grains has ceased, either because of interlocking or because they are temporarily not subjected to strain-inducing local stresses. Thirdly, the displacements may lead to the formation of new domains through the yielding of bridging links which become "overstressed." If the stress level is sufficiently high, such structural damage will accumulate and bulk failure will eventually take place.

Creep Theory

The heterogeneity in stress and structure on the microscale will jointly result in a distribution of heights of the energy barriers. The structural changes imply that the energy spectrum will vary in the course of the creep. Thermal activation is assumed, for the creep of soils is known to be significantly temperature dependent. This suggests that, as in other materials where the creep is known to result from thermally activated glide, it is governed by a stress-dependent and time-dependent spectrum of energy barriers, which control the unit slip events on the molecular scale. These features have been embodied in a recent model of the creep of soils (4). In practice, the equations obtained may not be amenable to easy analytical treatment, particularly if one wishes to examine the influence of the energy-barrier distribution at the onset of the creep on the time dependence of the creep rate. A simple computer model has therefore been devised (1), and its application to the creep of clay is here examined in the specific case when the initial distribution of energy barriers is "flat," i.e., it is constant in a given barrier-height range, and zero outside it.

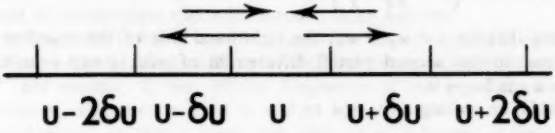

FIG. 2.—Segments of Activation Energy Range

A basic assumption is that the dwell time, θ, of a slip unit at a barrier of effective height, u, is given by the Arrhenius rate equation

$$\theta(u) = \frac{1}{\nu_D} \exp\left(\frac{u}{kT}\right) \quad \ldots\ldots\ldots\ldots\ldots\ldots\ldots\ldots\ldots\ldots\ldots\ldots\ldots\ldots (1)$$

in which u = the barrier height; ν_D = an atomic vibrational frequency of the order of 10^{12}/sec; k = Boltzmann's constant; and T = the temperature, in degrees Kelvin.

At any given temperature only a limited energy spectrum

$$u_1 \leq u \leq u_2 \quad \ldots\ldots\ldots\ldots\ldots\ldots\ldots\ldots\ldots\ldots\ldots\ldots\ldots\ldots\ldots\ldots\ldots\ldots (2)$$

will be of relevance, for with $u < u_1$ the dwell-times will be too short, and for $u > u_2$ too long, to be "observable" during the periods over which creep tests generally extend in practice (4).

If slip has been activated at a certain point in the clay, i.e., a barrier has been overcome, a contribution to the overall shear is made by the associated

extension of the local slip-patch. In the model it is assumed that the next barrier to be encountered by the same spreading slip-zone will be either higher or lower by an average amount δu. Concerning the form of the spectrum, i.e., the number $n(u,t)\delta u$ of potential slip units per unit volume of material held up at time t at barriers of height u, the spectrum is considered to be subdivided into equal intervals δu. Now referring to Fig. 2, which shows consecutive activation energy intervals, the time rate of change of the number $n(u,t)\delta u$ of flow units in the u-interval, i.e., $(\partial n/\partial t)\delta u$, is seen to be determined on the one hand, by the outflow from the u-level into the higher energy-interval $(1/2)\, n(u,t)\delta u\, v_D \exp(-u/kT)$ and, it is assumed, of the same number into the lower one, indicated respectively by the right and left lower arrows. Similarly, the simultaneous influx is

$$\frac{1}{2} n(u-\delta u,t)\delta u\, v_D \exp\left(-\frac{u-\delta u}{kT}\right)$$

$$+\frac{1}{2} n(u+\delta u,t)\delta u\, D \exp\left(-\frac{u+\delta u}{kT}\right)$$

If all the separate contributions are added, one obtains

$$\frac{\partial n}{\partial t} = \frac{1}{2} v_D \left[n(u+\delta u,t) \exp\left(-\frac{u+\delta u}{kT}\right) - 2n(u,t) \exp\left(-\frac{u}{kT}\right) \right.$$

$$\left. + n(u-\delta u,t) \exp\left(-\frac{u-\delta u}{kT}\right)\right]$$

Assuming that $\delta u << u_2 - u_1$, the right-hand side of the equation can be seen to tend to the second partial differential of $n(u,t)\exp(-u/kT)$ with respect to u, as $\delta u \to 0$.

This yields, on writing n for $n(u,t)$

$$\frac{\partial n}{\partial t} = D \frac{\partial^2 \left[n \exp\left(-\frac{u}{kT}\right)\right]}{\partial u^2}, \quad D = \frac{1}{2} v_D (\delta u)^2 \quad \ldots\ldots\ldots\ldots\ldots (3)$$

If each activated jump is taken to make the same, mean, contribution A^* to the shear strain, γ, of the specimen, then the creep rate in shear will be

$$\dot{\gamma} = A^* \int_{u_1}^{u_2} v(u)\, n(u,t)\, du = A^* v_D \int_{u_1}^{u_2} n(u,t) \exp\left(-\frac{u}{kT}\right) du \quad \ldots\ldots (4)$$

We note that the range of u-values terminates at u_1 at the low u end, while u_2 represents the upper limit of the operative spectrum. In the integration it is assumed that the scheme of jumps shown in Fig. 2 is preserved at both ends of the cascade; thus u_1 is regarded as a "generating barrier," the formation of new slip units being favored in regions where the activation energies for slip are low. These new units are taken as providing the otherwise absent net inflow to the u_1-level from $u_1 - \delta u$. Again, jumps over barriers higher than u_2 will occur with such a low frequency that their contribution to the creep over the period of observation may be neglected. One may regard u_2 as an

"absorbing barrier." These considerations lead to the result (4) that the most probable value of u in the spectrum will be equal to about 25 kT, i.e., about 0.6 eV at room temperature.

A solution of Eq. 3 which leads to creep laws generally observed in solids at relatively low temperatures (4) is

$$n(u,t) \propto g\, e^{-q} \quad \ldots\ldots\ldots\ldots\ldots\ldots\ldots\ldots\ldots\ldots\ldots\ldots\ldots\ldots\ldots\ldots (5)$$

in which $$q = \frac{\exp\left(\frac{u}{kT}\right)}{\nu_D(t + t_o)} \quad \ldots\ldots\ldots\ldots\ldots\ldots\ldots\ldots\ldots\ldots\ldots\ldots\ldots\ldots\ldots\ldots (6)$$

and t_o = a constant of integration. Upon substitution into Eq. 4, one obtains a relation which is practically indistinguishable from the simple form

$$\dot{\gamma} \propto \frac{1}{t + t_o} \quad \ldots\ldots\ldots\ldots\ldots\ldots\ldots\ldots\ldots\ldots\ldots\ldots\ldots\ldots\ldots\ldots (7)$$

in which the appropriate constant of proportionality depends on the deviator stress, the temperature, and on structural details.

Computation of Creep Rate

The evolution of creep according to this creep model is here examined by means of a computer code (1) for numerical integration of the equations governing the thermal activation, using discrete energy intervals in the thermally activated movement of independent slip units across energy barriers.

Code.—The code is based on the assumption that the probability that a slip unit will have a kinetic energy sufficiently high to overcome a barrier encountered, is $e^{-u/kT}$ per attempt. If the attempt frequency of the slip units is ν_D, then the number of encounters in time Δt will be $\nu_D \Delta t$.

The probability, p, that a given unit held up at a barrier at time t, is still held up by the barrier at time $t + \Delta t$ is therefore

$$p = (1 - e^{-u/kT})^{\nu_D \Delta t} \quad \ldots\ldots\ldots\ldots\ldots\ldots\ldots\ldots\ldots\ldots\ldots\ldots\ldots\ldots\ldots\ldots (8)$$

If a large number of independent slip units are contained in independent potential wells of depth u, the fraction, f, which has crossed over during the interval Δt is

$$f = 1 - p = 1 - (1 - e^{-u/kT})^{\nu_D \Delta t} \quad \ldots\ldots\ldots\ldots\ldots\ldots\ldots\ldots\ldots\ldots\ldots\ldots\ldots\ldots\ldots\ldots (9)$$

We assume that the range of barrier heights $u_2 - u_1$ increases from u_1 by equal steps δu to u_2. With a total of N steps we therefore have $\delta u = (u_2 - u_1)/(N - 1)$. Activated jumps will be assumed to take a given slip unit, held up at a barrier of height u, with equal probability (1/2) to a barrier of height $u + \delta u$ or $u - \delta u$. This single-step process characterizes the numerical-integration scheme which yields the distribution law, $n(u,t)$, for the barrier heights. In the present work we shall assume that $n(u,0) = \text{const}$ for all u-values in the range. This boundary condition will underestimate the n-population for low u-values compared with the distribution given by Eq. 5, as is readily inferred on considering $n(u,0)$ in both cases.

The numerical integration scheme for the model corresponding to the cascade used in the derivation of Eq. 3 in the foregoing, is as follows

$$p_i(t + \Delta t) = p_i(t) - f_i p_i(t) + \frac{1}{2} f_{i+1} p_{i+1}(t) + \frac{1}{2} f_{i-1} p_{i-1}(t) \quad \ldots\ldots\ldots \quad (10)$$

We now take

$$p_1(t + \Delta t) = p_1(t) - f_1 p_1(t) + \frac{1}{2} f_2 p_2(t) \quad \ldots\ldots\ldots\ldots\ldots\ldots \quad (11)$$

assuming in the present instance that there is no net influx from outside the range, i.e., from p_o. This implies that no slip units are generated at weak spots (low u). Furthermore

$$p_2(t + \Delta t) = p_2(t) - f_2 p_2(t) + \frac{1}{2} f_3 p_3(t) + f_1 p_1(t) \quad \ldots\ldots\ldots\ldots \quad (12)$$

and similarly, for $2 < i < N - 1$

$$P_{N-1}(t + \Delta t) = p_{N-1}(t) - f_{N-1} p_{N-1}(t) + \frac{1}{2} f_{N-2} p_{N-2}(t) + f_N p_N(t) \quad (13)$$

Finally

$$P_N(t + \Delta t) = p_N(t) - f_N p_N(t) + \frac{1}{2} f_{N-1} p_{N-1}(t) \quad \ldots\ldots\ldots\ldots \quad (14)$$

and again, there is no influx $(1/2) f_{N+1} p_{N+1}(t)$ from u-levels beyond u_2. This boundary condition will be unimportant in practice, for u_2 will be chosen to imply dwell times long compared with the period over which the creep is being considered.

The model requires the following as input:

Parameter	Restrictions
NEB: Number of energy barrier heights	$0 < \text{NEB} \leq 20$
DT: Time step for integration, in seconds	$0 < \text{DT} < \infty$
TNDS: Total number of slip units	$0 < \text{TNDS} < \infty$
TMAX: Duration of creep, in seconds	$0 < T_{\max} < \infty$
TPRINT: Time step for printing results	DT < TPRINT < TMAX
u_1 = Minimum energy, in electron volts	$0 < u_1 < \infty$
u_2 = Maximum energy, in electron volts	$0 < u_2 < \infty$
TEMP: Temperature, T, in degrees Celsius	$0 < \text{TEMP} < \infty$
BC: Boltzmanns's constant, k	eV/K
FREQ: Attempt frequency, ν_D, per second	$0 < \text{FREQ} < \infty$

Application

As we were interested principally in the shape of the creep curve it was possible to choose the values of all parameters appearing only in the constant

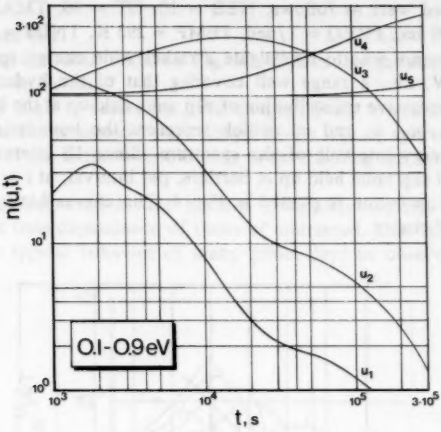

FIG. 3.—Successive Redistribution of Barrier Heights per δu Interval of Energy Spectrum in Course of Creep (0.1 eV–0.9 eV)

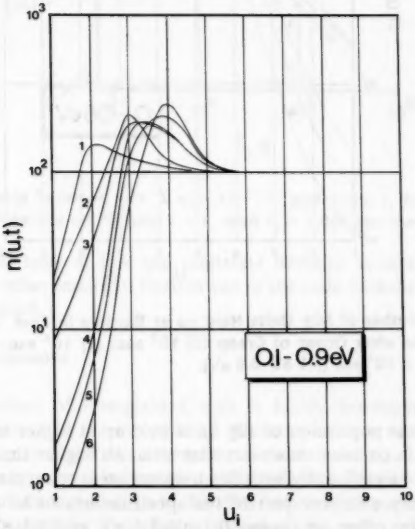

FIG. 4.—Total Number of Slip Units Held up at Spectrum Intervals at Different Times after Onset of Creep: (1) 10^3 sec; (2) 5×10^3 sec; (3) 10^4 sec; (4) 5×10^4 sec; (5) 10^5 sec; (6) 2×10^6 sec (0.1 eV–0.9 eV)

of proportionality (e.g., see Eq. 7) arbitrarily, for convenience in computing. The values used were as follows: NEB = 10, DT = 10, TMAX = $3 \cdot 10^5$ sec, TPRINT = 100 sec, FREQ = 1/sec, TEMP = 293 K, TNDS = 1,000.

The first attempt was to investigate a rather wide energy spectrum: 0.1 eV $\leq u \leq$ 0.9 eV, i.e., a range well covering that of the hydrogen bond. Fig. 3 shows the successive redistribution of slip units held up at the lowest boundary u_1, and at u_2, u_3, u_4 and u_5, which represent the boundaries between the lower four energy intervals of the spectrum. Since 10 intervals were taken, there were 100 slip units held up at barriers, per interval, at $t = 0$.

The net redistribution is plotted in Fig. 4. The curves have been smoothed for the sake of clarity.

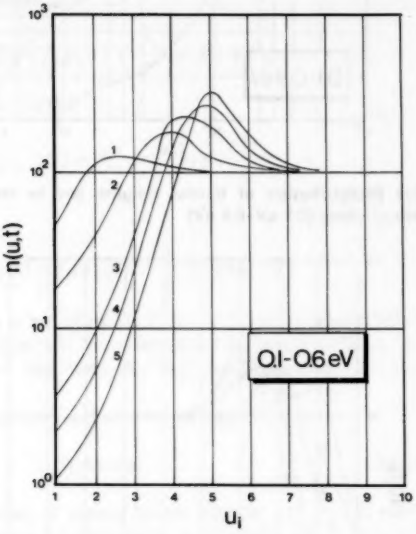

FIG. 5.—Total Number of Slip Units Held up at Barriers in Each Spectrum Interval at Different Times after Onset of Creep (1) 10^3 sec; (2) 10^4 sec; (3) 5×10^4 sec; (4) 10^5 sec; (5) 2×10^5 sec (0.1 eV–0.6 eV)

As expected, the population of slip units held up at higher barriers increased successively. It is obvious, however, that intervals higher than 0.6 eV–0.7 eV do not participate significantly with this u-spectrum at room temperature, which indicates that only a narrow part of the spectrum has to be considered. This was confirmed by other runs using 0.1 eV–1.5 eV and 0.1 eV–0.6 eV spans, the latter being shown by Fig. 5.

As to the creep rate, it is assumed in the theory that every jump makes the same contribution to the strain. The creep rate is thus obtained from the computed values of $n(u,t)$, (Figs. 3, 4 and 5) using the relation

$$\dot{\gamma} \propto \sum_i n(u_i,t)e^{-u_i/kT} \quad \ldots\ldots\ldots\ldots\ldots\ldots\ldots\ldots\ldots\ldots\ldots\ldots \quad (15)$$

for various values of t.

Fig. 6, showing the result based on Fig. 5, indicates that the computed relation is of the type given by Eq. 7.

The relatively high t_o-value, i.e., the comparatively low initial creep rate, and results from the assumed "flat" shape of the $n(u,o)$ spectrum, points to the importance of the initial u-distribution in determining the form of the early stages of creep.

The simple model used in the present computation yields creep curves representing the time-dependence of those of undrained, soft, illitic clay. They also reflect the typical behavior of many illitic clays as observed in uniaxial

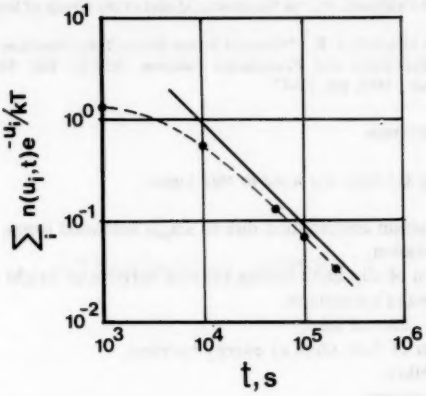

FIG. 6.—Relationship between $\dot{\gamma} \propto \Sigma\, n(u_i,t)e^{-u_i/kT}$ and time, t, for 0.1 eV–0.6 eV (Straight Line is Obtained on Plotting $t + t_o$ with t_o = 7,000 sec instead of t)

as well as triaxial tests at low and moderate deviator stresses, for which t_o is in many cases rather small (5). Further use of the code with different boundary conditions is planned.

Summary and Conclusions

The microstructure of fine-grained soils is highly heterogeneous, implying large spatial variation in the strength of the more or less continuous particle network. In creep induced by a constant deviatoric stress, the number and heights of thermally activable barriers to slip will thus vary in space and time. The resulting evolutionary change in the distribution of the spectrum of barrier heights is encompassed by a stochastic model of the creep of clay previously described by the writers. A simple version of this model was used in a computer simulation to determine the form of the creep curve at constant stress and temperature. The dependence of the strain on time was found to be approximately logarithmic, in good agreement with experiments. The use of various boundary

conditions, particularly defining the barrier spectrum at the onset of creep, should facilitate the diagnostic use of the computer program in studies of the deformation of clays.

Appendix I.—References

1. Miles, G., and Felthamn, P., "DENEB—A Computer Code for Numerical Integration of the Equations Governing the Thermal Activation of Discrete, Independent, Dislocation Segments Across Energy Barriers," Internal Report, Brunel University, Middlesex, England.
2. Pusch, R., "Clay Microstructure," *Document D:8*, National Swedish Building Research Council, Stockholm, Sweden, 1970.
3. Pusch, R., "Creep Evolution in Non-Cemented, Soft, Illitic Clays at Constant, Low or Intermediate Stresses," in press.
4. Pusch, R., and Felthamn, P., "A Stochastic Model of the Creep of Soils," *Géotechnique*, Sept., 1980.
5. Singh, A., and Mitchell, J. K., "General Stress-Strain-Time Function for Soils," *Journal of the Soil Mechanics and Foundation Division*, ASCE, Vol. 94, No. SM1, Proc. Paper 5728, Jan., 1968, pp. 21–47.

Appendix II.—Notation

The following symbols are used in this paper:

A^* = shear strain contribution due to single activated jump;
D = abbreviation;
f = fraction of slip units having crossed barriers of height u;
k = Boltzmann's constant;
N = energy interval step;
n = number of flow units or energy barriers;
p = probability;
q = abbreviation;
T = temperature;
t = time;
t_o = constant;
u = energy barrier height;
γ = shear strain;
$\dot{\gamma}$ = shear strain (creep) rate;
Δt = time interval;
δu = energy spectrum interval;
θ = dwell time of slip unit;
ν = slip frequency; and
ν_D = atomic vibrational frequency.

JOURNAL OF THE GEOTECHNICAL ENGINEERING DIVISION

TECHNICAL NOTES

Note.—Discussion open until June 1, 1981. To extend the closing date one month, a written request must be filed with the Manager of Technical and Professional Publications, ASCE. This paper is part of the Journal of the Geotechnical Engineering Division, Proceedings of the American Society of Civil Engineers, © ASCE, Vol. 107, No. GT1, January, 1981.

Technical Notes

To provide a place within ASCE for publication of technical ideas that have not advanced, as yet, to the point where they warrant publication as a Proceedings paper in a *Journal*, the publication of Technical Notes was authorized by the Board of Direction on October 16–18, 1967, under the following guidelines:

1. An original manuscript and two copies are to be submitted to the Manager of Technical and Professional Publications, ASCE, 345 East 47th Street, New York, N.Y., 10017, along with a request by the author that it be considered as a Technical Note.
2. The two copies will be sent to an appropriate Technical Division or Council for review.
3. If the Division or Council approves the contribution for publication, it shall be returned to Society Headquarters with appropriate comments.
4. The technical publications staff will prepare the material for use in the earliest possible issue of the *Journal*, after proper coordination with the author.
5. Each Technical Note is not to exceed 4 pages in the *Journal*. As an approximation, each full manuscript page of text, tables, or figures is the equivalent of one-half a *Journal* page.
6. The Technical Notes will be grouped in a special section of each *Journal*.
7. Information retrieval abstracts and key words will be unnecessary for Technical Notes.
8. The final date on which a Discussion should reach the Society is given as a footnote with each Technical Note.
9. Technical Notes will not be included in *Transactions*.
10. Technical Notes will be included in ASCE's annual and cumulative subject and author indexes.

The manuscripts for Technical Notes must meet the following requirements:

1. Titles must have a length not exceeding 50 characters and spaces.
2. The author's full name, Society membership grade, and a footnote reference stating present employment must appear on the first page of the manuscript. Authors need not be Society members.
3. The manuscript is to be submitted as an original copy (with two duplicates) that is typed double-spaced on one side of 8-1/2-in. (220-mm) by 11-in. (280-mm) white bond paper.
4. All mathematics must be typewritten and special symbols must be properly identified. The letter symbols used must be defined where they first appear, in figures or text, and arranged alphabetically in an Appendix.—Notation.
5. Standard definitions and symbols must be used. Reference must be made to the lists published by the American National Standards Institute and to the *Authors' Guide to the Publications of ASCE*.
6. Tables must be typed double-spaced (an original ribbon copy and two duplicate copies) on one side of 8-1/2-in. (220-mm) by 11-in. (280-mm) paper. An explanation of each table must appear in the text.
7. Figures must be drawn in black ink on one side of 8-1/2-in. (220-mm) by 11-in. (280-mm) paper. Because figures will be reproduced with a width of between 3 in. (76 mm) to 4-1/2 in. (110 mm), the lettering must be large enough to be legible at this width. Photographs must be submitted as glossy prints. Explanations and descriptions must be made within the text for each figure.
8. References cited in text must be typed at the end of the Technical Note in alphabetical order in an Appendix.—References.
9. Dual units, i.e., U.S. Customary followed by SI (International System) units in parentheses, should be used throughout the paper.

STRESSES IN SOIL AROUND VERTICAL COMPRESSIBLE PILES

By K. S. Sankaran,[1] N. R. Krishnaswamy,[2] and B. K. Sharas Chandra[3]

An attempt has been made to evaluate the stresses by obtaining the side shear distribution using linear elastic theory as suggested by Mattes and Poulos (3). The influence of the compressibility and L/d ratio of the pile on the stress distribution have been studied for $\mu = 0.5$, to show the difference between a very flexible and a rigid pile. The side shear distribution thus obtained for a particular ratio of L/d and compressibility of the pile is divided into uniform and linear variations (1), and is finally summed up, to get the net stresses. This is a step-by-step procedure, and the double integration of the Mindlin's equation (4) involved is solved partly analytically and partly numerically in a computer, using Gauss Quadrature formulas. The analysis is confined to vertical stress, although other stresses could be evaluated by the same technique.

The analysis is more realistic than the earlier methods (1,2) for the following reasons: (1) There is no assumption regarding the side shear distribution; (2) the length to diameter ratio of the pile is taken into account; (3) the compressibility of the pile, expressed by the stiffness factor, λ (ratio of Young's modulus of the pile, E_p, to the Young's modulus of soil, E_s), for a solid pile, is taken into account; and (4) further, the stress at the tip of the pile can be evaluated. The assumptions made in the analysis are: (1) The pile base is assumed to be a smooth disc, across which the base load is uniformly distributed; and (2) the disturbance of the continuity of the elastic halfspace due to the presence of the pile is ignored.

The table of stress coefficients is presented to cover a range of stiffness factors representing a highly flexible to a very rigid pile. In tables 1–4, the stresses can be interpolated for any intermediate flexibility of the pile. The tables are presented for selected ratios of m (ratio of depth to the length of the pile, z/L) and n (ratio of radial distance to the length of the pile, r/L). The L/d ratio and stiffness factor are varied from 10–100, and 50–50,000, respectively, assuming $\mu = 0.5$.

[1]Prof., Dept. of Civ. Engrg., Indian Inst. of Tech., Madras, 600 036, India.
[2]Asst. Prof., Dept. of Civ. Engrg., Indian Inst. of Tech., Madras, 600 036, India.
[3]Research Scholar, Dept. of Civ. Engrg., Indian Inst. of Tech., Madras, 600 036, India.

Note.—Discussion open until June 1, 1981. To extend the closing date one month, a written request must be filed with the Manager of Technical and Professional Publications, ASCE. Manuscript was submitted for review for possible publication on March 11, 1980. This paper is part of the Journal of the Geotechnical Engineering Division, Proceedings of the American Society of Civil Engineers, © ASCE, Vol. 107, No. GT1, January, 1981. ISSN 0093-6405/81/0001-0107/$01.00.

TABLE 1.—Vertical Stress Coefficients (× 1,000) for $L/d = 10$ (+ Tension, Otherwise Compression)

	n												
m	0.0	0.05	0.075	0.1	0.15	0.2	0.3	0.4	0.5	0.75	1.0	1.5	2.0
(1)	(2)	(3)	(4)	(5)	(6)	(7)	(8)	(9)	(10)	(11)	(12)	(13)	(14)
0.2		2,373	1,855	1,435	863	519	200	91	49	17	7	1	—
		538	523	474	365	270	153	97	66	28	12	2	—
		164	262	283	271	225	144	97	69	30	13	2	—
		260	319	325	285	229	144	97	69	30	13	2	—
0.4		1,316	1,105	948	717	551	331	203	128	46	18	3	1
		182	226	257	283	283	246	195	147	66	29	5	1
		+15	72	134	204	233	229	192	149	70	30	5	1
		+40	53	121	199	232	231	193	150	70	31	6	1
0.6		347	384	424	445	426	342	253	181	76	33	7	2
		+55	70	172	293	341	327	268	207	100	47	10	2
		+253	+51	101	263	326	325	270	211	104	49	11	2
		+272	+66	89	257	323	325	272	213	105	49	11	2
0.8		170	308	398	446	427	342	261	196	95	46	12	3
		566	692	727	669	582	426	315	236	119	61	16	4
		786	844	826	718	609	438	322	242	123	63	17	4
		793	856	831	722	613	441	325	244	124	64	17	4
0.9		255	391	484	515	555	336	254	193	99	51	14	4
		1,233	1,107	1,017	860	688	454	324	241	125	66	19	5
		1,337	1,211	1,110	925	730	474	335	249	129	69	20	6
		1,439	1,263	1,133	934	736	477	337	251	130	69	20	6
1.0	9,778	4,879	1,603	1,100	690	506	334	246	189	101	55	16	5
	10,247	7,669	2,667	1,854	1,142	801	481	333	246	129	71	22	7
	11,199	8,074	2,822	1,967	1,214	850	506	347	255	133	73	23	7
	11,289	8,144	2,861	1,995	1,230	859	510	349	257	135	74	23	7
1.1	4,148	2,156	1,680	1,270	771	536	335	242	186	103	58	19	6
	4,224	3,382	2,653	2,019	1,231	846	500	342	251	133	75	25	8
	4,447	3,563	2,797	2,130	1,301	895	526	358	262	138	78	26	9
	4,485	3,594	2,823	2,152	1,316	905	532	361	264	139	79	26	9
1.2	1,716	806	756	696	571	464	320	236	182	103	60	21	7
	1,721	1,282	1,201	1,105	903	727	483	342	254	137	76	27	10
	1,919	1,353	1,268	1,167	954	767	509	359	266	142	82	28	10
	1,937	1,368	1,282	1,180	965	776	515	362	268	143	83	29	10
1.4	718	370	364	356	334	308	253	206	167	102	63	25	10
	741	577	567	553	516	473	385	304	241	140	85	33	13
	780	609	598	583	544	499	403	319	252	146	88	34	13
	788	616	605	589	550	504	407	322	254	147	89	34	13
1.6	411	235	233	231	224	214	191	167	144	96	63	27	12
	433	359	356	351	339	324	287	247	209	135	87	37	16
	456	378	375	370	357	341	302	259	219	141	90	38	16
	461	382	379	374	361	345	305	262	221	142	91	38	17
1.8	276	168	167	166	163	158	147	134	120	87	61	29	14
	294	252	251	249	244	237	219	197	175	124	85	39	18
	309	265	264	262	256	249	230	207	185	130	89	41	19
	312	268	266	264	259	251	232	209	187	131	89	42	19
2.0	201	127	127	126	125	122	116	109	100	77	57	30	15
	216	189	189	188	185	181	171	159	145	111	81	41	20
	227	199	198	197	194	190	180	167	153	116	84	43	21
	229	201	200	199	196	192	182	169	154	117	85	43	21

Note: The four values noted one below the other correspond to $\lambda = 5 \times 10^1$; 5×10^2; 5×10^3; and 5×10^4, respectively.

TABLE 2.—Vertical Stress Coefficients (× 1,000) for $L/d = 25$ (+ Tension, Otherwise Compression)

	n												
m	0.0	0.05	0.075	0.1	0.15	0.2	0.3	0.4	0.5	0.75	1.0	1.5	2.0
(1)	(2)	(3)	(4)	(5)	(6)	(7)	(8)	(9)	(10)	(11)	(12)	(13)	(14)
0.2		5,276	3,841	2,818	1,496	782	217	64	121	3	2	—	—
		1,415	1,108	876	548	345	151	80	51	22	10	2	—
		481	454	409	307	223	126	82	59	28	12	2	—
		375	380	355	279	209	123	82	60	28	13	2	—
0.4		2,096	1,759	1,492	1,078	773	386	192	98	24	8	2	—
		621	540	480	395	332	242	179	133	63	28	5	1
		+49	28	81	145	178	192	173	143	74	35	7	1
		+132	+34	32	115	159	186	172	144	76	36	7	1
0.6		257	332	373	401	387	306	216	145	52	21	4	1
		+303	+137	+17	145	235	284	254	204	102	49	11	2
		+657	+407	+227	18	161	268	262	221	118	58	13	3
		+704	+442	+254	2	152	266	263	223	120	59	13	3
0.8		+995	+479	+187	96	198	224	189	146	68	32	8	2
		+1,583	+599	+78	355	455	407	318	244	125	65	17	5
		+1,656	+568	+6	443	530	456	353	271	142	75	20	5
		+1,671	+569	+1	451	538	461	357	274	144	76	22	5
0.9		+647	+114	70	175	199	194	167	135	71	35	10	3
		108	937	1,028	839	658	445	326	247	131	70	20	6
		615	1,373	1,375	1,054	799	516	370	278	145	80	24	7
		663	1,421	1,415	1,080	816	525	375	282	150	82	24	7
1.0	11,603	1,626	757	447	254	201	168	145	122	70	38	11	4
	37,769	6,375	3,328	2,095	1,133	762	460	327	247	134	75	23	7
	45,045	7,741	4,117	2,617	1,416	940	548	379	283	152	85	27	9
	45,960	7,917	4,215	2,681	1,450	961	559	386	287	154	87	27	9
1.1	1,440	906	718	555	343	241	164	133	112	68	39	13	5
	5,113	3,392	2,735	2,147	1,337	896	503	341	252	137	79	26	9
	6,158	4,104	3,320	2,616	1,634	1,097	607	402	293	157	90	30	10
	6,291	4,196	3,395	2,675	1,675	1,121	619	410	298	159	91	31	10
1.2	573	452	418	379	300	238	164	128	105	66	40	14	5
	2,076	1,685	1,559	1,410	1,107	852	526	357	261	141	82	29	10
	2,513	2,044	1,893	1,713	1,346	1,036	635	425	307	163	95	34	12
	2,568	2,090	1,935	1,752	1,376	1,059	648	433	313	165	96	34	12
1.4	236	210	205	200	186	170	139	114	94	62	40	16	7
	820	735	718	696	640	574	445	339	261	147	89	34	16
	993	890	870	843	774	694	536	406	311	171	103	40	16
	1,014	909	888	861	791	709	547	415	317	175	104	40	16
1.6	144	133	132	130	126	120	108	94	82	57	39	18	8
	473	437	432	423	409	387	335	282	234	145	92	39	17
	570	527	521	514	493	466	403	338	279	171	108	45	19
	582	538	533	525	503	476	411	344	284	174	110	46	20
1.8	101	95	95	94	92	90	84	77	69	51	37	19	9
	318	298	296	294	287	277	253	226	197	136	92	42	20
	382	358	356	353	345	333	304	270	236	161	108	49	21
	390	366	364	361	352	340	310	275	240	164	110	50	23
2.0	77	73	73	72	71	70	67	62	58	46	35	19	10
	232	220	219	218	214	210	197	181	164	122	88	44	22
	278	264	263	261	257	251	236	217	196	145	109	51	25
	284	269	268	266	262	256	240	221	200	148	106	52	26

Note: The four values noted one below the other correspond to $\lambda = 5 \times 10^{1}$; 5×10^{2}; 5×10^{3}; and 5×10^{4}, respectively.

TABLE 3.—Vertical Stress Coefficients (× 1,000) for $L/d = 50$ (+ Tension, Otherwise Compression)

	n												
m (1)	0.0 (2)	0.05 (3)	0.075 (4)	0.1 (5)	0.15 (6)	0.2 (7)	0.3 (8)	0.4 (9)	0.5 (10)	0.75 (11)	1.0 (12)	1.5 (13)	2.0 (14)
0.2		7,025	5,055	3,627	1,812	881	203	45	9	1	—	—	—
		2,987	2,201	1,649	933	530	182	73	36	12	5	1	—
		745	642	544	376	256	129	78	53	25	11	2	—
		430	422	386	294	214	120	78	56	27	12	2	—
0.4		1,440	1,400	1,302	1,041	779	391	185	87	17	5	1	—
		1,564	1,268	1,055	756	554	309	183	114	43	19	4	1
		163	186	201	216	218	201	171	138	71	33	6	1
		+80	1	56	126	163	183	169	142	76	36	7	1
0.6		+44	113	208	301	321	270	190	125	41	15	3	1
		+119	188	236	297	321	297	237	177	79	36	8	2
		+546	+339	+186	30	161	263	257	216	115	57	13	3
		+679	+441	+266	+19	132	256	259	222	121	60	14	3
0.8		+571	+303	+138	41	119	157	141	112	53	24	6	2
		+1,524	+713	+245	192	325	328	264	203	100	50	13	4
		+1,897	+818	+204	342	481	443	348	269	141	74	20	5
		+1,953	+835	+198	364	504	460	361	279	147	77	21	6
0.9		+463	+152	+31	62	99	123	116	99	54	27	7	2
		+374	265	506	514	444	335	258	200	104	55	15	5
		+314	1,021	1,201	987	765	505	365	276	146	79	23	7
		+226	1,148	1,315	1,062	816	531	381	287	153	83	25	7
1.0	8,542	565	235	134	89	90	98	96	85	52	28	9	3
	56,007	4,335	2,134	1,301	704	493	326	246	193	106	58	18	6
	93,948	7,778	3,980	2,480	1,331	890	529	371	278	150	84	27	8
	99,440	8,330	4,278	2,670	1,432	954	561	390	291	157	88	28	9
1.1	507	348	275	212	137	105	88	82	74	49	29	10	4
	3,510	2,447	1,940	1,496	906	602	349	247	190	107	61	20	7
	6,237	4,313	3,443	2,675	1,632	1,075	589	392	287	155	89	30	10
	6,506	4,610	3,683	2,863	1,748	1,150	627	415	302	162	93	31	11
1.2	214	185	172	157	128	107	85	74	67	46	29	11	4
	1,215	1,211	1,114	1,001	776	592	367	255	192	108	64	22	8
	2,564	2,138	1,969	1,771	1,372	1,041	627	417	301	160	93	33	12
	2,652	2,286	2,105	1,894	1,467	1,113	668	443	318	168	98	35	13
1.4	101	96	94	92	87	82	72	63	56	41	28	12	5
	961	522	510	494	453	407	315	242	189	110	67	26	11
	1,016	911	889	860	787	703	537	404	308	169	101	39	16
	1,042	972	949	919	840	750	573	430	327	179	107	41	16
1.6	68	66	65	65	63	61	57	52	47	36	26	13	6
	526	311	308	303	291	275	239	202	169	107	69	29	13
	583	534	528	520	498	470	404	357	278	169	106	44	19
	597	569	563	554	531	501	431	359	295	179	112	47	20
1.8	51	50	50	49	49	48	45	43	40	32	24	13	7
	321	213	212	210	205	198	182	162	143	99	68	32	15
	390	361	359	356	347	335	305	270	235	160	107	48	22
	399	385	382	379	369	356	324	287	250	169	113	51	24
2.0	40	40	39	39	39	38	37	35	33	27	22	13	7
	263	158	157	156	154	150	142	131	119	89	65	33	17
	288	265	264	262	258	252	236	217	196	144	103	51	25
	291	282	280	279	274	268	251	230	208	154	109	54	26

Note: The four values noted one below the other correspond to $\lambda = 5 \times 10^1$; 5×10^2; 5×10^3; and 5×10^4, respectively.

TABLE 4.—Vertical Stress Coefficients (× 1,000) for $L/d = 100$ (+ Tension, Otherwise Compression)

	n												
m (1)	0.00 (2)	0.05 (3)	0.075 (4)	0.1 (5)	0.15 (6)	0.2 (7)	0.3 (8)	0.4 (9)	0.5 (10)	0.75 (11)	1.0 (12)	1.5 (13)	2.0 (14)
0.2		6,480	4,988	3,693	1,860	886	199	50	15	2	1	—	—
		5,539	3,946	2,850	1,489	773	210	58	16	10	1	—	—
		1,484	1,161	916	569	355	150	77	47	19	3	1	—
		553	511	453	331	234	125	77	54	25	11	2	—
0.4		2,657	1,849	1,916	1,859	900	386	194	98	22	7	1	—
		2,232	1,857	1,562	1,111	785	382	185	91	21	7	1	—
		723	615	538	428	351	245	177	130	61	27	5	1
		42	97	133	177	196	195	171	140	73	34	6	1
0.6		228	313	359	391	379	263	190	128	45	17	4	1
		110	194	248	303	312	299	209	139	49	19	4	1
		+202	+73	23	159	237	282	252	203	102	49	11	2
		+541	+337	+186	28	160	264	260	220	118	58	13	3
0.8		+56	29	83	142	165	166	142	113	55	25	6	2
		+1,089	+578	+269	48	169	211	181	141	65	30	7	2
		+1,675	+752	+208	294	431	406	321	247	126	65	17	5
		+1,812	+790	+188	360	499	456	358	276	144	75	20	5
0.9		+958	62	103	131	139	136	121	101	55	28	8	3
		+905	228	300	137	174	181	158	129	67	34	9	3
		+653	693	931	817	655	448	330	250	132	70	20	6
		+451	1,038	1,249	1,032	799	524	377	284	150	81	24	7
1.0	5,950	318	186	145	125	120	114	103	89	54	30	9	3
	46,894	1,547	673	379	211	173	153	136	115	67	36	11	4
	191,043	6,446	3,246	2,011	1,090	743	458	328	249	135	75	23	7
	194,408	7,995	4,076	2,541	1,373	922	549	384	287	155	87	27	9
1.1	256	215	186	160	128	113	100	90	79	51	30	10	4
	1,210	934	725	547	324	221	149	124	105	65	37	12	4
	4,984	3,672	2,915	2,252	1,365	900	502	341	252	138	79	26	9
	6,118	4,524	3,600	2,788	1,694	1,114	610	406	297	159	91	31	10
1.2	147	138	133	126	114	104	90	80	71	49	30	11	4
	1,025	460	422	379	294	228	153	119	98	63	38	13	5
	2,046	1,815	1,670	1,500	1,159	879	533	359	263	142	83	29	11
	2,512	2,288	2,060	1,850	1,430	1,083	650	432	312	165	96	34	12
1.4	88	86	85	84	82	79	72	65	59	43	29	13	5
	717	206	202	196	181	165	133	108	89	58	38	16	6
	813	773	755	731	669	598	458	347	266	148	39	35	14
	998	950	927	897	820	732	559	420	319	175	104	40	16
1.6	64	63	63	63	62	60	57	53	49	38	27	13	6
	433	128	127	126	121	116	103	90	78	54	37	17	8
	469	455	450	443	424	401	346	289	239	147	93	39	17
	574	556	550	541	518	489	420	350	288	175	110	46	20
1.8	50	49	49	49	48	48	46	43	40	33	25	14	7
	294	91	91	90	88	86	80	73	66	49	35	18	9
	316	309	307	304	296	286	261	232	202	138	93	42	20
	385	376	373	370	360	348	317	280	244	165	110	50	23
2.0	40	40	40	40	39	39	38	36	34	29	23	13	7
	171	70	69	69	68	67	64	59	55	43	33	18	9
	231	227	226	224	221	216	202	186	168	125	99	44	22
	280	275	274	272	268	261	245	225	203	150	106	52	26

Note: The four values noted one below the other correspond to $\lambda = 5 \times 10^1$; 5×10^2; 5×10^3; and 5×10^4, respectively.

APPENDIX.—REFERENCES

1. Geddes, J. D., "Stresses in Foundation Soils Due to Vertical Subsurface Loadings," *Geotechnique*, London, England, Vol. 16, No. 3, 1966, pp. 231–255.
2. Geddes, J. D., "Boussinesq Based Approximations to the Vertical Stresses Caused by Pile Type Subsurface Loadings," *Geotechnique*, London, England, Vol. 19, No. 4, pp. 509–514.
3. Mattes, N. S., and Poulos, H. G., "Settlement of Single Compressible Pile," *Journal of the Soil Mechanics and Foundations Division*, ASCE, Vol. 95, No. SM1, Proc. Paper 6356, Jan., 1969, pp. 189–207.
4. Mindlin, R. D., "Force at a Point in the Interior of a Semiinfinite Solid," *Physics*, Vol. 7, May, 1936, pp. 195–202.

JOURNAL OF THE GEOTECHNICAL ENGINEERING DIVISION

DISCUSSION

Note.—This paper is part of the Journal of the Geotechnical Engineering Division, Proceedings of the American Society of Civil Engineers, © ASCE, Vol. 107, No. GT1, January, 1981. ISSN 0093-6405/81/0001-0113/$01.00

Discussions

Discussions may be submitted on any Proceedings paper or technical note published in any *Journal* or on any paper presented at any Specialty Conference or other meeting, the *Proceedings* of which have been published by ASCE. Discussion of a paper/technical note is open to anyone who has significant comments or questions regarding the content of the paper/technical note. Discussions are accepted for a period of 4 months following the date of publication of a paper/technical note and they should be sent to the Manager of Technical and Professional Publications, ASCE, 345 East 47th Street, New York, N.Y. 10017. The discussion period may be extended by a written request from a discusser.

The original and three copies of the Discussion should be submitted on 8-1/2-in. (220-mm) by 11-in. (280-mm) white bond paper, typed double-spaced with wide margins. The length of a Discussion is restricted to two *Journal* pages (about four typewritten double-spaced pages of manuscript including figures and tables); the editors will delete matter extraneous to the subject under discussion. If a Discussion is over two pages long it will be returned for shortening. All Discussions will be reviewed by the editors and the Division's or Council's Publications Committees. In some cases, Discussions will be returned to discussers for rewriting, or they may be encouraged to submit a paper or technical note rather than a Discussion.

Standards for Discussions are the same as those for Proceedings Papers. A Discussion is subject to rejection if it contains matter readily found elsewhere, advocates special interests, is carelessly prepared, controverts established fact, is purely speculative, introduces personalities, or is foreign to the purposes of the Society. All Discussions should be written in the third person, and the discusser should use the term "the writer" when referring to himself. The author of the original paper/technical note is referred to as "the author."

Discussions have a specific format. The title of the original paper/technical note appears at the top of the first page with a superscript that corresponds to a footnote indicating the month, year, author(s), and number of the original paper/technical note. The discusser's full name should be indicated below the title (see Discussions herein as an example) together with his ASCE membership grade (if applicable).

The discusser's title, company affiliation, and business address should appear on the first page of the manuscript, along with the *Proceedings* paper number of the original paper/technical note, the date and name of the *Journal* in which it appeared, and the original author's name.

Note that the discusser's identification footnote should follow consecutively from the original paper/technical note. If the paper/technical note under discussion contained footnote numbers 1 and 2, the first Discussion would begin with footnote 3, and subsequent Discussions would continue in sequence.

Figures supplied by the discusser should be designated by letters, starting with A. This also applies separately to tables and references. In referring to a figure, table, or reference that appeared in the original paper/technical note use the same number used in the original.

It is suggested that potential discussers request a copy of the *ASCE Authors' Guide to the Publications of ASCE* for more detailed information on preparation and submission of manuscripts.

Extreme-Value Problems of Limiting Equilibrium[a]

Discussion by Reginald A. Barron,[3] F. ASCE

This paper presents an analysis method for stability problems at limiting equilibrium using the method of variational calculus. This calculus is not new, but the writer doubts that many engineers in the field are familiar with it. If it is to be used by the profession, additional details should be given. It is considered by the writer that important omissions were made in this paper which, had they been included, would have improved the clarity and value of the paper. These omissions are:

1. No list of assumptions is given. Near the end of the introduction the authors state that none are used. Certainly the use of the effective stress concept as expressed by Eq. 1 is one. Another is the use of safety factor, F, to apply not only for the overall stability, but also as a point safety factor when F is greater than unity.
2. No illustrative examples are given. To aid the comprehension by most engineers a detailed example would be most useful.
3. No comparison with results of others are given. Near the end of the section on "Slope Stability Problems" the authors state the results of their method "are almost identical with those given by Taylor (8)." If this is so, what is the purpose for using a more complicated method of analysis?
4. No discussion is included indicating the influence of the soil stress-strain properties on the validity of the method. In fact, in the second paragraph of the "Summary and Conclusions" the authors state that the method "takes into account all the possible distribution of soil properties . . . and pore-water pressures."

Nowhere in the paper are the strength parameters defined. The writer assumes since an effective stress equation is used (Eq. 1) that the strength parameters are those obtained from consolidated-drained (S) shear tests. The writer concurs in the application of Eq. 1 to failure conditions where F is equal to unity; but for cases where F is greater than unity the drained shear strength for the nonfailure effective normal stress is generally not available. See Barron (10,11) Gould (14) and Johnson (12,13). Except for dry, cohesionless soils the potential shear strength of a wet soil not at a failure condition is the undrained strength that can be obtained without any change in the water content. The shear strength tests are, therefore, the consolidated-undrained (R) or the unconsolidated-undrained (Q) as the conditions to be analyzed indicate. In the writer's opinion,

[a]October, 1979, by Michael Garber and Rafael Baker (Proc. Paper 14901).
[3]Consulting Engr., 62 Horshoe Rd., Guilford, Conn. 06437.

the concept indicated by Eq. 1 is the most misused idea of soil mechanics.

If a stable stress condition exists in a moist soil and an undrained shear test is made, the effective stress path for a dilative soil has a positive slope and at failure the pore pressure can be negative (gage) resulting in a shear strength at failure larger than that given by Eq. 1 with the effective normal stress that which exists on the potential failure surface at the initiative of the test. Because large negative pore pressures (gage) can occur in a test using large back pressure to prevent pore-water cavitation, the full shear strength given by this test may not be conservative to use in a stability study.

If the soil is compressive (strain-softening), then the effective stress path rises to the failure strength curve with a negative slope. Large positive pore pressures can exist and the shear strength at failure is less than that indicated by Eq. 1. The shear strength indicated by Eq. 1 can be realized only if water content changes can occur. If they cannot, then it is improper to use the results of Eq. 1.

In addition, if F, the average safety factor, is larger than unity, then the stress conditions in the soil mass are highly indeterminate and the concept of a limiting equilibrium condition with a reduced shear strength being applied to a given problem is certainly an assumption, but one which is commonly made without, however, claims being made for any greater degree of exactness. An excellent discussion of the difficulties of analyzing slopes is given by Johnson (12,13). It would be desirable if the authors define Dirac's function and Lagrange's undetermined multipliers.

In conclusion, the writer questions the advisability of publishing theoretical papers of this kind without it being so written that it can be comprehended by a large portion of the society's membership.

Appendix.—References

10. Barron, R. A. "Discussion of paper by Bishop and Morgenstern, Stability Coefficients for Earth Slopes," *Geotechnique* 10:4: 129–150; Vol. XIV, No. 4, Dec., 1964, pp. 134–261.
11. Barron, R. A., *Proceedings of the Sixth International Conference on Soil Mechanics and Foundation Engineers*, Vol. III, Sept., 1965, p. 559.
12. Johnson, S. J., "Analysis and Design Relating to Embankments: A State of the Art Review," *Misc. Paper S-75-3*, Waterways Experiment Station, Vicksburg, Miss., 1975.
13. Johnson, S. J., "Analysis and Design Relating to Embankments: A State of the Art Review," *Proceedings of the Conference on Analysis in Geotechnical Engineering*, University of Texas, Austin, Texas and the Geotechnical Division, ASCE, Vol. III, 1974, pp. 1–48.
14. "Soil Mechanics, Foundation and Earth Structures, *NAVDOCK Design Manual, DM-7*, Department of the Navy, Bureau of Yards and Docks, 1961.

Discussion by Ryszard J. Izbicki[4]

The authors applied a generalized limit equilibrium approach to the problems of slope stability and problems of limiting magnitude, and location or direction of a load and external moment. The most important result is a basic theorem

[4]Adjunct, Inst. of Geotechnics, Technical Univ. of Wrocław, ul. Głogowska 9/72, 53-621 Wrocław, Poland.

of limit equilibrium which states that the critical value of the extermization parameter (F = the factor of safety; P = an external load; M = an external moment, etc.) is independent of the normal stress distribution along the critical slip line. Simultaneously, the variational analysis establishes the existence of two (rotational and translational) modes of failure mechanism. In the case of the rotational mode of failure the potential slip lines are a log-spiral but if the translational mode of failure exists, the potential slip lines are straight lines. The analysis was performed without any a priori assumptions regarding slip line and normal stress distribution; all the equilibrium equations are satisfied and no aditional assumptions were in the investigation process. The results stated in the paper are very interesting but are not surprising.

So, approximate methods for solving the problems of soil stability may be divided into (15,16,18): (1) Methods of limit analysis based on two limit theorems; and (2) methods of approximate satisfying of conditions of equilibrium and yield criterion only in the definite points or regions of the material considered. These method are called the limit equilibrium methods.

In the limit analysis for elastic or rigid-plastic material obeying the associated flow law the validity of two basic limit theorems is proved, making use of the principle of maximum plastic work. According to the statement of this theorems, in order to properly bound the "true" solution, it is necessary to find a kinematically admissible failure mechanism (velocity or flow field) in order to obtain an upper bound solution. A statically admissible stress field, satisfying all the equilibrium conditions and nowhere violating the yield criterion, will be required for a lower bound solution. If the upper and lower bounds coincide, the exact value of the collapse, or limit, load (factor of safety, etc.) is determined (15,18).

An upper bound solution may be obtained (see Ref. 18) by: (1) Comparing the sum of the total work of external forces and total work of body forces with the total internal dissipation of energy (this method is called herein energy approach); or (2) making use of equilibrium conditions of the field of forces (stresses) associated with the assumed kinematically admissible failure mechanism (equilibrium approach).

Both the approaches are equivalent. It can be observed, that the equations of the work balance, may be treated as an equation of virtual work and, thus, as an equation that expresses the condition of global equilibrium. A number of examples solved by means of the two approaches are discussed in Ref. 18.

The upper bound equilibrium approach is more advantageous in relation to the analysis starting from work balance. Namely, it provides more information about the stress distribution inside the material or the force (load) distribution along contact lines. There are, however, difficulties in applying this approach in the case of layered soil profile and composed failure mechanisms, which consist of rigid zones (blocks) and soft zones.

In the case of associated flow law the energy dissipated within the failure mechanism is independent of the stress distribution. Therefore the determined value of limit load (and all other parameters) will be independent of the internal stress distribution. In the kinematically admissible failure mechanism, the potential slip lines are either log-spirals (rotational mode) or straight lines (translational mode).

The aforementioned properties of the upper bound solutions and kinematically admissible mechanisms follow from the associated flow law. The same properties are obtained by the authors by applying, in the light of the assumed classification of methods, the upper bound generalized equilibrium approach. Their considerations, however, are limited to the case of failure mechanisms consisting of one rigid block which undergoes either rotation or translation.

The upper bound energy approach allows the consideration of complex failure mechanisms composed of a number of rigid blocks which undergo either translation or rotation, as well as of mechanisms containing soft zones, which are deformed during plastic strain. Some examples on composed failure mechanisms have been given by Gudehus (17), Chen (15), the writer and Mróz (18), and Karal (19).

To conclude we may add that conventional limit equilibrium methods based on static equilibrium of forces (or stresses) acting on the yield region are in many cases equivalent to the upper bound method (see equilibrium approach). However, the assumed failure mechanism must be kinematically admissible and it must be associated by the appropriate volumetric dilatation. When the failure mechanism is not kinematically admisible from viewpoint of limit analysis, it may be neither upper bound not the lower one. However, each upper bound (equilibrium approach) solution is always equivalent to the limit equilibrium method (15,18).

Appendix.—References

15. Chen, W. F., "Limit Analysis and Soil Plasticity," American Elsevier Publishing Co., Inc., New York, N.Y., 1975.
16. Chen, W. F., and Scawthorn, C. R., "Limit Analysis and Limit Equilibrium Solutions in Soil Mechanics," *Soil and Foundations*, Vol. 10, No. 3, 1970, pp. 13–49.
17. Gudehus, G., "Lower and Upper Bounds for Stability of Earth-Retaining Structures," *Proceeding of the 5th European Conference on Soil Mechanics and Foundation Engineering*, Vol. 1, 1972, pp. 21–28.
18. Izbicki R. J., and Mróz, Z., "Limit States in Soil and Rock Mechanics," PWN, Warszawa, 1976, (in Polish).
19. Karal, K., "Energy Method for Soil Stability Analyses," *Journal of the Geotechnical Engineering Division*, ASCE, Vol. 103, No. GT5, Proc. Paper 12917, May, 1977, pp. 431–445.

Discussion by A. Luceño[5] and E. Castillo[6]

The authors state a generalized extreme-value problem of *LE* as a search for a pair of functions $y(x)$ and $\sigma(x)$ that realize the extremum X_{ex} of X subject to the satisfaction of the three LE equations (3).

However it can be easily demonstrated that functional $X[y(x),\sigma(x)]$ is, in general, unbounded. Therefore there exists a potential sliding line $y(x)$ and a normal stress distribution $\sigma(x)$ giving a safety factor as small as desired,

[5]Escvela Técnica Superior de Ingenieros de Caminos, Canales, y Puertos, opto. de Matemáticas Aplicadas a la Ingeniería, Universidad de Santander, Avda. de los Castros, s/n—Santander, España.
[6]Escvela Técnica Superior de Ingenieros de Caminos, Canales, y Puertos, opto. de Matemáticas Aplicadas a la Ingeniería, Avda. de los Castros, s/n—Santander, España.

and in consequence the extreme problem is incorrectly stated.

In order to give an example of the unbounded character of functional $X[y(x),\sigma(x)]$ let us consider Eqs. 3*a*, 3*b* and 3*c* for the case of a slope in an homogeneous soil and lack of pore water pressure and external loads. These equations in adimensional form become (when $k = 1$):

$$\int_{X_0}^{X_1} [(N + S\psi) - FSY'] \, dX = 0 \quad \ldots \quad (29)$$

$$\int_{X_0}^{X_1} [(N + S\psi)\, Y' - F(\bar{Y} - Y - S)] \, dX = 0 \quad \ldots \quad (30)$$

$$\int_{X_0}^{X_1} \{(N + S\psi)(Y - Y'X) - F[S(X + Y'Y) - X(\bar{Y} - Y)]\} \, dX = 0 \quad \ldots \quad (31)$$

in which the following adimensional parameters have been used: $N = c/\gamma H$, $S = \sigma/\gamma H$, $\psi = tg(\phi)$, $X = x/H$, $Y = y/H$, $\bar{Y} = \bar{y}/H$, $Y' = dY/dX$, where X_0, X_1 = the abscissas of the end points of the sliding line; and H = the height of the slope.

By making $X = F$ (Baker and Garber, 1978), Eq. 29 gives:

$$F = \frac{\int_{X_0}^{X_1} (N + S\psi)\, dX}{\int_{X_0}^{X_1} S\, Y'\, dX} \quad \ldots \quad (32)$$

So, according to Garber and Baker, the problem can be stated as minimizing Eq. 32 subject to conditions described by Eqs. 30 and 31.

One way of demonstrating that Eq. 32, subject to Eqs. 30 and 31, does not attain an absolute minimum is by selecting a sliding line $Y^*(X)$, not a log-spiral, and by using the Ritz method to check that the functional $F^*[S(X)]$ obtained by substituting the equation of this sliding line in Eq. 32 and Eqs. 30 and 31 has no absolute minimum.

As it is well known, Ritz's method consists of a discretization of the vector space of possible solutions. So, a system of basic functions $[l_i(X)]$ is selected and the solution is assumed to be of the type:

$$S(X) = \sum_{i=1}^{n} \alpha_i l_i(X); \quad \alpha_i = cte, \quad (i = 1, 2, \ldots, n) \quad \ldots \quad (33)$$

According to this assumption the functional $F^*[S(X)]$ becomes a function of n-2 variables from which its minimum must be investigated.

In effect, let us consider a slope defined by the following geometrical and geotechnical characteristics: $c = 1\ Tn/m^2$; $\psi = tg(\phi) = 1$; $\gamma = 2\ Tn/m^3$; and $H = 3\ m$.

The characteristics of the slope, in adimensional form are: $N = c/\gamma H = 1/6$, $\psi = 1$ and its equation is given by:

$$\bar{Y} = 0; \quad \forall X \le 0; \quad \bar{Y} = 3X; \quad \forall X \in (0, 1/3);$$

$$\bar{Y} = 1; \quad \forall X \ge 1/3 \quad \ldots \quad (34)$$

The safety factor of this slope according to the solution given by Euler's equations is approx 1.8.

If the following potential slip line: $Y^*(X) = 3X^2 - 1/3$ and the system of basic functions: $l_1(X) = X^2$; $l_2(X) = X$; $l_3(X) = 1$ are selected, functional $F^*[S(X)]$, according to Eqs. 32, 30 and 31, becomes a function of one variable defined by the following system of equations:

$$(2 - 5F^*)\alpha_1 + (3 - 12F^*)\alpha_2 + (18 - 18F^*)\alpha_3 = -3 \quad \ldots\ldots\ldots (35)$$

$$(5 + 2F^*)\alpha_1 + (12 + 3F^*)\alpha_2 + (18 + 18F^*)\alpha_3 = -3 + 9F^* \quad \ldots\ldots (36)$$

$$(192 + 345F^*)\alpha_1 + (315 + 612F^*)\alpha_2 + (1{,}080 + 1{,}080F^*)\alpha_3$$

$$= -180 + 195F^* \quad \ldots\ldots\ldots\ldots\ldots\ldots\ldots\ldots\ldots (37)$$

This system can be solved in α_1, α_2, and α_3 for values of F^* not equal to $-1/3$. This shows that Eq. 32 subject to conditions described in Eqs. 30 and 31 is unbounded.

Nevertheless, it is worthwhile to make some comments:

1. Though the safety factor must be positive, this fact is not explicitly reflected in the statement of the problem, and as a consequence the system, Eqs. 35, 36 and 37 can be solved for negative values of F^*.
2. In the same way, the condition given by the Mohr-Coulomb failure criterion:

$$S(X) \geq -N/\psi; \quad \forall X \in (X_0, X_1) \quad \ldots\ldots\ldots\ldots\ldots\ldots (38)$$

is not included, and as a consequence the system of Eqs. 35, 36, and 37 gives solutions not satisfying this condition.

One way of taking into account these constraints in the statement of the problem is by making:

$$F = K^2 \quad \ldots\ldots\ldots\ldots\ldots\ldots\ldots\ldots\ldots\ldots\ldots (39)$$

$$S(X) = [\epsilon(X)]^2 - \frac{N}{\psi} \quad \ldots\ldots\ldots\ldots\ldots\ldots\ldots\ldots (40)$$

which lead to the system:

$$\int_{X_0}^{X_1} \left[\psi\epsilon^2 - K^2\left(\epsilon^2 - \frac{N}{\psi}\right) Y' \right] dX = 0 \quad \ldots\ldots\ldots\ldots\ldots (41)$$

$$\int_{X_0}^{X_1} \left[\psi\epsilon^2 Y' - K^2\left(\bar{Y} - Y - \epsilon^2 + \frac{N}{\psi}\right) \right] dX = 0 \quad \ldots\ldots\ldots\ldots (42)$$

$$\int_{X_0}^{X_1} \left\{ \psi\epsilon^2(Y - Y'X) - K^2\left[\left(\epsilon^2 - \frac{N}{\psi}\right)(X + Y'Y) \right.\right.$$

$$\left.\left. - X(\bar{Y} - Y) \right]\right\} dX = 0 \quad \ldots\ldots\ldots\ldots\ldots\ldots\ldots (43)$$

Eq. 41 defines functional $K^2 = F$ which must be minimized subject to the conditions described by Eqs. 42 and 43.

The extremals of this new problem are exactly the same as those of the

old functional and it can be demonstrated by a counterexample that the new functional does not attain a relative minimum either (the first writer, 1979; the writers, 1980).

Appendix.—References

20. Baker, R., and Garber, M., "Theoretical analysis of the Stability of Slopes," *Géotechnique*, Vol. 28, No. 4, 1978, pp. 395–411.
21. Luceño, A. (1979), Análisis de los métodos Variacionales aplicados a los problemas de establidad en Mecánica del Suelo, Utilización del teorema de la cota superior, Ph.D. Thesis, University of Santander, Spain.
22. Luceño, A., and Castillo, E., "Evaluation of Variational Methods in Slope Analysis," *International Symposium on Landslides*, New Delhi, India, 1980.
23. Luceño, A., and Castillo, E. (1980), Análisis crítico de los métodos variacionales aplicados a la estabilidad de taludes, Boletín del Laboratorio del Transporte y Mecánica del Suelo "José Luis Escario," Madrid.

Closure by Michael Garber[7] and Rafael Baker[8]

The writers thank all the discussers for the interest expressed in the paper.

The discussion by A. Luceno and E. Castillo suggests that in the extreme-value problem of LE presented by the writers the extremization parameter {functional $X[y(x), \sigma(x)]$} is, in general, unbounded. The discussers claim that there always exist a pair of functions $y(x)$ and $\sigma(x)$ "giving (a) safety factor as small as desired, and in consequence the extreme problem is incorrectly stated." To prove it, the discussers provide a "counter example" that, in their understanding, clearly disqualifies the writers' presentation. The example refers to a slope which, according to the writers' solution, has a safety factor of 1.8. The discussers chose at random a potential slip line $y(x)$ and assumed the pressure distribution $\sigma(x)$ to be presented by a polynomial with three unknown parameters σ_1, α_2, and α_3. Substituting their functions $y(x)$ and $\sigma(x)$ into the writers' equilibrium equations the discussers derived a system of three linear equations with respect to three unknowns α_1, α_2, and α_3. This system can be solved for almost any value of the safety factor, F. It seems therefore, that the discussers can always point out a pair, $y(x)$ and $\sigma(x)$, that not only gives F less than 1.8 but, moreover, F "as small as desired."

The point is, however, that there are natural restrictions on the value of F as well as on the character of the $\sigma(x)$ function, and the discussers recognize this as they make an attempt to modify the problem presentation. These restrictions are: (1) $F \geq 0$ (the safety factor is non-negative by definition); and (2) $\sigma(x) \geq -c/\psi$ while $\sigma \not\equiv -c/\psi$ (a condition supplementing the Mohr-Coulomb failure condition).

These restrictions were not mentioned explicitly in the paper, but as the discussers know, their incorporation does not change the variational solution. If we consider the discussers "counter example" in view of these restrictions,

[7]Sr. Research Assoc., Transport Tech. Lab., Dept. of Mech. and Aeronautical Engrg., Room 203 C. J. Mackenzie Building, Carleton Univ., Ottawa, Canada K1S 5B6.

[8]Sr. Research Fellow, Soil Mechanics Dept., Faculty of Civ. Engrg., Technion-Israel Inst. of Tech., Haifa, Israel.

then it fails to prove anything but the validity of the writers solution. The nondimensional pressure distribution $S(x)$ assumed by the discussers was inspected in the range $0 \leq F \leq 4$ [Figs. 5(*b*) and 5(*c*)] against restriction 2, which in nondimensional terms is rewritten as $S(x) \geq N/\psi$. It was found that the minimal S always occurs at the end points x_0 and x_1 [Figs. 5(*a*) and 5(*b*)] of the slip line $y(x)$. As it can be seen from Figs. 5(*b*) and 5(*c*), $S(x)$ satisfies restriction 2 for $F \geq 4$ but fails to satisfy it for any $0 \leq F < 4$. This implies that $F = 4$ is the minimum the discussers can claim for their example without violating the obvious restrictions previously mentioned. As 4 is greater than 1.8 the "counter example" clearly fails. Possibly in expectation of this the discussers refer to another example that is supposed to demonstrate their point. The reference is to two papers in Spanish (local bulletins) and one in English

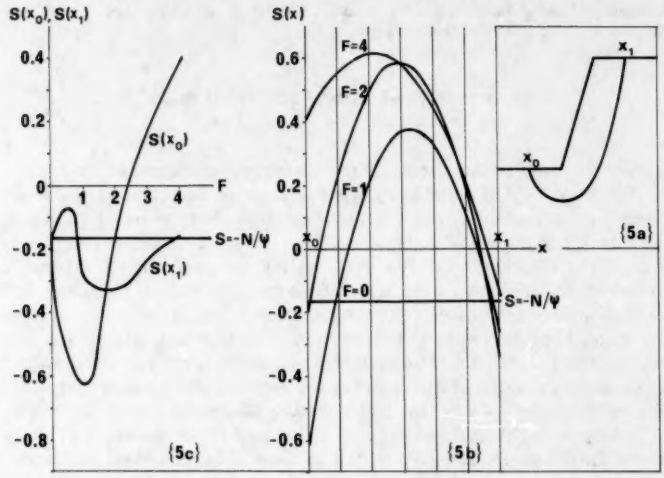

FIG. 5.—Investigation of Discusser's Example: (*a*) Discusser's Potential Slip Line; (*b*) Pressure Distribution $S(x)$ for Range $0 < F < 4$; (*c*) Pressure at End Points x_0 and x_1 for Range $0 < F < 4$

(Symposium in India). The writers' efforts to obtain these papers have been unsuccessful and thus comment is reserved.

The variational solutions proved to satisfy restrictions 1 (which in general has to be stated as $X \geq 0$, in which X = the extremization parameter) and 2 as demonstrated by solutions presented by the writers (5). Taking the opportunity, the writers would like to introduce an additional (kinematic) restriction that must be imposed on the shape of $y(x)$. This third restriction states that the sliding is possible only when the curvature of $y(x)$ decreases in the direction of sliding. Thus, there are "proper" and "improper" potential slip lines, and $y(x)$ used by the discussers [see Fig. 5(*a*)] obviously belongs to the class of "improper." The variational (extremal) $Y(x)$ always satisfies the third restriction. Indeed, using Eq. 8*b* the curvature ρ of $Y(x)$ is expressed as

$$\rho = \left| \frac{Y''}{(1 + Y'^2)^{3/2}} \right| = \frac{1}{r\sqrt{1 + \left(\frac{k\psi}{F}\right)^2}} \quad \ldots\ldots\ldots\ldots\ldots\ldots \quad (44)$$

As was shown in the paper, the radius vector **r** increases in the direction of sliding (see Geometrical Analysis section), consequently ρ, (Eq. 44), decreases in the direction of sliding.

The discussion by R. A. Barron questions the manner in which the material is presented. The writers readily agree with a number of points raised. The original text was about 25% longer and it included more detail explanations about the essence of the method and its limitations. We had, however, to follow the reviewers request to considerably shorten the paper.

The discussion by R. J. Izbicki provides a profound analysis of the writers method from the point of view of the limit analysis approach. The writers found a special interest in this discussion.

Errata.—The following corrections should be made to the original paper:

Page 1158, paragraph 1, line 3: Should read "the negative *x* direction," instead of "the negative *c* direction,"

Page 1164, line 10: Should read "(rotational mode of failure)," instead of "(rotational mode of failure,"

Technical Papers

Original papers should be submitted in triplicate to the Manager of Technical and Professional Publications, ASCE, 345 East 47th Street, New York, N.Y. 10017. Authors must indicate the Technical Division or Council, Technical Committee, Subcommittee, and Task Committee (if any) to which the paper should be referred. Those who are planning to submit material will expedite the review and publication procedures by complying with the following basic requirements:

1. Titles must have a length not exceeding 50 characters and spaces.

2. The manuscript (an original ribbon copy and two duplicate copies) should be double-spaced on one side of 8-1/2-in. (220-mm) by 11-in. (280-mm) paper. Three copies of all figures and tables must be included.

3. Generally, the maximum length of a paper is 10,000 word-equivalents. As an *approximation*, each full manuscript page of text, tables or figures is the equivalent of 300 words. If a particular subject cannot be adequately presented within the 10,000-word limit, the paper should be accompanied by a rationale for the overlength. This will permit rapid review and approval by the Division or Council Publications and Executive Committees and the Society's Committee on Publications. Valuable contributions to the Society's publications are not intended to be discouraged by this procedure.

4. The author's full name, Society membership grade, and a footnote stating present employment must appear on the first page of the paper. Authors need not be Society members.

5. All mathematics must be typewritten and special symbols must be identified properly. The letter symbols used should be defined where they first appear, in figures, tables, or text, and arranged alphabetically in an appendix at the end of the paper titled Appendix.—Notation.

6. Standard definitions and symbols should be used. Reference should be made to the lists published by the American National Standards Institute and to the *Authors' Guide to the Publications of ASCE*.

7. Figures should be drawn in black ink, at a size that, with a 50% reduction, would have a published width in the *Journals* of from 3 in. (76 mm) to 4-1/2 in. (110 mm). The lettering must be legible at the reduced size. Photographs should be submitted as glossy prints. Explanations and descriptions must be placed in text rather than within the figure.

8. Tables should be typed (an original ribbon copy and two duplicates) on one side of 8-1/2-in. (220-mm) by 11-in. (280-mm) paper. An explanation of each table must appear in the text.

9. References cited in text should be arranged in alphabetical order in an appendix at the end of the paper, or preceding the Appendix.—Notation, as an Appendix.—References.

10. A list of key words and an information retrieval abstract of 175 words should be provided with each paper.

11. A summary of approximately 40 words must accompany the paper.

12. A set of conclusions must end the paper.

13. Dual units, i.e., U.S. Customary followed by SI (International System) units in parentheses, should be used throughout the paper.

14. A practical applications section should be included also, if appropriate.